

AD-A210 180

Martin Marietta Laboratories

MARTIN MARIETTA

STILL FILE COPY

(2)

MML TR 89-56c

HIGH-STRAIN-RATE BEHAVIOR OF HYDRATED CEMENT PASTE

Submitted to:

Air Force Office of Scientific Research
Bolling Air Force Base
Washington, D.C. 20332-6448

Submitted by:

Martin Marietta Laboratories
1450 S. Rolling Road
Baltimore, Maryland 21227-3898

and

University of Maryland
College Park, Maryland 20742

DTIC
ELECTE
JUL 11 1989
S D

DISSEMINATION STATEMENT
Approved for public release
Distribution Unlimited

May 1989

89 7 11 030

MML TR 89-56c

HIGH-STRAIN-RATE BEHAVIOR OF HYDRATED CEMENT PASTE

Submitted to:

Air Force Office of Scientific Research
Bolling Air Force Base
Washington, D.C. 20332-6448

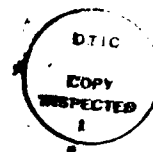
Submitted by:

Martin Marietta Laboratories
1450 S. Rolling Road
Baltimore, Maryland 21227-3898

and

University of Maryland
College Park, Maryland 20742

May 1989



Accession For	
NTIS CRA&I	<input checked="checked" type="checkbox"/>
DTIC TAB	<input type="checkbox"/>
Unannounced	<input type="checkbox"/>
Justification	
By	
Distribution/	
Availability Codes	
Dist	Avail and/or Special
A-1	

UNCLASSIFIED

SECURITY CLASSIFICATION OF THIS PAGE

REPORT DOCUMENTATION PAGE

Form Approved
OMB No. 0704-0188

1a. REPORT SECURITY CLASSIFICATION Unclassified			1b. RESTRICTIVE MARKINGS		
2a. SECURITY CLASSIFICATION AUTHORITY			3. DISTRIBUTION/AVAILABILITY OF REPORT Approved for public release, distribution unlimited		
2b. DECLASSIFICATION/DOWNGRADING SCHEDULE			4. PERFORMING ORGANIZATION REPORT NUMBER(S) MML TR 89-56c		
6a. NAME OF PERFORMING ORGANIZATION Martin Marietta Laboratories			6b. OFFICE SYMBOL (if applicable) NA		
6c. ADDRESS (City, State, and ZIP Code) 1450 South Rolling Road Baltimore, Maryland 21227			7a. NAME OF MONITORING ORGANIZATION Air Force Office of Scientific Research		
8a. NAME OF FUNDING/SPONSORING ORGANIZATION AFOSR			8b. OFFICE SYMBOL (if applicable) NA		
8c. ADDRESS (City, State, and ZIP Code) Bolling AFB Washington DC 20332-6448			9. MONITORING ORGANIZATION REPORT NUMBER(S) AFOSR-TR-89-U927		
9. PROCUREMENT INSTRUMENT IDENTIFICATION NUMBER F4962-86-C-0021			10. SOURCE OF FUNDING NUMBERS		
PROGRAM ELEMENT NO. 61102F		PROJECT NO. 2302	TASK NO. C2	WORK UNIT ACCESSION NO.	
11. TITLE (Include Security Classification) High Strain-Rate Behavior of Hydrated Cement Paste					
12. PERSONAL AUTHOR(S) A. Ritter, G. Childs, K. Bridger, S. Winzer, D. Barker, and R. Dick					
13a. TYPE OF REPORT Final		13b. TIME COVERED FROM 1/86 TO 5/89		14. DATE OF REPORT (Year, Month, Day) 89 May 31	
15. PAGE COUNT 101					
16. SUPPLEMENTARY NOTATION					
17. COSATI CODES			18. SUBJECT TERMS (Continue on reverse if necessary and identify by block number)		
FIELD	GROUP	SUB-GROUP	Cement microstructure, dynamic loading, shock effects. CONCRETE		
19. ABSTRACT (Continue on reverse if necessary and identify by block number)					
<p>Cement paste and mortar were studied at intermediate to high strain-rates, $10^2 - 10^5 \text{ s}^{-1}$, and peak pressures up to 150 kbar, to determine how the microstructure responded to dynamic loading. Intermediate response was primarily brittle failure, while high strain-rate (shock) loads induced microcracking, particle size reduction, lattice distortion and alteration and/or elimination of porosity. Effects were isolated by comparing explosively-loaded specimens with unshocked reference materials, using X-ray diffraction, scanning electron microscopy, and mercury porosimetry.</p>					
20. DISTRIBUTION/AVAILABILITY OF ABSTRACT <input checked="" type="checkbox"/> UNCLASSIFIED/UNLIMITED <input type="checkbox"/> SAME AS RPT. <input type="checkbox"/> DTIC USERS			21. ABSTRACT SECURITY CLASSIFICATION Unclassified		
22a. NAME OF RESPONSIBLE INDIVIDUAL SPENCER T. WY			22b. TELEPHONE (Include Area Code) (202) 267-6862		22c. OFFICE SYMBOL AFOSR/NA

UNCLASSIFIED

MML TR 89-56c

HIGH-STRAIN-RATE BEHAVIOR OF HYDRATED CEMENT PASTE

FINAL REPORT

January 1, 198⁶~~7~~ - May 31, 1989

Contract No.: F49629-86-C-0021

Submitted to:

Air Force Office of Scientific Research
Bolling Air Force Base
Washington, D.C. 20332-6448

Submitted by:

A. Ritter, G. Childs, K. Bridger, S. Winzer

Martin Marietta Laboratories
1450 S. Rolling Road
Baltimore, Maryland 21227-3898

and

D. Barker and R. Dick
Department of Engineering
University of Maryland
College Park, Maryland 20742

May 1989

EXECUTIVE SUMMARY

Responding to an Air Force interest in understanding how concrete fails when exposed to dynamic loads, Martin Martin Laboratories, in collaboration with the University of Maryland, performed a three-year study of the high-strain-rate (HSR) behavior of hydrated cement paste and mortar. The objective of this program was to determine the microstructural response of cement when subjected to well characterized dynamic loads. Although concrete is the ultimate material of interest, its complexity, and the resources of this program, required a simplified approach. For those reasons, the research effort focussed on cement paste as the most important, but least understood constituent, of the concrete system.

Plane-stress testing at low and intermediate strain rates (10^{-3} to 10^3 s^{-1}) and at pressures to 2 kbar was done to examine the material response of Types III and IV cement pastes prepared with varying water to cement (w/c) ratios to provide a suite of materials with a range of porosity. At these strain rates and peak loads the cement samples remained in the elastic-brittle response regime. Dynamic yield strengths were measured and reviewed as a function of strain rate, cement type and w/c, and curing time. The yield strengths were directly dependent on strain rate and curing time (degree of hydration) and inversely related to the sample porosity. Type III cement had higher strengths at all strain rates (up to 10^3 s^{-1}) relative to Type IV pastes of similar age, because of differences in the degree of hydration. Scanning electron microscopy (SEM) of fracture surfaces of cement that failed during plane-stress testing showed that brittle fracture was the dominant failure mechanism. At low and intermediate strain rates, fracture paths occurred preferentially in the major hydrated cement paste, calcium-silicate-hydrate (C-S-H). At intermediate strain rates, 10^2 - 10^3 s^{-1} , an increased amount of fracture across basal planes of calcium-hydroxide (C-H) was also noted.

The Hugoniot elastic limits (HEL) of Type III paste and mortar were measured by impacting instrumented specimens with a gas-gun-driven flyer plate. Average HEL's were found to be approximately 5 kb and were related to

the amount of porosity and the peak pressure (a function of strain rate) induced in the sample.

Type III cement paste and mortar samples were loaded with planar explosively formed shock waves to pressures within the elastic-plastic (or perhaps, fully plastic) material response regime, i.e., pressures to 150 kbar and strain rates up to 10^5 s^{-1} . Specimens were recovered, using impedance-matched momentum traps, for microstructural characterizations that included X-ray diffraction (XRD), scanning electron microscopy (SEM), and mercury porosimetry. Significant failure mechanisms observed include a) micro-cracking, b) particle size reduction and/or lattice distortion, c) dis-ordering of semicrystalline C-S-H, d) granulation of C-S-H, and e) alteration of the pore size distribution by modification and/or elimination of capillary porosity.

More work is needed to determine causes of the observed microstructural changes, specifically by establishing relationships between shock-induced changes and a) peak pressure and its duration, b) porosity, and c) effects of shear. More information can be obtained about the nature of such changes through the use of additional types of characterizations, such as infrared spectroscopy and transmission microscopy, and by employing computer models to design better shock recovery experiments and predict stress histories in recovered specimens.

TABLE OF CONTENTS

	<u>Page</u>
I. INTRODUCTION	1
II. MATERIAL SELECTION AND SAMPLE PREPARATION	6
III. PLANE-STRESS TESTING	9
A. LOW AND INTERMEDIATE STRAIN-RATE EXPERIMENTAL METHODS	9
B. CHARACTERIZATION OF TEST SAMPLES	11
C. RESULTS AND DISCUSSION	13
IV. PLAIN STRAIN EXPERIMENTS	23
A. OVERVIEW	23
B. CALIBRATION OF SHOCK-INDUCED PRESSURES	25
C. SHOCK RECOVERY: EXPERIMENTAL METHODS AND RESULTS	33
1. Methods	33
2. Results and Discussion	38
D. MICROSTRUCTURAL CHARACTERIZATION OF RECOVERED SAMPLES	43
1. Sampling Procedure	43
2. TGA Analyses	45
3. XRD Analyses	45
4. SEM Analyses	53
5. Mercury Porosimetry	66
E. DISCUSSION	83
V. CONCLUSIONS	87
VI. SUGGESTIONS FOR FUTURE RESEARCH	90
VII. REFERENCES	93

LIST OF FIGURES

	<u>Page</u>
Figure 1. Experimental matrix of tests conducted at low, intermediate, and high strain rates and pressures.	5
Figure 2. Schematic diagram of the SHPB set-up.	10
Figure 3. Typical strain-time history plot showing incident, reflected, and transmitted pulses.	12
Figure 4. Stress vs strain-rate curves for 0.25-, 0.33-, and 0.40-w/c ratios of a) Type III and b) Type IV cement pastes.	14
Figure 5. (a-h) Sequence of eight high-speed photographs showing dynamic failure of a cement specimen undergoing SHPB testing.	17
Figure 5. (continued)	18
Figure 5. (continued)	19
Figure 5. (concluded)	20
Figure 6. SHPB fracture surfaces showing a) fracture between hydrated and unhydrated particles, b) fracture propagation through C-S-H material, c) fracture across the basal plane, and d) fracture parallel to the basal plane.	22
Figure 7. Schematic of flyer-plate experimental set-up showing cross section of the target and pin hardware.	26
Figure 8. a) Schematic diagram of strain-gage assembly showing location of gages mounted on the specimen and b) photo showing the specimens mounted to the target plate.	28
Figure 9. Schematic of gas-gun-driven flyer-plate test to determine material response to peak pressures within the elastic plastic region of the test material.	29
Figure 10. Output upon initial impact of a) manganin gage on cement sample and b) PVF ₂ pressure gage on mortar sample at a depth of 5 mm beneath the impact surface.	30
Figure 11. Plot of pressure vs sample depth for cement and mortar samples conducted at Dynasen.	32
Figure 12. Schematic of the a) top and b) cross-sectional views of a sample in the impedance assembly.	35

LIST OF FIGURES (cont.)

	<u>Page</u>
Figure 13. Schematic of a) the first momentum trap design including the impedance assembly and b) the larger momentum trap design including the impedance assembly with the spall layers.	36
Figure 14. Shock pressure data from test C6. Top waveform: gage output (pressure) recorded between the buffer and the sample; bottom waveform: indicates pressure recorded between the sample and the anvil.	41
Figure 15. Recovered test samples from tests C5 through C7 and from C11 and C12. Intact samples were recovered from tests a) C6, b) C5, c) C11 and C12; sample fragments were recovered from d) C7.	44
Figure 16. TGA plots of unshocked and shocked a) cement and b) mortar samples ramped to 1000°C at a heating rate of 10°C/min.	46
Figure 17. Typical XRD scan of a) unshocked and b) shocked cement between 15-40 degrees.	48
Figure 18. XRD scans of a) unshocked and b) shocked cement paste at various times from initial casting.	52
Figure 19. Scanning electron micrographs of unshocked cement fragments showing typical microstructure: (a and c) and (b and d) are the references for shock recovery tests C6 and C5, respectively.	55
Figure 20. Scanning electron micrographs of fracture surfaces of shocked cement fragments showing compaction and granulation in response to shock recovery tests C6 (a and c) and C5 (b and d).	56
Figure 21. Scanning electron micrographs of cement microstructure showing a) angular porosity in an unshocked reference sample and (b-d) granulation and elimination of angular particles and porosity in shocked specimens.	57
Figure 22. Scanning electron micrographs of the reference cement paste for recovery tests C11 and C12 taken at (a) low and (b-d) high magnification. Note reduced amount of porosity relative to previously characterized reference paste for tests C5 and C6 (Fig. 19).	59
Figure 23. Scanning electron micrographs of fracture surfaces of fragments from the top outer edge of sample C11 showing typical features at (a) low and (b-d) high magnification.	60

LIST OF FIGURES (cont.)

	<u>Page</u>
Figure 24. Scanning electron micrographs of fracture surfaces of fragments from midway between the outer edge and center of the top of sample C11 showing typical features at (a) low and (b-d) high magnification. Note the relatively homogeneous texture dominated by rounded particles.	62
Figure 25. Scanning electron micrographs of fracture surfaces of fragments from the top center of sample C11 showing typical features at (a) low and (b-d) high magnification. Note the increased amount of porosity relative to the unshocked reference paste (Fig. 22).	63
Figure 26. Scanning electron micrographs (a-d) of fracture surfaces of fragments from the top center of sample C12 showing typical features at high magnifications.	64
Figure 27. Scanning electron micrographs of fracture surfaces of fragments from the bottom center of sample C12 showing typical features at high magnifications. Note fragmentation and rounding of corners of the C-H mineral (c and d) relative to the C-H in the reference paste (Fig. 22d).	65
Figure 28. Scanning electron micrographs of fracture surfaces of fragments of unshocked mortar for reference to recovery samples M5 and M6 showing typical features at (a) low and (b-d) high magnifications.	67
Figure 29. Scanning electron micrographs of fracture surfaces of fragments of recovered mortar anvils from tests M5 and M6 showing typical features at (a) low and (b-d) high magnifications.	68
Figure 30. Cumulative porosimetry data for unshocked and shocked cement pastes showing volumetric hysteresis effects.	70
Figure 31. Pore size distribution for two samples of a) reference cement R11/R12 and b) shocked cement (C11 and C12).	73
Figure 32. Pore size distribution of a) reference (fractured at low strain rate) and b) SHPB-tested samples.	78
Figure 33. Pore size distribution for a) reference (R11/R12) and b) shocked cement from test sample C11.	79
Figure 34. Pore size distribution for a) reference (R11/R12) and b) shocked cement from test sample C12.	80
Figure 35. Pore size distribution for a) reference (R5) and b) shocked cement from test sample C5.	81

LIST OF FIGURES (concluded)

	<u>Page</u>
Figure 36. Pore size distribution for a) reference (R7) and b) shocked cement from test sample C7.	82
Figure 37. Pore size distribution for a) mortar reference (M5) and b) shocked mortar sample from test M5.	84

LIST OF TABLES

	<u>Page</u>
Table 1. Phases in Types II and IV Portland Cement	6
Table 2. Characterization of Types III and IV Cement Pastes	13
Table 3. Data from Gas-Gun Tests on Cement and Mortar Material	15
Table 4. Summary of Shock Recovery Tests	39
Table 5. Principal Cement Peaks Used for XRD Analysis	49-50
Table 6. Porosity Data for Reference Cement Samples	75
Table 7. Porosity Data for Shocked Cement Samples	76

I. INTRODUCTION

The use of concrete as a basic structural material makes it increasingly important to improve both our understanding of its behavior and our ability to accurately predict its response under dynamic load. Although the behavior of concrete under static and quasi-dynamic loadings appears to be reasonably well understood, the same cannot be said about its behavior under dynamic tensile and compressive loadings. Predicting the structural response under such loading rates, and accounting for it, is of critical importance in the design of civilian structures, such as fallout shelters and nuclear containment structures, and military structures, such as bunkers, ammunition depots, and aircraft runways.

This research program, a collaborative effort of Martin Marietta Laboratories and the University of Maryland, attempted to address the above problem by starting with a single, but most important, constituent of concrete, namely, the hydrated cement paste. More specifically, we studied the relationship between the mechanical properties and microstructure of hydrated cement paste subjected to strain rates up to 10^5 s^{-1} and peak pressures up to 150 kbar.

Strain rates below 10^3 s^{-1} load the sample in plane stress because as the stress wave propagates, the material is allowed to expand radially. Strain rates above 10^4 s^{-1} are plane strain-type because they are so rapid that inertial effects prevent radial expansion, placing the material under hydrostatic stress.

In metallic materials, plane-stress experiments can be directly related to plane-strain experiments, since, in general, the yield strength of the material is independent of the hydrostatic pressure. That is, the yield strength is independent of the first invariant of stress and is a function of only the deviatoric stress components. In brittle materials such as rock, concrete, or ceramics, the yield strength is not independent of the

hydrostatic pressure, and there is no simple way to correlate the results of plane-stress and plane-strain experiments. This behavior results from the microstructural changes that take place at high-strain-rate (HSR) loadings. The most common change is the collapse of natural voids in the material, but other effects, such as phase changes, an increase in dislocation density or even melting also can occur under dynamic or shock loading. All of these changes are a function of the hydrostatic pressure.

The complexity of concrete, a composite material of hydrated cement minerals, fine and coarse aggregates, chemical additives, and water, makes it very difficult to isolate microstructural changes during HSR loading. The mechanical properties of individual phases and their bond strength are known only marginally. To fully understand what microstructural changes occur and how they influence the dynamic yield strength, we must know the constitutive equation under HSR loading. This relation is known for some of the minerals commonly used in concrete mixes and can be correlated with irreversible changes in the material induced by increasingly strong shock pulses.

Defining constitutive equations for all constituents of concrete is a formidable task and outside the scope of this project. To succeed even in part, the large problem (the concrete system) can be broken down into smaller, more tractable portions that could be addressed with the resources available. As mentioned above, data exist for rocks and minerals, i.e., quartz and calcite, commonly used in concrete. Similar data do not exist for the hydrated cement paste; therefore, concentration on this part of the problem was needed.

The complexity of the cement paste itself may also have limiting effects on obtaining dynamic response data. Hydrated cement paste consists primarily of C-S-H (about 70%), C-H (about 20%), calcium sulfoaluminate hydrates, other minor hydrated phases (about 7%), and some still unhydrated cement. Since C-S-H makes up the bulk of the hydrated matrix and contains most of the fine porosity, it should have the greatest effect on paste properties. C-S-H is considered to have a degenerate clay structure, i.e., a

layered structure, in which water plays an important role. Water is held in C-S-H in a variety of ways, including bulk water in capillary pores, water physically absorbed on or between the surfaces that constitute the layers in the structure, water structurally associated with the solid (interlayer water), and hydroxyl water in the solid lattice.[1] As water is removed from the C-S-H, some rearrangement of the structure takes place. For example, loss of water from capillary pores is believed to induce compressive stress on the C-S-H system due to surface tension effects, and loss of water between layers or from the surface changes the potential for bonding (ionic-covalent, van der Waals, or interlayer). Changes in bonding could cause permanent changes in the structure. There is also considerable evidence that the presence or removal of water has an important effect on the strength and fracture behavior of cement paste.[1]

Martin Marietta has attempted to document and understand the effects of dynamic loading on hydrated cement paste. This understanding, in turn, can be used to develop concrete with better dynamic properties. During the first year of our study, we investigated the microstructural response in plane stress. A split Hopkinson pressure bar (SHPB) was used to generate high strain rates up to 10^3 s^{-1} and peak pressures up to 2 kb in cement samples of various water-to-cement ratios (w/c). These studies confirmed that both the mechanical and microstructural response to SHPB loading for each type of cement were similar at similar degrees of hydration, and that brittle fracture was the primary mode of failure. Elastic compression and elastic shear waves with complex reflections are generated only in the later stages of the loading event.

Second-year efforts concentrated more on the microstructural effects of Type III hydrated cement paste in plane strain. Flyer-plate impact tests were conducted at Los Alamos National Laboratories (LANL), the University of Dayton Research Institute (UDRI), and at Dynasen, Inc. (an independent impact testing laboratory). Shock-loading impact tests generate two types of loading pulses, high-amplitude elastic waves and high-amplitude plastic waves. Points along the equation of state curve, i.e., the Hugoniot elastic limit (HEL), and

points within the elastic-plastic region were determined from these tests. Wave amplitudes and velocities were found to diminish (attenuate) quite rapidly as they propagate through the sample.

Contact explosives were used to generate strain rates up to 10^5 s^{-1} and peak pressures exceeding 150 kb in the 0.25 w/c paste during the third year of our efforts. The cement material was expected to be above the HEL and well into the elastic-plastic region at these strain rates and peak pressures. The test matrix was extended to include mortar, a Type III cement with silica (quartz) sand, during the latter part of the third year (Fig. 1).

CEMENT TYPE	W:C RATIO	MTS	SHPB	GAS GUN	EXPLOSIVES
TYPE III					
	0.25	●	●	●	●
	0.33	●	●	●	
	0.40	●	●	●	
TYPE IV					
	0.25	●	●		
	0.40	●	●		

$10^{-4} / s$  $10^6 / s$
 STRAIN RATE

Figure 1. Experimental matrix of tests conducted at low, intermediate, and high strain rates and pressures.

II. MATERIAL SELECTION AND SAMPLE PREPARATION

There are several types of portland cement, including formulations to achieve various early or late strengths, curing rates, ultimate strengths, and reactivities with aggregate. The principal differences between types are the contents of the unhydrated cement minerals, i.e., of di- and tri-calcium silicates (C_2S and C_3S), and the (smaller) variations in tricalcium aluminate (C_3A), ferrite solid solution (Fss or C_4AF), and calcium sulphate. Types III and IV portland cements represent the extremes in phase compositions (as shown in Table 1) and therefore were selected as baseline materials for this study.

TABLE 1
Phases in Types III and IV Portland Cement^a

<u>Phase</u>	<u>Type III (wt%)</u>	<u>Type IV (wt%)</u>
C_3S	60	25
C_2S	15	50
C_3A	10	5
C_4AF (Fss)	8	12
CSH_2	5	4

^a Calculated using the Bogue equation

Type III cement is described as an early strength cement because of the fast hydration of the C_3S phase.[2] Type IV cement is a specialty cement noted for its sulfite resistance and does not develop strength quickly because of the higher proportion of C_2S , a slower hydrating mineral.

Hydrated cement samples from Types III and IV paste were prepared using different w/c's to obtain a range of microstructures (primarily porosity) in the paste. Theoretically, cement would require approximately 20-25% by weight of water for complete hydration, provided every cement grain had unrestricted access to water. However, because of the nature of the hydration reactions and the desire to make the cement paste workable, more water is needed. As

the w/c increases, the microstructure becomes increasingly porous. Water-reducing additives, e.g., lignosulfonate dispersants, can decrease the water requirement, maintain workability, and result in low-porosity microstructures.

Hydrated cement or concrete must also be properly cured if its optimum reproducible properties are to be developed. An adequate supply of moisture is necessary to ensure that hydration is sufficient to reduce porosity to a level such that the desired strength and durability can be attained. Proper curing methods require sufficient time for most cement minerals to hydrate and thus develop a strong material. We used a minimal 28-day period of wet curing in lime solution, the ASTM standard procedure for curing hydrated pastes and concrete,[3] which is considered adequate for a meaningful test of strength and other mechanical properties. Properly cured concrete generally gains about 75-80% of its ultimate strength in 28 days; the additional 20-25% strength gain possibly takes over a year.[4]

To obtain a range of microstructures, we prepared Type III and Type IV cement pastes with varying w/c's (0.25, 0.33, and 0.40), according to ASTM STP C305, for low and intermediate strain-rate testing. The 0.25 w/c mixture contained 1% calcium lignosulfonate (by weight of cement) as a water reducer. After mixing, the cement paste was immediately cast into clean Plexiglas molds and vibrated at medium-to-high intensity on a Syntron vibrating table for 10 minutes. The mold was wrapped in plastic and allowed to set for about 24 hours before being immersed in a saturated limewater bath to cure for 28 days at room temperature. During the curing process, i.e., about 14 days after casting, samples were cored using a precision diamond core drill and precisely machined on a lathe to a specified length and diameter. The samples were continuously exposed to water during the coring and machining process to prevent shrinkage cracks. After machining, the samples were returned to the saturated limewater solution for continued hydration.

Samples for the instrumented gas-gun impact experiments were also prepared as above. However, only Type III paste was used. Mortar samples were prepared using Type III paste (0.25 w/c) mixed with 45 wt% clean F125

quartz sand. The samples were cured in lime-saturated water for 28 days, machined to the appropriate thickness and diameter, and then air dried several weeks before testing.

Samples for shock recovery HSR testing were also made using only Type III portland cement with $w/c = 0.25$ as both paste and mortar. Two weeks after casting, samples were cored and machined to have a 25-mm diameter and a 15-mm thickness. Samples were continuously exposed to water during the coring and machining process to prevent shrinkage cracks, and were returned to a saturated limewater solution after machining for continued hydration. Hydration was stopped 35 days after casting by holding the samples at 80°C for 10 hours under vacuum. They were then placed in a desiccator to prevent further hydration.

III. PLANE-STRESS TESTING

A. LOW AND INTERMEDIATE STRAIN-RATE EXPERIMENTAL METHODS

Plane-stress testing of hydrated cement paste was done at low and intermediate strain-rates to investigate changes in material response within the purely elastic loading regime. The primary relationship studied was that of the dynamic yield strength with cement microstructure.

Obtaining the dynamic yield strength in plane stress was relatively straightforward. Specimens were loaded using either a conventional servo-hydraulic testing machine (MTS, Inc.) at strain rates up to 10^0 s^{-1} or a SHPB at strain rates up to 10^3 s^{-1} and peak pressures of 2 kb. The SHPB (Fig. 2) consists of two long bars, commonly referred to as the incident bar and the transmitter bar, between which the sample is located. To load the test sample, a compressive stress wave of uniform intensity is generated in the incident bar by impacting its end with a striker bar or projectile of the same material and diameter. This procedure allows an impulse to travel along the bar into the sample.

From simple one-dimensional wave mechanics, the stress and strain in the sample, σ_s and ϵ_s , can be calculated at any point in time from measurements of the transmitted elastic strain wave in the transmitter bar, ϵ_t , and the reflected strain wave in the incident bar, ϵ_r , as

$$\sigma_s = EA\epsilon_t/A_s \quad (1)$$

and

$$\epsilon_s = -2C_0/L_s \int_0^t \epsilon_r dt \quad (2)$$

where E is the Young's modulus, A and A_s are the cross-sectional areas of the bar and sample, respectively, L_s is the length of the sample, and C_0 is the longitudinal wave velocity within the bars. The average strain rate can be calculated as

$$\dot{\epsilon}_s = -2C_0\dot{\epsilon}_r/L_s. \quad (3)$$

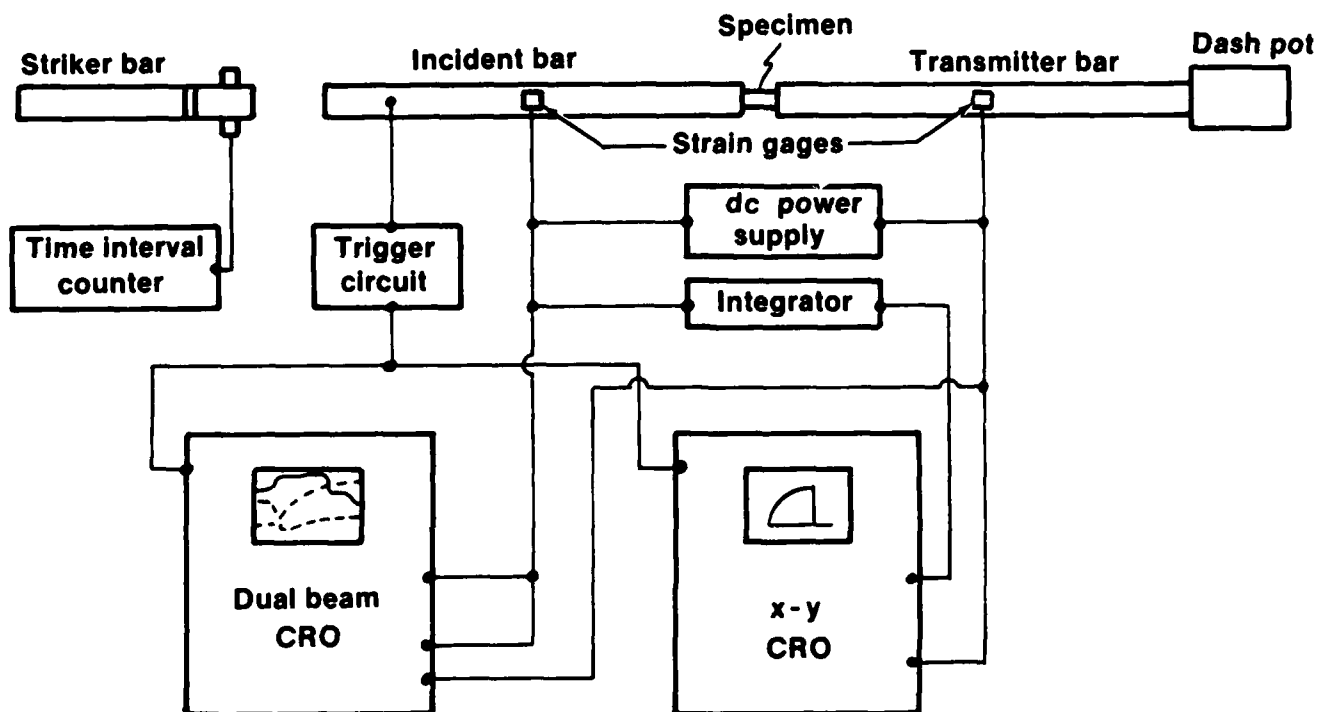


Figure 2. Schematic diagram of the SHPB set-up.

Thus, from one experiment, it is possible to generate a complete dynamic stress-strain plot of the sample material at a given strain rate. This plot naturally provides the yield and ultimate strengths or failure stress for a particular strain rate.

A Nicolet 2090 digital oscilloscope and two Micro-Measurements BAM-1B dynamic bridge amplifiers provided instrumentation for the SHPB apparatus. Two strain gages each were mounted on the incident and transmitter bars to measure elastic waves after projectile impact. A typical wave output is shown in Fig. 3. Fragmented samples from the MTS and SHPB tests were stored in a dessicator and later characterized for degree of hydration, porosity, and morphological changes in the hydrated paste.

B. CHARACTERIZATION OF TEST SAMPLES

The degree of hydration was estimated as the chemically bound non-evaporable water in the cement paste, as indicated by weight loss upon heating. For this determination, the paste was ground, washed several times with acetone, oven dried at 105°C for about 24 hours, and then ignited at 1000°C for 1 hour. The resulting weight loss was taken as a measure of the degree of hydration of the cement.

Mercury intrusion porosimetry was used to estimate the percent porosity of the specimens. In this technique, mercury is forced into the pore system of the paste under external pressure. The pressure required is inversely proportional to the pore radius. This technique provides better information about the capillary pores of the system than other techniques -- an important feature since the capillary porosity of the cement paste is inversely related to its compressive strength.[4] Measurements were made on oven-dried pieces of hydrated paste with a Micrometrics Model 9300 pore sizer. More details of the porosimetry analyses are presented in Section IV.

Scanning electron microscopy (SEM) was used to examine microstructural

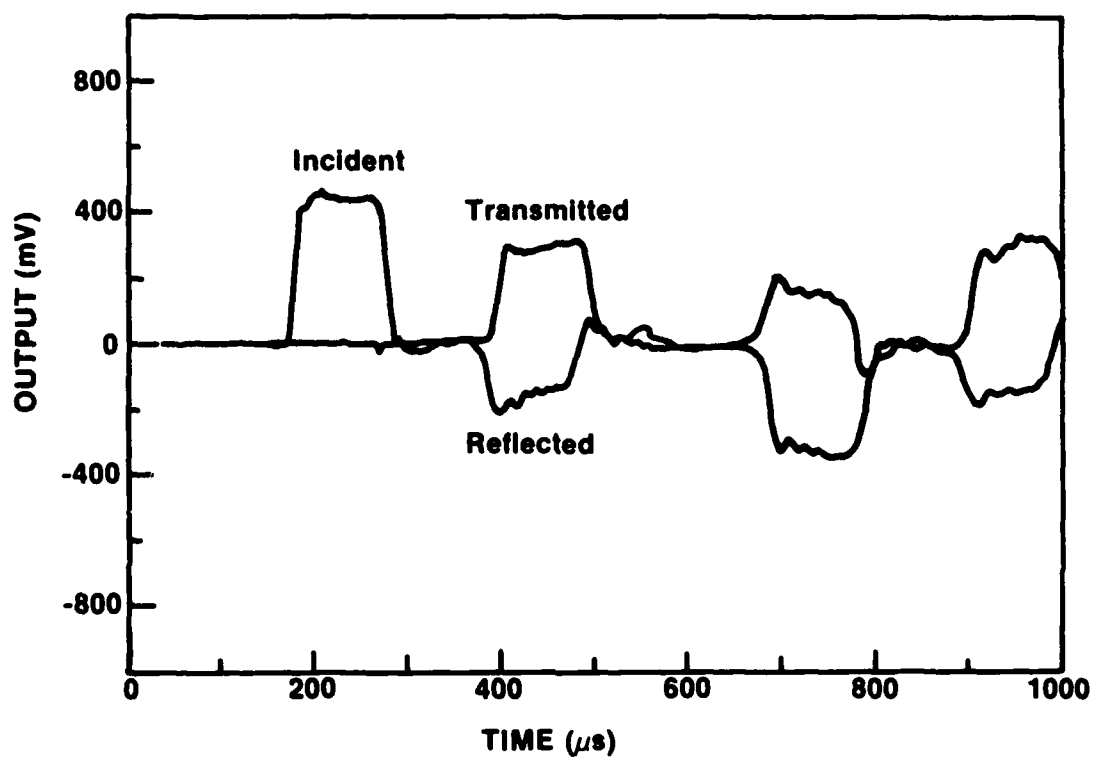


Figure 3. Typical strain-time history plot showing incident, reflected, and transmitted pulses.

changes in the cement paste before and after MTS and the SHPB tests. A JEOL Model JSM 35-CF scanning electron microscope was used.

C. RESULTS AND DISCUSSION

High strain-rate SHPB testing of 28-day-old cement paste was conducted at the University of Maryland under the direction of Dr. Donald Barker. As shown in Fig. 4, two major differences were observed between the HSR response of Type III and Type IV cement pastes: the Type IV cement pastes were less strain-rate sensitive than the Type III cement pastes (note the sharp increase in strength of Type III pastes at $\sim 10^2 \text{ s}^{-1}$ strain rates) and they also showed lower strength at specific strain rates than the Type III pastes with the same w/c ratio. The differences in strength were correlated with significant differences in their degree of hydration, as Table 2 shows. At equivalent hydration, the strengths of the Type IV and Type III cement samples were comparable at each w/c ratio tested. For example, when 0.25 w/c and 0.40 w/c Type IV pastes had hydrated approximately 75-80%, their ultimate strengths averaged 260 MPa (38 ksi) and 179 MPa (25 ksi), respectively, at average strain rates of 900 s^{-1} . Type III pastes with the same w/c ratios and hydration had the same average strengths, i.e., 260 MPa (38 ksi) and 151 MPa (22 ksi), respectively. The strength of Type III and Type IV pastes correlated directly with the bulk porosity of the cement paste, which was affected by the w/c ratio as shown in Table 3.

Table 2
Characterization of Types III and IV Cement Pastes

w/c Ratio	Stress $\times 10^3$ Strain rate - 10^3 s^{-1} (MPa)	Porosity (%)	Hydration (%)	Median Pore Size ^a (μm)
<u>Type III</u>				
0.25	260	15.2	75	0.019
0.33	200	18.3	76	0.021
0.40	170	22.2	82	0.035
<u>Type IV</u>				
0.25	260	15.5	50	0.020
0.40	151	23.5	54	0.030

^a Determined at 50% of the total intruded volume

TABLE 3

DATA FROM GAS GUN TESTS ON CEMENT AND MORTAR MATERIAL

(Conducted at LANL, unless otherwise noted)

Material	w/c Ratio (%)	Gage Depth (mm)	Projectile Velocity (mm/ μ s)	Peak Pressure (kbar)	Average HEL
Cement	25	9	0.10	3.8	
"	25	18	0.10	3.4	2.9
"	25	27	0.10	3.3	
"	25	9	0.24	8.5	
"	25	18	0.24	5.3	5.0
"	25	27	0.24	4.0	
"	25	6 ¹	Unknown	15.0 ²	5.9
"	25	5	0.90	56.0 ²	
"	25	10	0.90	47.0 ²	9.0 ³
"	25	15	0.90	41.0 ²	
<hr/>					
Cement	33	9	0.10	5.1	
"	33	18	0.10	4.6	3.3
"	33	27	0.10	3.4	
<hr/>					
Cement	40	9	0.10	2.0	
"	40	18	0.10	1.9	1.6
"	40	27	0.10	1.3	
<hr/>					
Mortar	25	5	0.90	41 ²	
"	25	10	0.90	33 ²	4.0
"	25	15	0.90	27 ²	

¹ Test conducted at UDRI, Dayton, OH, only 1 HEL measurement.

² Test conducted at Dynasen, Inc., Goleta, CA; are an average of 3 pressure gages.

The SHPB testing procedure was also evaluated to ensure that the test results were not influenced by artifacts of the technique. Higher strain-rates were achieved in our tests by either varying the impact velocity or changing the sample size. Sample geometries were varied from 3/4 inches to 1/4 inches in diameter while maintaining a constant length-to-diameter ratio. Additional testing concentrated only on varying the strain rate by changing the impacting projectile velocity, i.e., the magnitude of the input stress pulse, rather than changing sample size. The results of the additional testing confirmed those obtained previously and showed that the strength data are indeed a function of strain rate and not significantly influenced by sample size.

Uniform loading of the cement samples during the SHPB tests was evaluated by using a Beckman and Whitney high-speed framing camera (20,000 frames/s) as shown in Fig. 5. Figure 5 (a) has been arbitrarily labeled time zero because it is the first frame that shows an indication of loading. Actually the loading pulse had arrived prior to this frame but after the previous frame, which, at these framing rates, represents an uncertainty of 50 microseconds. Figure 5 (b) was taken 50 microseconds after time zero. It is obvious from the increase in diameter of the specimen that the sample has failed. The remaining photos show how the cement sample breaks up after initial failure. The final photograph, taken at 500 microseconds from time zero, shows relatively uniform fragmentation of the sample, which we interpret as indicative of relatively uniform loading. However, there are also features in the series of photographs that indicate some stress concentration in the sample, e.g., a large shear failure that can be seen in the upper left corner of Fig. 5 (c). The developing shear plane may indicate nonparallelism of the loading surfaces, which could cause premature failure of the test specimen. By following this failure through the series of photographs, it is evident that although the shear fracture is a major one, material above and below it is well fragmented. If the shear failure occurred prematurely, sections of the test specimen would be isolated from the loading pulse and would not show significant fragmentation. This analysis supports the contention of a generally uniform loading pulse.

a)



b)

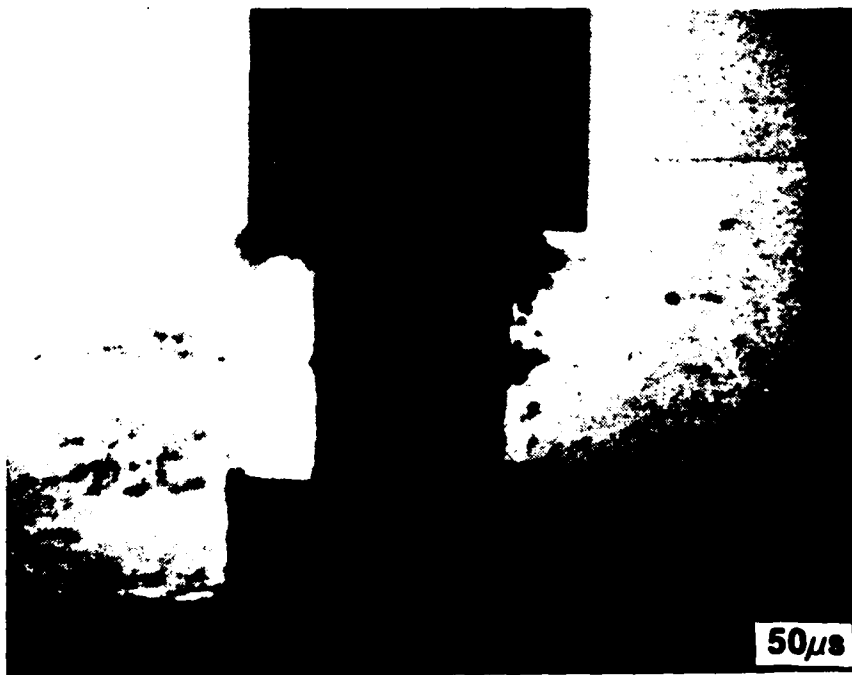


Figure 5. (a-h) Sequence of eight high-speed photographs showing dynamic failure of a cement specimen undergoing SHPB testing.

c)



d)

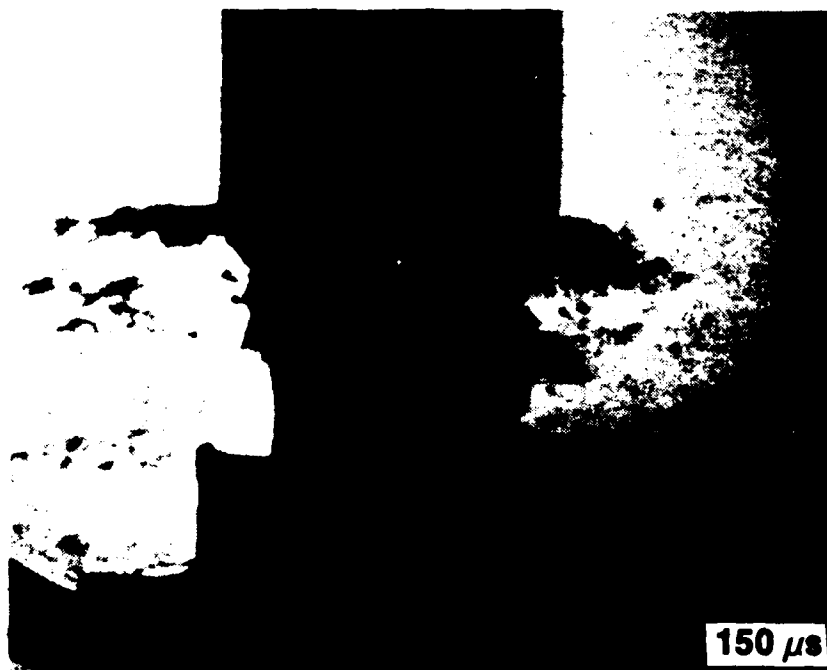


Figure 5. (continued)



Figure 5. (continued)

g)



h)



Figure 5. (concluded)

The specimens were examined by SEM after the SHPB tests and compared with those that had not been mechanically tested to determine the microstructure of the fracture surfaces and any possible morphological changes as a result of loading. The fracture surface consisted predominantly of the C-S-H phase and contained very little C-H. This was observed at all w/c ratios. In fully hydrated cement paste, C-H would constitute about 20-25% of the hydration products. For our pastes, with approximately 70-80% degree of hydration, we had expected at least 10-15% of the fracture surface to consist of C-H if the microstructure did not fracture preferentially. In some instances, cracks were also seen between the hydrated and unhydrated cement particles, as shown in Fig. 6 (a). Figure 6 (b) shows a crack propagating through the C-S-H phase.

Previous studies [5-7] on crack propagation in cement pastes under static loading have indicated that in the early stages of hydration, C-S-H is the softer phase in the paste and, therefore, the more likely region to fracture. As the paste matures, the strengths of C-S-H and C-H probably become similar so that there is no particular region in which cracks preferentially propagate. Our data suggest that even after 28 days, thus a relatively mature paste, fracture preferentially occurs through the more porous C-S-H. This behavior was observed at both low and high rates of loading. The specimens did occasionally show fracture across the C-H basal plane [Fig. 6 (c)], but usually fractured parallel to them [Fig. 6 (d)]. The latter mode of fracture was found to be more common at higher strain rates. Additional examinations were conducted using x-ray diffraction (XRD) and differential thermal analysis (DTA). However, these two techniques did not, or were unable to, reveal any changes in the nature and crystallinity of hydration products.

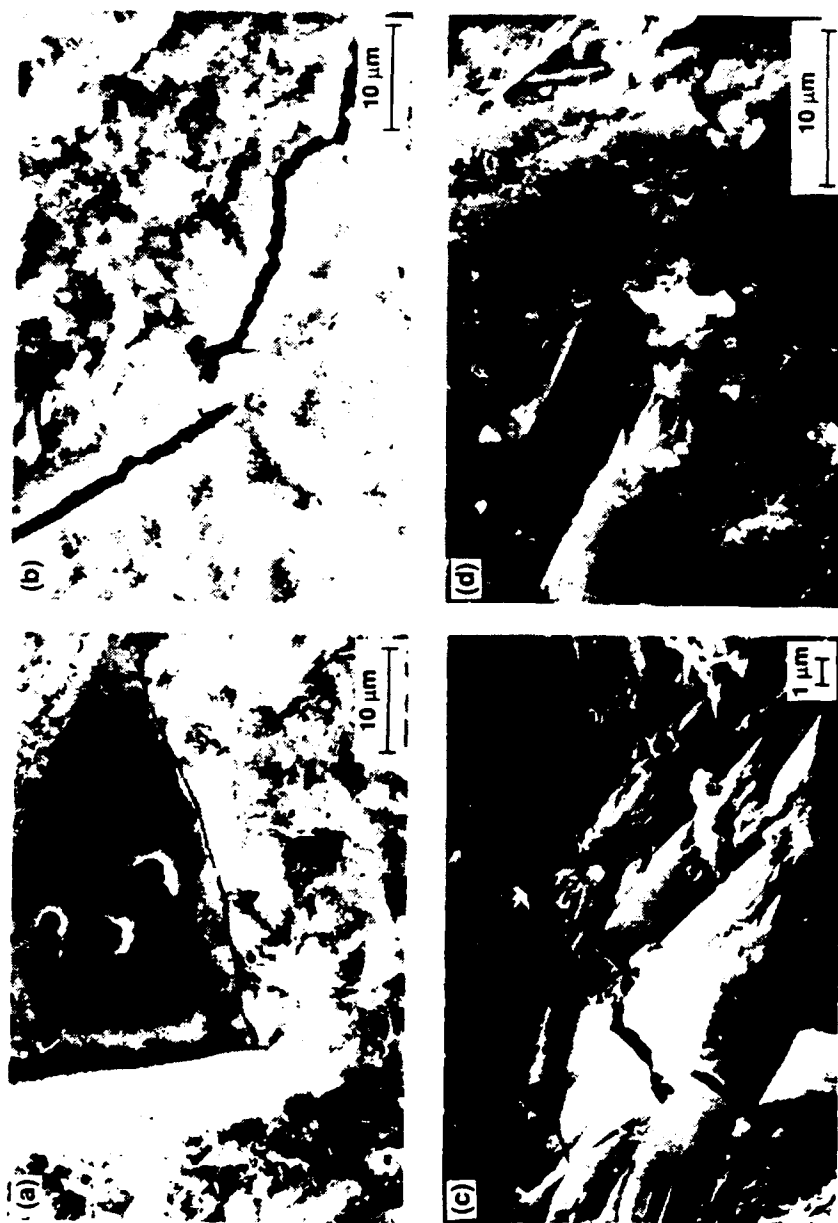


Figure 6. SHPB fracture surfaces showing a) fracture between hydrated and unhydrated particles, b) fracture propagation through C-S-H material, c) fracture across the basal plane, and d) fracture parallel to the basal plane.

IV. PLANE STRAIN EXPERIMENTS

A. OVERVIEW

The plate impact or shock type of experiment is not often used for determining dynamic mechanical properties of materials. It is more commonly used by solid-state physicists to determine electrical and chemical properties of high-pressure thermodynamic equations of state. However, using plate impact experiments in a mechanical behavior study allows application of extremely high strain-rates and peak pressures and ensures an exact, well-defined state of strain for the duration of the experiment. The technique also has several disadvantages: both very precise measurements and relatively large sample sizes are necessary and the cost per experiment is high. Perhaps the largest disadvantage is the difficulty in recovering a brittle sample with known loading history after intense shock loading, which is required in order to characterize the shock-induced microstructural changes, the basis for this study.

Conceptually, the plane-strain experiments are quite simple. The sample material is subjected to a sharp, impulsive load through either direct contact with an explosive or impact with a flying plate. The impulsive loading creates a uniform, uniaxial strain response in the central region of the target material, and the resulting structure of the induced wave is a function of the peak pressures reached. If the induced peak pressure is only slightly greater than the elastic limit of the material, the loading produces two different waves: a faster traveling elastic precursor wave followed by a slower plastic wave. The elastic wave travels at the dilatational wave velocity

$$c_E = \{E(1-\nu)/[\rho_0(1-2\nu)(1+\nu)]\}^{1/2} \quad (4)$$

where E and ν are the elastic modulus and Poisson's ratio, respectively, of the sample and ρ_0 is the initial density of the samples. The plastic shock wave travels at

$$c_p = ((\sigma_B - \sigma_{HEL}) / [\rho_{HEL}(\epsilon - \epsilon_{HEL})])^{1/2} \quad (5)$$

where σ_B is the loading stress on the material above the HEL (or dynamic yield strength of the material in plane strain), and σ is the amplitude of the elastic wave. The $(\epsilon - \epsilon_{HEL})$ term is the amount of plastic deformation in the sample, i.e., ϵ_{HEL} is the strain on the sample at the HEL and ϵ is the strain corresponding to the loading stress, σ_B , above the HEL of the material. The term ρ_{HEL} is the density beyond the elastic limit of the material.

The details (shape) of the wave structures and velocities are a function of the load on the material as well as the stress-strain constitutive relation of the material. As the wave reflects from the free surface at the back of the target plate, the changes in the wave shape determine the resulting velocity time history of this free surface. By measuring this velocity time history and inputting it into a complete wave-propagation analysis of the target, we can obtain the stress-strain constitutive relation of the target in an indirect iterative manner, i.e., through successive changes in the impacting pressure. More detailed analyses of plane strain testing have been reported previously.[8]

There are two techniques used in shock-type experiments. In the flyer plate technique, a gas gun can generate peak pressures up to about 100 kbar, depending upon target and flyer materials and the maximum velocity of the gun used. Similarly, equal, and even higher, pressures can be obtained by generating a plane-wave detonation front in an explosive directly in contact with the target. Both techniques require great care in developing the planar impulsive wave to propagate into the target sample.

Of the two techniques, the gas gun is more common. With it, a known and repeatable pressure wave can easily be generated. However, it requires very expensive specialized equipment and instrumentation. Alternatively, the explosive technique does not generate a pressure wave with as well known characteristics and repeatability, but it requires no specialized capital equipment. Its only difficult requirement is the availability of a firing

facility that can handle relatively large amounts of explosive. Both techniques are amenable to specimen instrumentation, such as with stress gages, but sample recovery is much easier in explosive testing since samples can be embedded in large momentum traps. With gas gun tests, the sample is precisely aligned at the muzzle of the gun in a special evacuated chamber that is not designed to contain momentum traps, but only to slow down the launching projectile, flyer, and target after impact. Sample recovery of very brittle materials with a gas gun is very difficult and is not possible without extraordinary effort.

B. CALIBRATION OF SHOCK-INDUCED PRESSURES

Gas gun experiments were used to determine the plane-strain dynamic yield strength, i.e., HEL, as the primary macroscopic material property and the pressure-shock velocity relationships for calibration of explosive sample recovery tests. A stress gage placed on the back of the target allows more accurate measurement of the elastic limit because of the nature of the wave induced by the impact. High-velocity gas guns generate very different loading pulses within the sample than those generated using a SHPB. Whereas the SHPB generates elastic compressive and elastic shear waves, gas guns generate high-amplitude shock-loading pulses as well as elastic waves. At impact loads near the elastic limit of the material, the elastic wave travels faster than the plastic or shock wave, and the amplitude of this elastic precursor wave is the dynamic yield strength of the material. Pressure gages allowed the direct measurement of the amplitude of the elastic precursor.

A typical flyer-plate experimental set-up using a gas gun is schematically shown in Fig. 7. The flyer plate is bonded to a long projectile body and is propelled into the target plate at the desired velocity by compressed gas. The precise impact velocity is determined by the projectile shorting slender charged pins that protrude at accurately known distances from the surface of the target plate. The simultaneity of the impact is determined by four additional charged pins positioned flush with the impact surface. The shock velocity and particle velocity in the target material are then measured

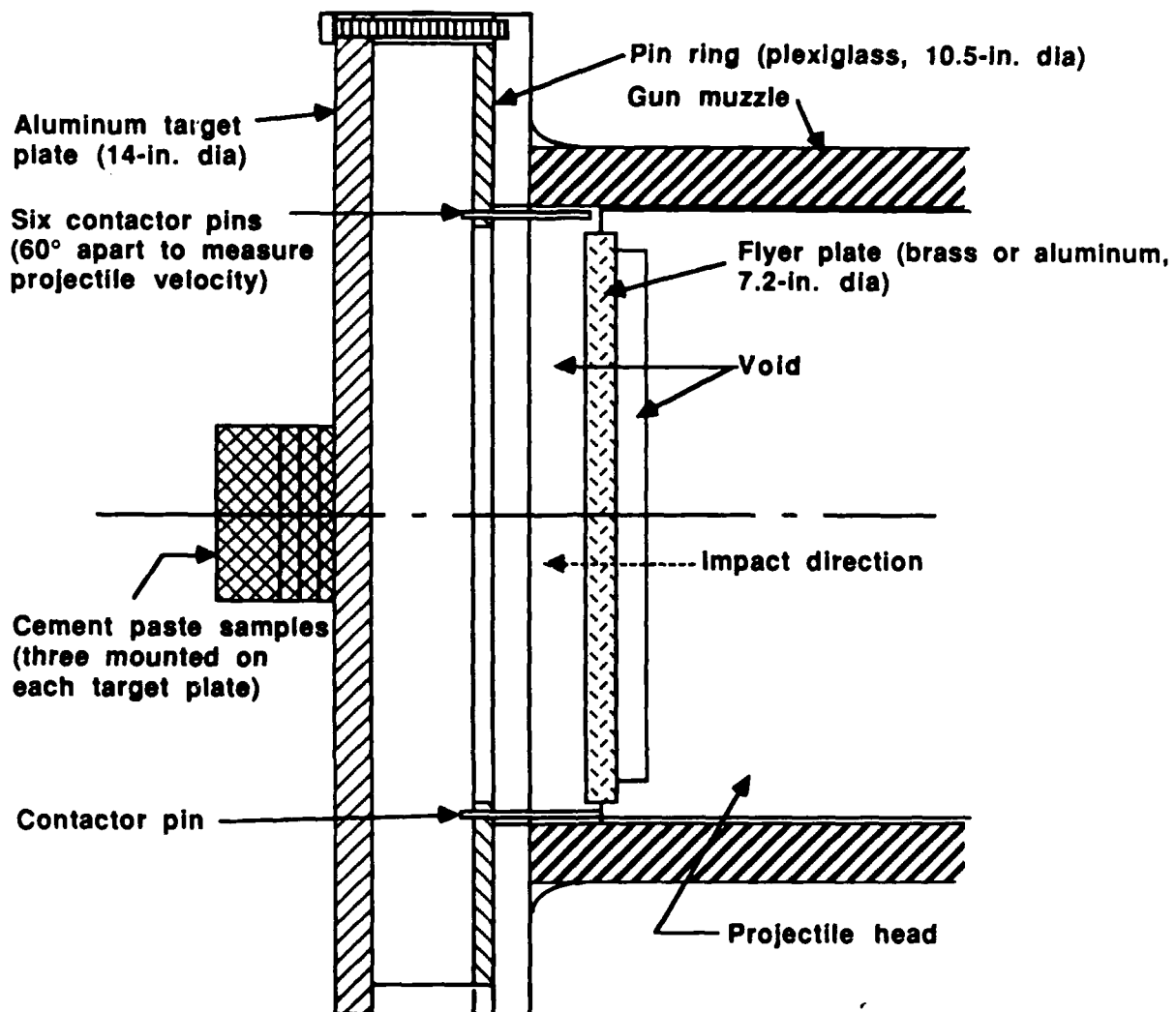


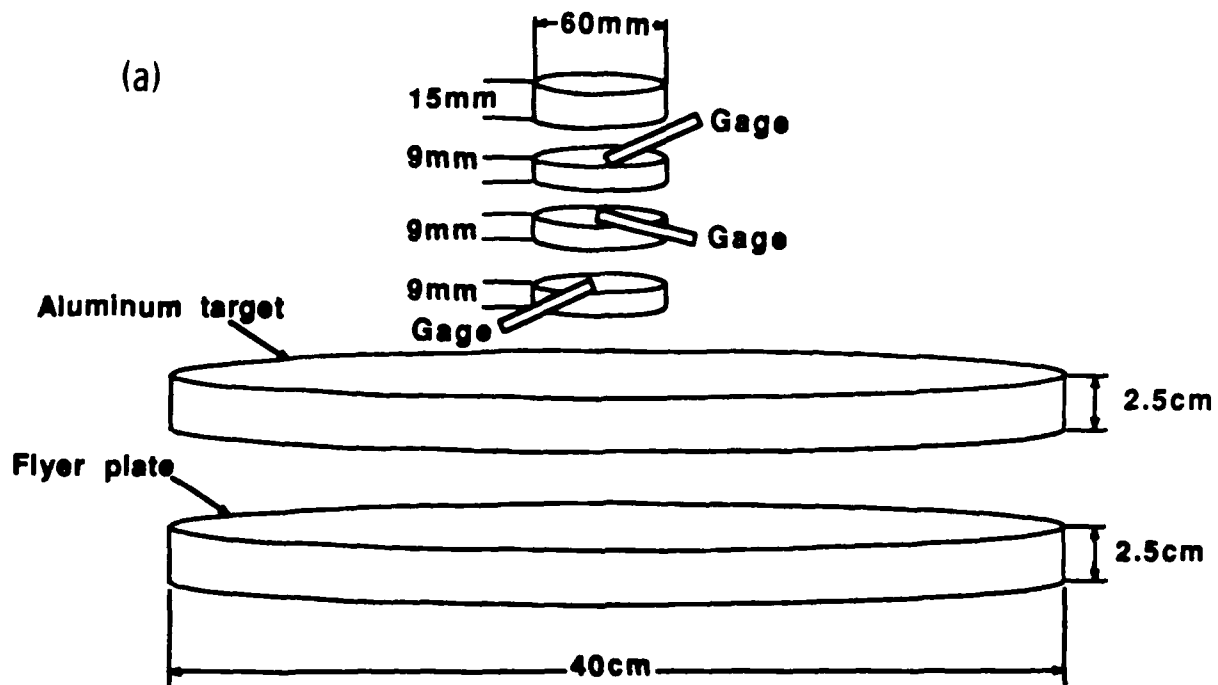
Figure 7. Schematic of flyer-plate experimental set-up showing cross section of the target and pin hardware.

in a variety of ways, and these values are used to describe the dynamic stress-strain behavior of the material.

Gas-gun impact tests were conducted primarily at Los Alamos National Laboratory (LANL) under the direction of Dr. R. Dick, at University of Dayton Research Institute (UDRI) under the direction of Dr. N.S. Brar, and at Dynasen, Inc. The gun at LANL has a smooth bore, is 20 mm in diameter, and is 3.5-m long. The standard projectiles are dog-bone shaped and weigh approximately 12 kg, excluding the flyer plate. Impact velocity is controlled by varying gun pressure and flyer-plate material.

Each LANL test sample (#G025 and #G026) contained three cylindrical specimens from each of the three w/c ratios and had carbon stress-gages embedded at three different locations to measure the stress history. Test samples (60 mm in diameter) were prepared by mounting a 9-mm-thick disk to the target plate and then bonding sequentially a carbon gage, a second 9-mm-thick disk, a second carbon gage, a third 9-mm-thick disk, a carbon gage, and finally, a 15-mm-thick disk as a backing piece. Epoxy was used to bond the disks and gages together and to the target plate (see schematic diagram of the strain-gage assembly in Fig. 8). Although thin cement samples (15-mm thick) were used in the instrumented tests to increase the probabilities of obtaining a gage record, their use precluded sample recovery.

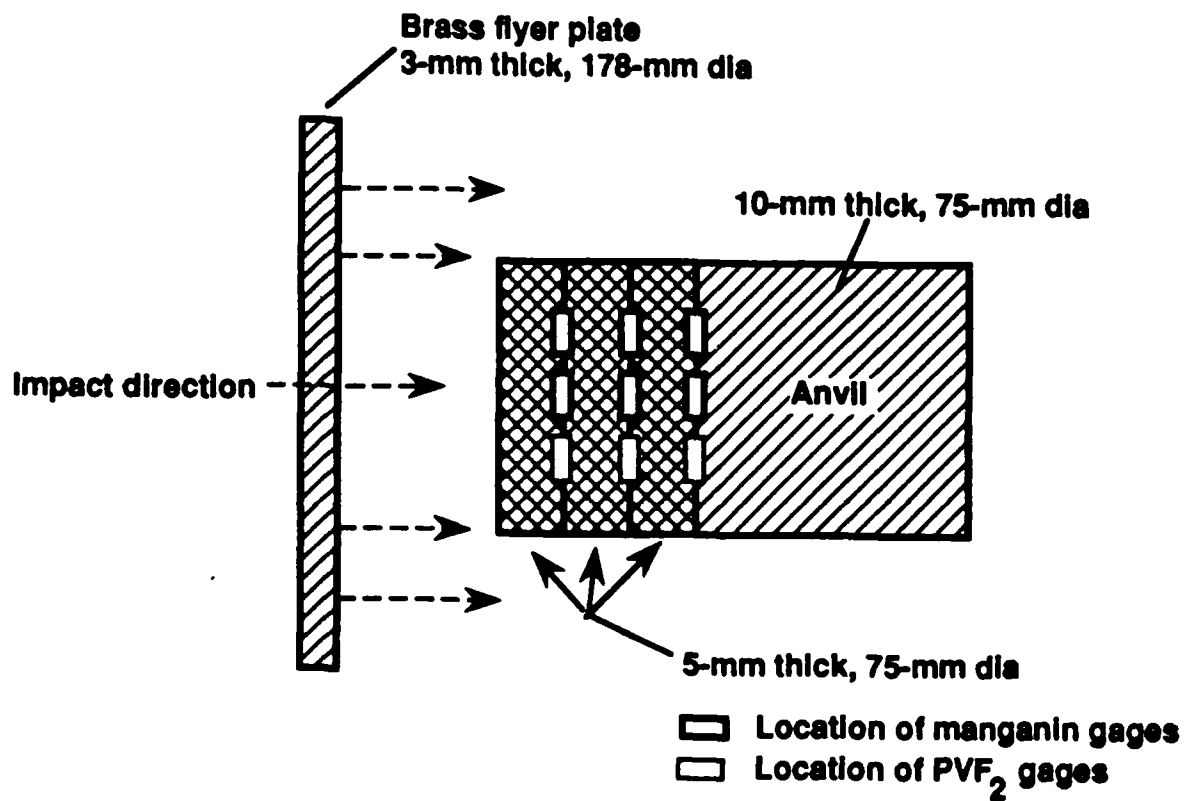
Additional gas gun tests were conducted at higher peak pressure by Dynasen, Inc. (Goleta, CA) to locate points on the equation-of-state curve within the elastic-plastic region. Two test samples, one mortar and one cement paste, were prepared (see Section II) and shipped to Dynasen where they were assembled with embedded gages. The samples were assembled from three 5-mm-thick disks and a 10-mm-thick anvil as shown in Fig. 9. Three gages, two manganin stress gages and one PVF₂ stress gage, were placed at each of the three interfaces. The flyer plate was 3-mm-thick brass accelerated to 0.900 mm/ μ s. Figure 10 shows representative outputs of an embedded pressure gage, one of which shows the location of the elastic precursor wave from which HELs were determined.



L80-5855-2



Figure 8. a) Schematic diagram of strain-gage assembly showing location of gages mounted on the specimen and b) photo showing the specimens mounted to the target plate.



L894-7153-2

Figure 9. Schematic of gas-gun-driven flyer-plate test to determine material response to peak pressures within the elastic plastic region of the test material.

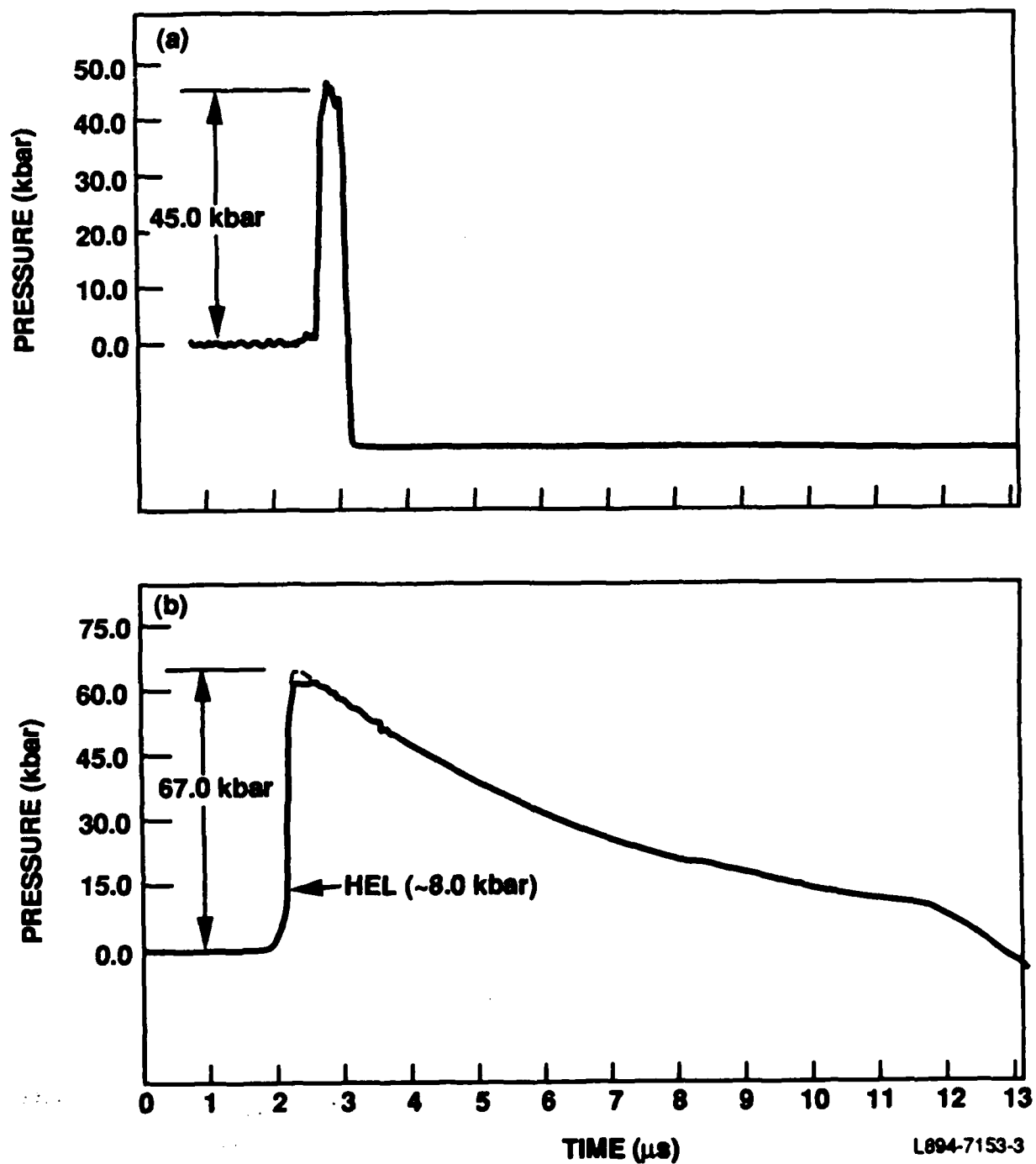


Figure 10. Output upon initial impact of a) manganin gage on cement sample and b) PVF₂ pressure gage on mortar sample at a depth of 5 mm beneath the impact surface.

Wave attenuation resulting from both wave scatter and wave absorption within the porous material was observed in the instrumented tests. Data from each test are presented in Table 3. The HEL values were found to increase as w/c (porosity) decreased, although an average HEL is about 5 kbar. As expected, higher impact velocities generate higher pressures. Although limited, the data do indicate higher HEL's for the same material when tested at higher peak pressures. However, the precise relationships among the HEL, peak pressure, and microstructure are uncertain because of our limited testing.

From the typical signal from one of the manganin and one of the piezoelectric polymer (PVF₂) pressure gages for the Dynasen tests shown in Fig. 10, note that the peak pressure in the sample lasts only a few tenths of a microsecond. The impact pressures and the pressures obtained from gages embedded at 5-mm increments beneath the impacted surface are plotted in Fig. 11 for both the cement and mortar samples. The impacting pressures of 67 kbar for the cement and 50 kbar for the mortar were determined indirectly from the calculated shock impedance, i.e., density and shock velocity, of the sample and the known shock impedance for brass (Fig. 11). (Note that the initial particle velocity is 0.9 mm/μs, which was obtained from the flyer plate velocity.) The peak pressure attenuates at about 1.5 kbar/mm for the cement paste sample and at about 1.4 kbar/mm for the mortar sample.

From the arrival time of the signal at the various gage locations, the shock velocities of the cement paste and mortar were calculated to be 3.6 mm/μs and 3.09 mm/μs, respectively. Because the bulk densities of the mortar (2.1g/cm³) and the cement paste (2.2g/cm³) were essentially the same, differences in shock velocity are felt to reflect of differences in the materials, such as porosity and the presence/absence of quartz fine aggregate (~ 50% of the mortar).

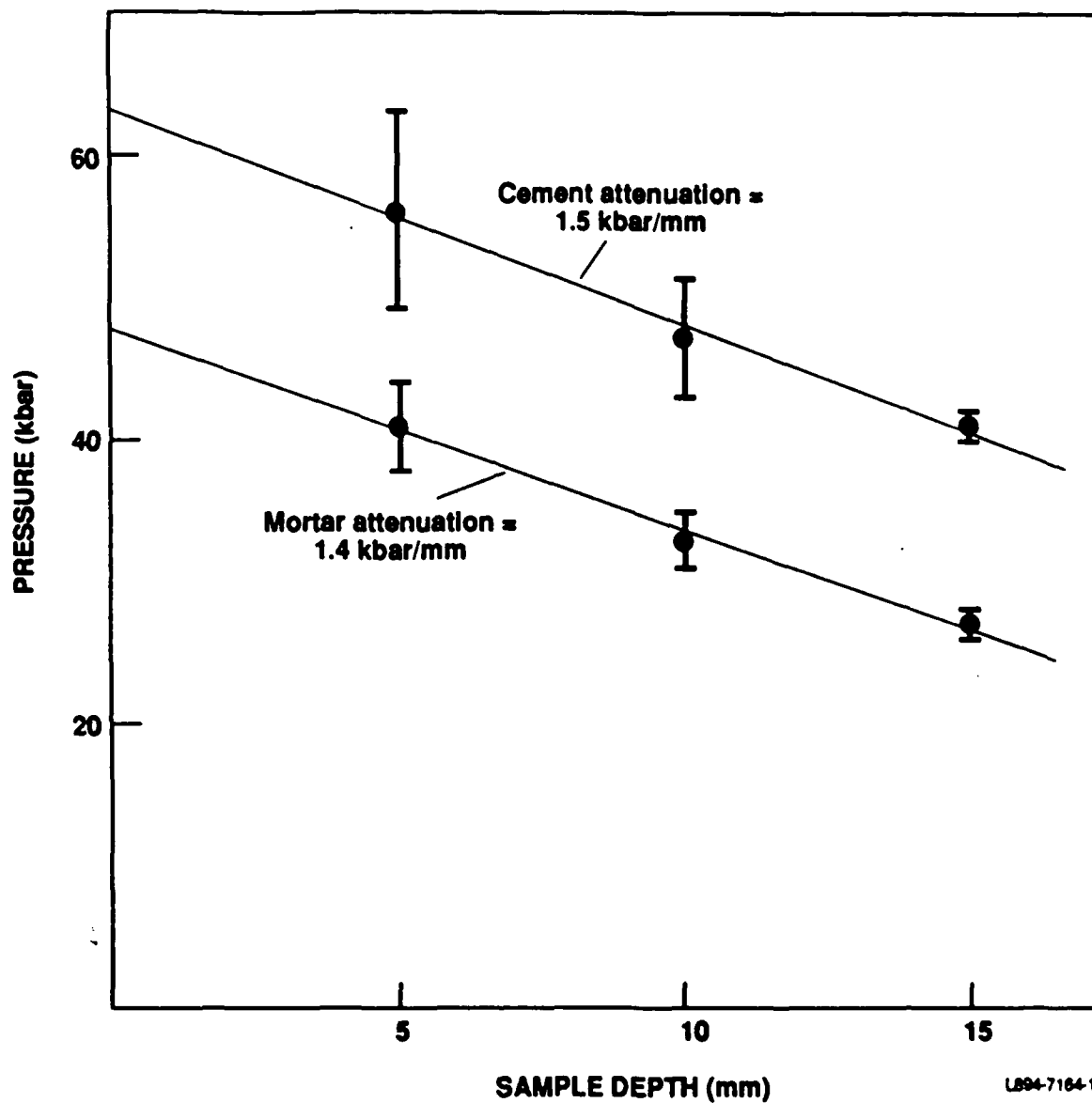


Figure 11. Plot of pressure vs sample depth for cement and mortar samples conducted at Dynasen.

C. SHOCK RECOVERY: EXPERIMENTAL METHODS AND RESULTS

1. Methods

In order to analyze microstructural response of cement pastes shock loaded into the elastic-plastic material response regime, two basic conditions must be met:

- The sample must be recovered for characterization after loading with intense pressures
- The pressures and loading history of the sample must be known to allow correlations with microstructural changes.

As reviewed above, explosive loading techniques allow experiments to be designed that load a test material with an essentially pure uniaxial strain impulse. This requires a) careful construction of the explosive fixture to develop a stable planar shock impulse and b) use of impedance-matched momentum traps that permit the initial loading impulse to pass through the sample unperturbed while preventing reflections of that impulse from reflecting back into the sample. Use of planar impulses and momentum traps allows the initial "simple" loading condition to be the primary one experienced by the sample, i.e., there are no complications by secondary loading, and, most importantly, prevents the sample from being destroyed and thus allows its recovery. In the following section, the construction of the explosive fixture and associated momentum trap is reviewed and the degree to which the required objectives of these tests were met is presented.

The momentum trap is designed to pass compressive waves, but to easily separate on planes of weakness to prevent tensile waves from traveling back across the interfaces to the target. In this manner, the momentum is trapped. Ideally, a momentum trap acts like an infinite half space. Compressive waves pass through the target into the surrounding material with no returning reflections.

Originally, it was assumed that the tests would be conducted at the Atlas Powder Company test facility where the target would be embedded in a fixture buried in the ground. This set-up comes as close as possible to an infinite momentum trap. When the tests were shifted to an indoor facility at Naval Surface Warfare Center (NSWC), a finite-sized momentum trap had to be developed.

The impedance-matching assembly consisted of cement sections cast around the sample, which was first coated with silicon grease to introduce a plane of weakness and also prevent moisture penetration during the casting. The sections were colored (stained with different food colorings) during mixing to help distinguish them from the undyed, shocked cement test specimens during post-test recovery.

Figure 12 is a schematic of the top and cross-sectional views of a sample in the impedance assembly. The sample was sandwiched between a 5-mm-thick cover (buffer) plate above and a 15-mm-thick anvil of the same diameter below. The mating surfaces between the buffer, sample, and anvil were precisely machined to reduce impedance mismatch and thus promote clean loading with minimum reflections. The stack of the buffer, sample, and anvil was first encased by casting a 51-mm-diameter cement cylinder (spall ring) around it to constrain lateral expansion and minimize radial reflected waves. The cylinder was then surrounded by a cast 102- x 102- x 63-mm spall block of cement paste with an additional spall plate directly under the spall ring. Planes of weakness were purposely introduced into the cement block to further trap wave momentum and prevent reflected tensile and shear waves from returning to the sample.

The impedance assembly was placed on top of a momentum trap consisting of tightly stacked concrete bricks. As the initial compressive loading pulse reflects in the bricks, they fly apart, so that the reflected impulses are trapped and prevented from returning to the sample trap. The entire fixture was placed upon sand bags to further isolate the momentum trap from the solid floor [Fig. 13 (a)].

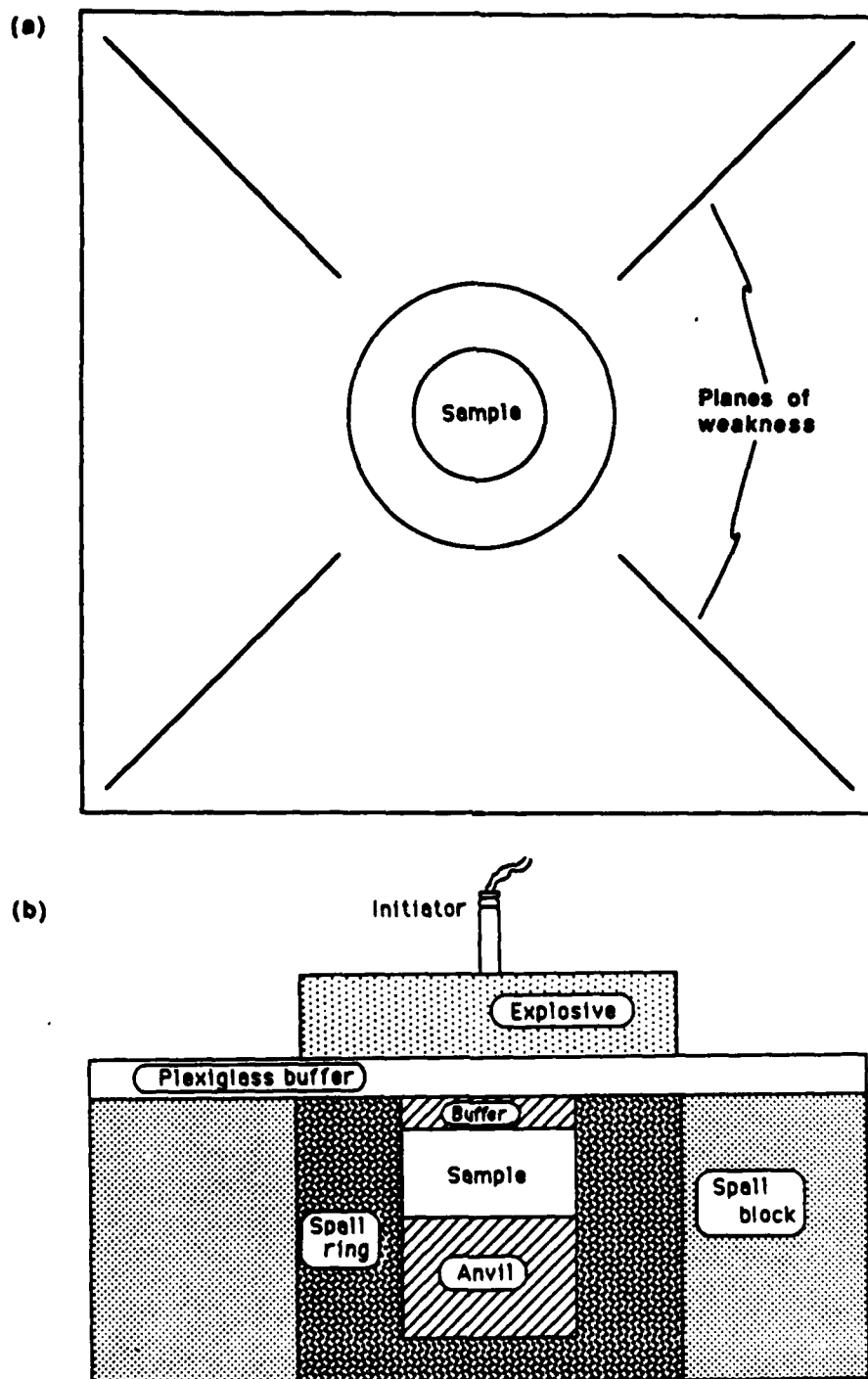
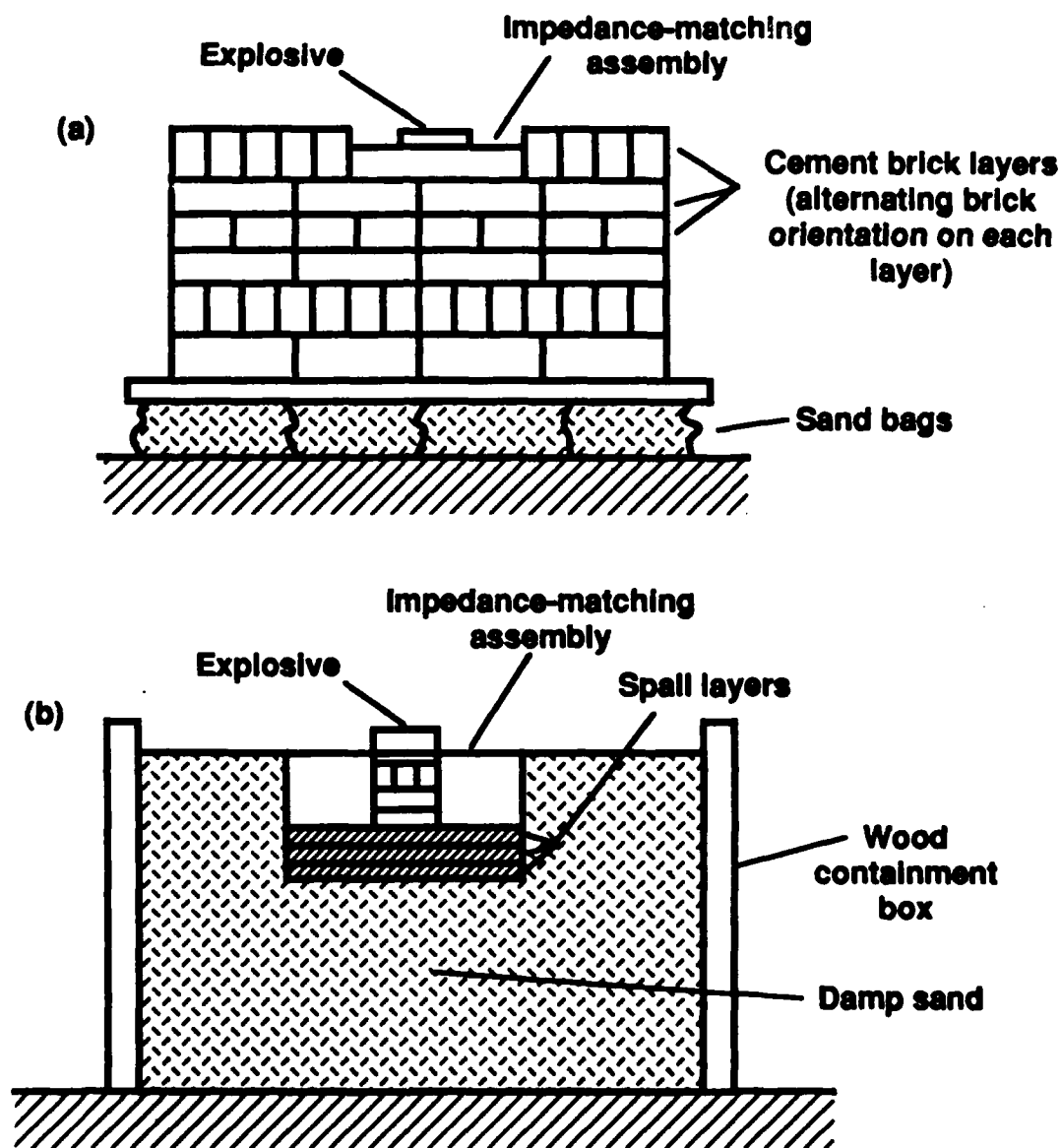


Figure 12. Schematic of the a) top and b) cross-sectional views of a sample in the impedance assembly.



L894-7153-1

Figure 13. Schematic of a) the first momentum trap design including the impedance assembly and b) the larger momentum trap design including the impedance assembly with the spall layers.

This momentum trap design proved to be inadequate for recovery with the quantity of explosive necessary to guarantee good plane-wave loading. Thus, improved momentum traps were constructed using damp sand as the momentum trap material. The target sample was again mounted in an impedance matching assembly which was increased in size to 40 x 40 x 17 cm (16 x 16 x 6.75 inches). The target sample was kept at 25 mm in diameter, but its thickness was increased to 25 mm. The other major changes besides the increases in size were the inclusion of 3 spall layers and another anvil layer beneath the target sample to minimize unwanted tensile reflections. This impedance-matching assembly was then placed in a box 81- x 81- x 61-cm deep (32 x 32 x 24 inches). Over one-half ton of damp sand was then tightly packed around it as shown in Fig. 13 (b).

Cylindrical blocks of explosive used to generate the shock impulse were placed directly on the impedance-matching cover plate or upon an intermediate buffer plate of polycarbonate. Edge effects from the explosive were minimized by making the diameter of the explosive larger than that of the sample. The duration of the compressive loading pulse was controlled by varying the thickness of the explosive: both 12.7 mm (0.5 inch) and 25.4 mm (1 inch) thicknesses were used. The magnitude of the peak pressure is a function of the detonation pressure and velocity of the explosive. DuPont Deta-Sheet (a PETN-based "plastic" explosive) was used for all tests because of its commercial availability and the ease in which it allows preparation of a cylindrical block of explosive. Deta-Sheet was also chosen since it should give an intermediate pressure, compared to other typical explosives such as TNT or Comp B (a general purpose, high-velocity, military explosive).

The explosive block was initiated two different ways. In the original experimental plan, an explosive plane-wave lens was to be used to initiate the block of explosive uniformly across the entire top surface. The plane wave initiation was needed to ensure planar shock (uniaxial strain) in the sample. The plane-wave lenses that were available from NSWC contained over 1.5 times more explosive than the block of Deta-Sheet used to load the sample. This combination of plane-wave lens and Deta-Sheet block proved to be

too energetic for our original momentum-trap design and were only used successfully for the last few tests with the very large sand momentum traps.

However, successful recovery tests were made with the original momentum trap design by initiating the block of Deta-Sheet with a normal detonator, i.e., blasting cap. The detonator was placed on the center of the top surface of the explosive block, resulting in a point initiation with a spherical detonation front. (In fact, because of the detonator design and size and the relatively small size of the explosive block, the conditions of initiation were more complex than that of a point-source initiation.) By the time the detonation front reached the sample assembly, its curvature was relatively small and thus more closely approximated a planar front. Further, a 12-mm-thick polycarbonate buffer plate, placed between the explosive and the cement sample assembly to aid in smoothing the wave front and increasing its radius of curvature, did not markedly attenuate the pressure pulse.

2. Results and Discussion

A total of 18 recovery tests were conducted on cement and mortar samples (Type III paste, 0.25 w/c) with varying degrees of success (Table 4). The first 15 tests were conducted with the smaller, brick momentum-trap design and point initiation on the explosive source (except the first two). The purpose of these tests was to perfect a momentum-trap design and then measure the peak pressures induced in the test samples. Tests C1 through C5 were noninstrumented recovery tests designed to examine the physics of the recovery set-up without the additional complexity of instrumentation. In our initial experiments (C1 and C2), an explosive plane-wave lens was used to initiate the explosive driver. The lens proved to be too energetic for our momentum trap fixture. After two additional tests (C3 and C4) using point-initiated contact explosives, we determined that altering the design of the momentum traps to include the polycarbonate buffer plate greatly improved sample recovery. Accordingly, although small fragments were recovered in test C4, approximately one third to one half of the sample was recovered for tests C5 through C7. It was recognized that the loading was not truly planar, and

TABLE 4
CEMENT TESTS

Test #	Explosive Used	Gage Depth (mm)		Peak Pressure (kbar)		Comments
		#1	#2	#1	#2	
C1	0.5					No recovery
C2	1 x 2					No recovery
C3	PW					No recovery
C4	1 x 2					Small fragments recovered
C5	1 x 2, PC	5	20			Specimen intact
C6	1 x 2, PC	5	20			Specimen intact, clipped signal
C7	1 x 2, PC	5	20			Good fragments, no trigger
C8	1 x 2, PC	5	20			No recovery, no trigger
C9	1 x 2, PC	5	20	80	60	No recovery, cross talk
C10	1 x 2, PC	5	20	70	40	No recovery, cross talk
C11	1 x 3, PW lens					Specimen intact
C12	1 x 3, PW lens					Specimen intact
M1	0.5 x 3 0.5 PC	5	20	50	30	No recovery, cross talk
M2	1 x 3, 0.5 PC	5	20	25	...	No recovery, cross talk
M3	0.5 x 3, 0.5 PC	15		40		Mica-armored gage, no recovery
M4	0.5 x 3, 0.5 PC	5	20	25	...	Mica-armored gage, no recovery, cross talk
M5	1 x 3, PW lens					No recovery, anvil only
M6	1 x 3, PW lens					No recovery, anvil only

* Explosive Deta-Sheet explosive size: thickness x diameter in inches; PW, plane-wave lens, otherwise center detonated; PC, thickness of polycarbonate buffer plate if used, in inches.

therefore not without large pressure gradients, but it was assumed that the loading could not be too bad as reflected by the large sizes of the recovered samples.

Problems arose when attempts were made to measure peak pressures within this shot design (tests C6 to C8). The manganin stress gages appeared to fail shortly after the arrival of the shock wave. It was questionable whether the gages were able to survive long enough to measure the peak values while embedded within the momentum trap. Pressure data were recorded for test C6, but a clipped signal prevented peak pressures from actually being measured: a gage record of outputs for this test is shown in Fig. 14. Although the output of the top gage, i.e., the one closest to the explosive, was clipped, peak pressures were estimated to be about 60-80 kbar with a pulse duration of approximately 1 μ s. Travel time of the shock pulse through the cement sample indicated a shock velocity of about 3,100 m/s. The small amplitude of the signal from the bottom gage showed considerable attenuation of the shock wave. Although some attenuation is expected (i.e., 1.5 kbar/mm), the excessive reduction of signal also suggests problems with this gage. No pressure data were obtained for tests C7 and C8.

Pressure data were obtained in tests C9, C10, M1, and M2 by mounting the gages between the buffer and the top of the sample surface and between the bottom of the sample and the top surface of the anvil, i.e., as in prior tests. However, the impedance and momentum trap fixtures were not attached. Testing in this fashion precluded sample recovery, but increased the chances of gage survival during the passage of the shock front.

During testing, another problem associated with the gage power supply became noticeable, i.e., cross talk between the two channels. The power supply is actually a two-channel combination of dynamic bridge amplifier and power supply designed and built by Dynasen just for the piezoresistive manganin gages. The problem of the signal from one gage showing up on the channel of the other gage on the power supply occurred only under actual dynamic testing and could not be simulated on the test bench. Only after all

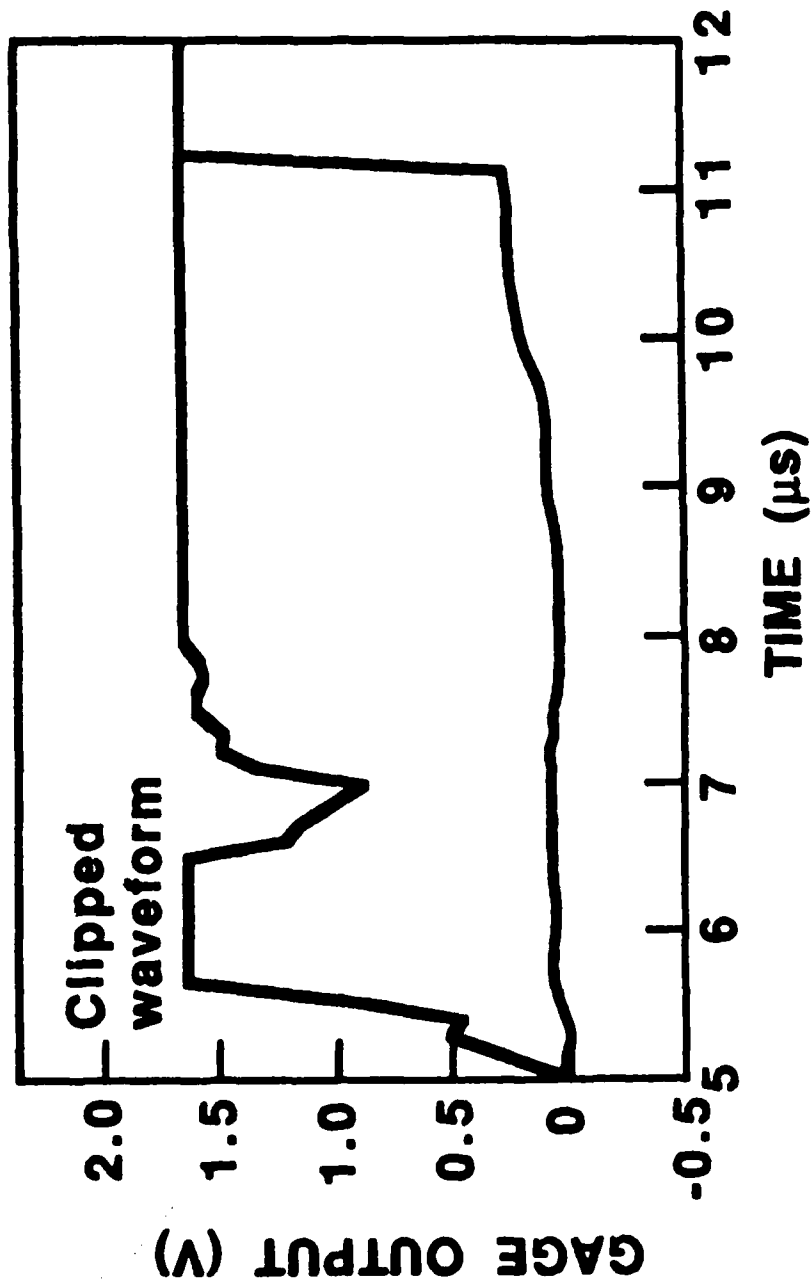


Figure 14. Shock pressure data from test C6. Top waveform: gage output (pressure) recorded between the buffer and the sample; bottom waveform: indicates pressure recorded between the sample and the anvil.

the instrumented tests were completed and the power supply shipped back to Dynasen was it discovered that there was a bad transformer and ground plane in the instrument. Thus, the shock speed measurements, which require arrival of a signal at two independent gages a known distance apart, are questionable. The peak pressure measurements are assumed to be good only to about ± 10 kbar because of the instrumentation problems and the divergent nature of the shock wave and edge effects when the explosive charges were not detonated with the plane-wave lens.

Even with these difficulties, the peak pressure for the cement paste under explosive loading with center detonation was determined to be about 60-80 kbar with a shock velocity of about 4 mm/ μ s. This peak pressure value closely agrees with a simulation of the test geometry conducted with EPIC-2 (a dynamic finite-element hydro code). Although the shock velocity is slightly faster than the velocity of 3.6 mm/ μ s determined in the gas-gun test (most likely due to differences in peak pressure), the 1.7 kbar/mm attenuation measured with explosive loading compares with the 1.5 kbar/mm attenuation from the gas gun test.

Because gradients in the nonplanar wave front were also suspected of contributing to the poor signals from the manganin gages, a military plane-wave lens was used to initiate a larger explosive driver in the last series of explosive loading tests. The increased diameter of the explosive and the plane-wave initiation scheme were used to minimize edge effects from the explosive (rarefaction waves propagating inward from the edges) and produce a plane-wave loading of the sample. With this more perfect plane-wave loading, the shock pressures within the samples were estimated to be on the order of 100 kbar. As reviewed previously, use of the more energetic explosive charges required a slightly modified, larger momentum trap. With this improvement, samples of cement were recovered, and although mortar samples were not, sections of the mortar impedance-matching fixture were obtained for analysis.

Table 4 contains a summary of the recovery tests noting sample material, explosive and detonation method, whether it was a recovery shot and if instrumented, measured peak pressure at the first and possibly second gage location, and estimated shock speed (if two pressure measurements were possible). Due to the problems with the instrumentation, the pressure measurements and shock velocities should only be considered approximate values.

D. MICROSTRUCTURAL CHARACTERIZATION OF RECOVERED SAMPLES

It has been hypothesized that shock loading causes changes in cement and mortar microstructures, including, to varying degrees, reduction of particle size, phase transformation, twinning, dehydration, phase decomposition, and, at sufficiently high pressures, melting. Consequently, the microstructures of samples of shock-loaded cement paste and mortar were characterized using thermal gravimetric analysis (TGA), XRD, SEM, and mercury intrusion porosimetry.

The approach taken to determine microstructural response was fundamental to isolating the shock effects in hydrated cement paste, and is based on comparative analyses using as a reference materials having virtually identical histories, except for the shock loading event. Thus, we could concentrate only on those features that were different, rather than on every aspect of the microstructure.

1. Sampling Procedure

Large sample fragments were recovered from tests C5 through C7 and from tests C11 and C12 (Fig. 15) and were stored in a dessicator until they could be characterized. For TGA, ~ 10 mg of sample was required per run; XRD required at least 0.30 g of sample, which had to be ground into powder to obtain a good diffraction pattern; porosimetry used at least 1.5 g of sample per analysis to obtain meaningful results; and SEM required at least 0.1 g of sample per analyses.

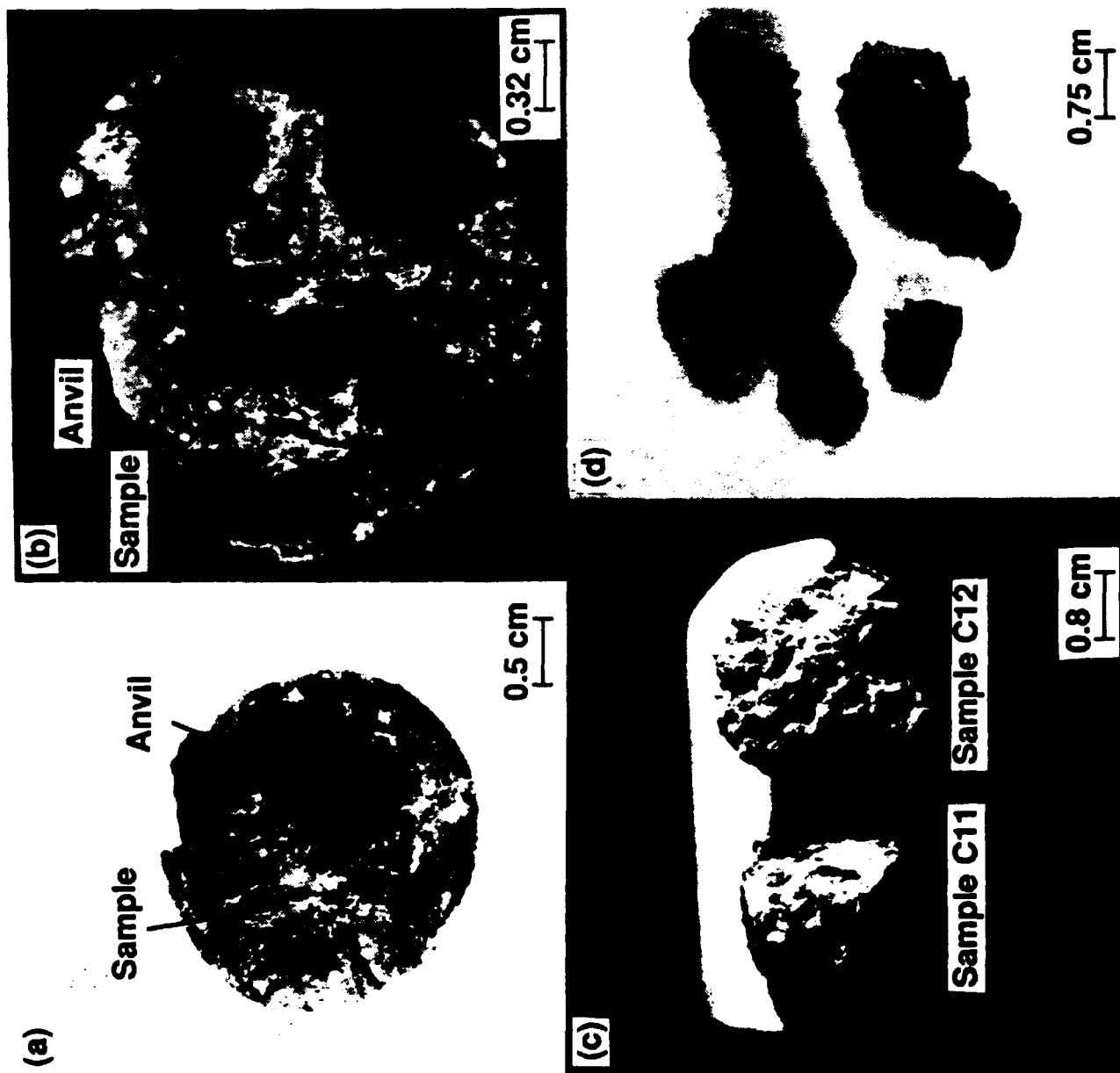


Figure 15. Recovered test samples from tests C5 through C7 and from C11 and C12. Intact samples were recovered from tests a) C6, b) C5, c) C11 and C12; sample fragments were recovered from d) C7.

The samples recovered from tests C5 through C7 clearly indicate a non-uniform loading pulse, as only sections and fragments were recovered (as seen in Fig. 15). In contrast, the loading geometry of tests C11 and C12 appeared to be more uniform. In the latter two tests, the entire diameter of the sample was recovered, but only the bottom third of the sample was intact. These samples were significantly cracked, especially on the top surfaces, with many shear-type failures seen upon visual examination. Samples were not recovered from the mortar tests (M5 and M6). However, the material directly beneath the sample (the anvil of the impedance fixture) was recovered intact and used to characterize the mortar microstructure.

2. TGA Analyses

The phenomena of dewatering and phase decomposition within the shock-loaded cement and mortar samples were examined using TGA. The samples were heated from room temperature to 1000°C at a rate of 10°C/min and the weight change was recorded (Fig. 16). There were no significant differences between referenced and shocked samples. The initial decrease in slope is consistent with the evaporation of water near 100°C. The discontinuity observed around 400°C indicates the decomposition of hydroxyl groups within the samples. The consistencies of the untested and tested samples indicate that either a) the conditions for dewatering and hydroxide decomposition were not reached in the samples subjected to high strain-rate loading or b) such effects occurred, but were short-lived as the sample re-equilibrated, i.e., immediately after passage of the shock wave or between the time of the test and the analysis.

3. XRD Analyses

Analyzing the shock response of single-phase materials is difficult in itself. Analysis of a complex multiphase material such as cement paste, where the predominant phases are largely amorphous, is even more so. However, our comparative analytical approach was successful in isolating several specific shock-induced responses noted through the use of powder XRD techniques.

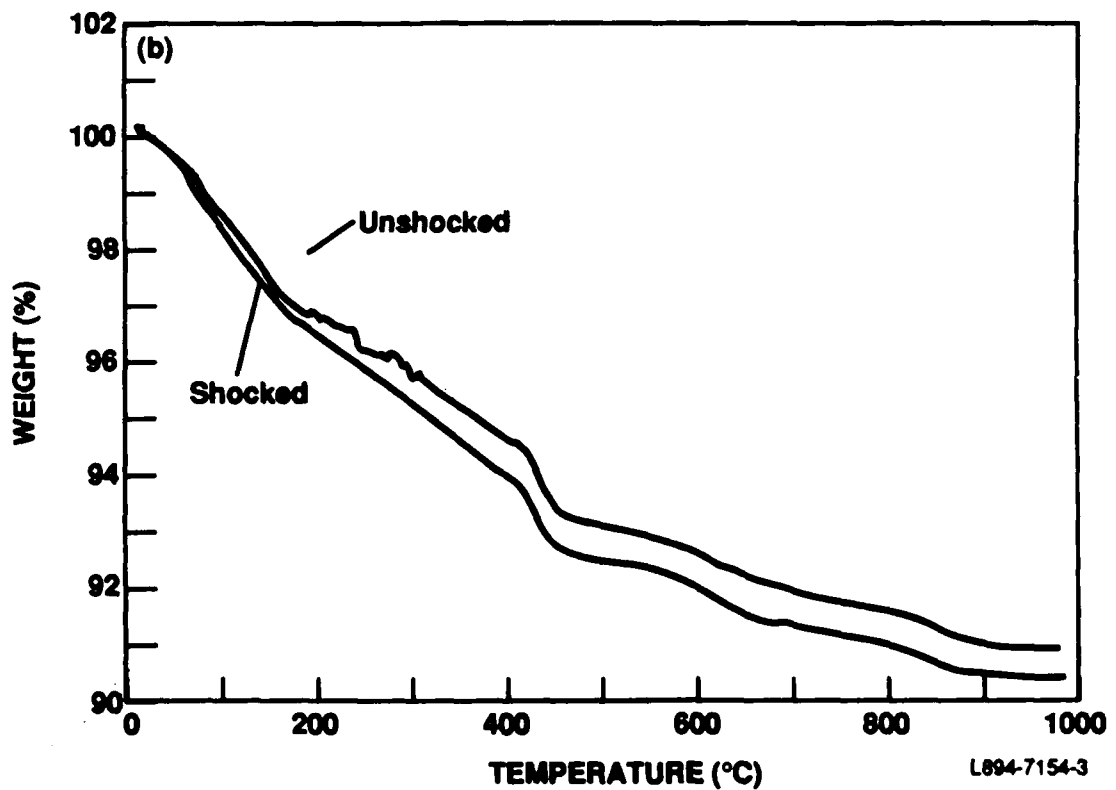
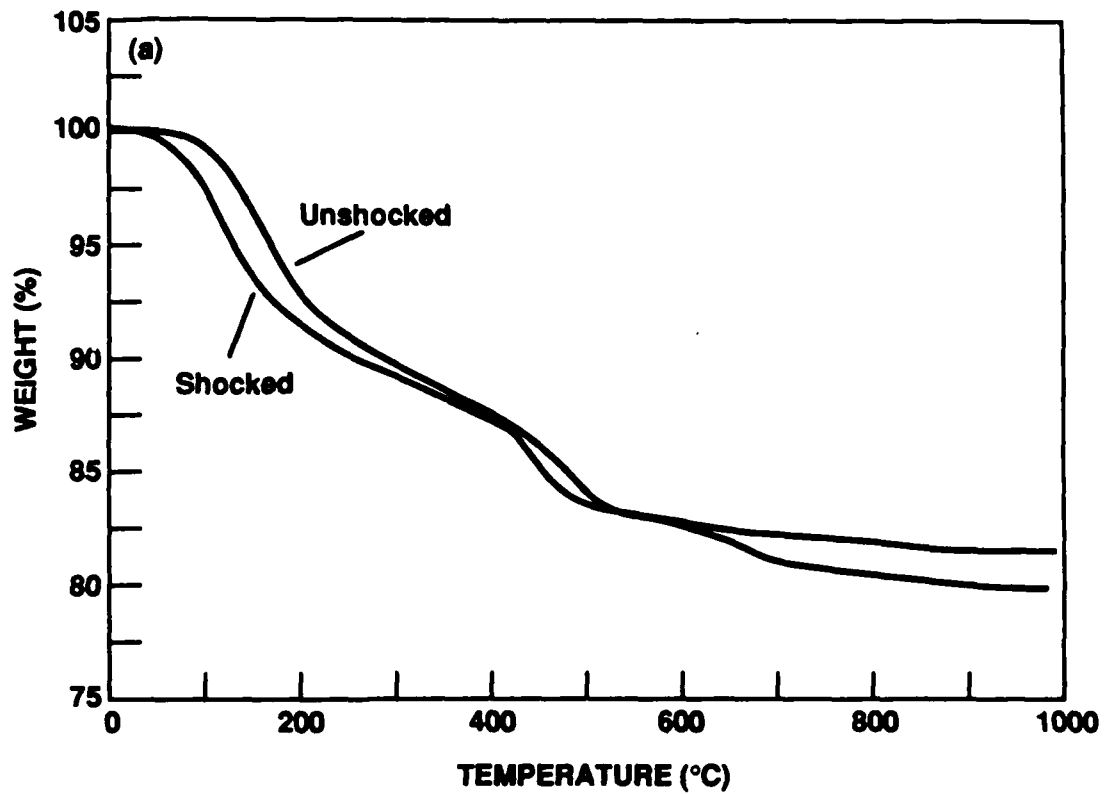


Figure 16. TGA plots of unshocked and shocked a) cement and b) mortar samples ramped to 1000°C at a heating rate of 10°C/min.

Observations were made on XRD patterns covering 2-theta angles between 15 - 20 degrees, where major peaks for C-S-H and C-H are located, and between 27 - 40 degrees, where major peaks from C-H and alite are located (Fig. 17). The patterns were made using a Philips Model XRG-3000 diffractometer integrated with a computer system for peak identification and characterization and at scanning rates of 0.01 degrees/s to improve resolution. The cement (and mortar) specimens were ground in a carbide mortar and pestle and immediately scanned to minimize detrimental reactions with the atmosphere.

The basic points of our analyses are:

- XRD patterns are reproducible for reference pastes of Type III cement (0.25 w/c) aged between 60 - 90 days
- Shocked pastes show peak broadening of the predominant crystalline hydrated phase (C-H), but broadening is not observed for an unhydrated cement mineral (alite)
- The ratio of the (205) alite and adjacent (101) C-H peak heights always increases after shock loading
- Shifts of C-H and alite peaks to high 2-theta values (smaller d-spacings) are generally observed in some of the shock-loaded samples, i.e., those from more recent shock tests
- The intensities of broad semicrystalline C-S-H peaks are reduced in shocked pastes.

Table 5 (A and B) is a compilation of the characteristics for the principal peaks used in our analyses. As seen in the table, the peak locations and widths measured for all reference (unshocked) materials are reproducible. However, there are some minor differences in peak amplitudes

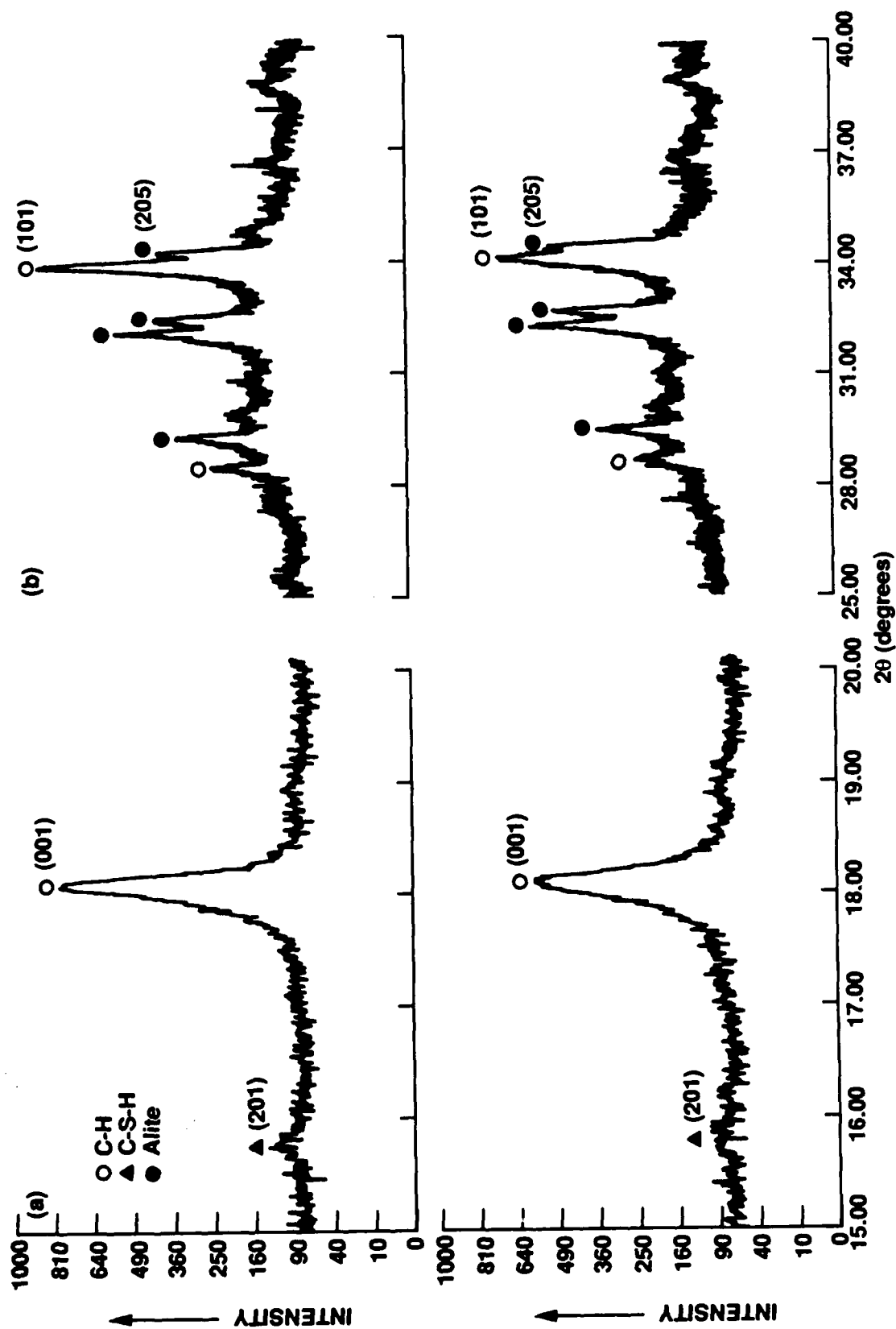


Figure 17. Typical XRD scan of a) unshocked and b) shocked cement between 15-40 degrees.

TABLE 5

PART A

REFERENCE DATA

<u>Sample</u>	<u>Peak</u>	<u>Lattice plane (hkl)</u>	<u>2θ (degrees)</u>	<u>Width (degrees)</u>	<u>Intensity, (counts/s) alite (205)/ C-H (101)</u>
942	C-S-H	201	-	-	0.55
	C-H	001	17.96	0.17	
	C-H	101	34.00	0.19	
	Alite	205	34.38	0.14	
569	C-S-H	201	15.74	0.17	0.39
	C-H	001	17.96	0.14	
	C-H	101	34.03	0.20	
	Alite	205	34.35	0.14	
993	C-S-H	201	15.75	-	0.54
	C-H	001	17.98	0.13	
	C-H	101	34.02	0.19	
	Alite	205	34.34	0.15	
1296	C-S-H	201	15.78	0.13	0.53
	C-H	001	18.02	0.16	
	C-H	101	34.06	0.15	
	Alite	205	34.39	0.09	
1015	C-S-H	201	-	-	0.48
	C-H	001	-	-	
	C-H	101	34.03	0.18	
	Alite	205	34.34	0.10	

AVERAGE REFERENCE DATA

		<u>2θ</u>	<u>Width</u>
C-S-H	201	15.76 \pm 0.02	0.15 \pm N/A
C-H	001	17.98 \pm 0.03	0.15 \pm 0.02
C-H	101	34.03 \pm 0.02	0.18 \pm 0.02
Alite	205	34.36 \pm 0.02	0.12 \pm 0.03

TABLE 5

PART B

SHOCKED SAMPLE DATA

Sample	Peak	Lattice plane (hkl)	2 θ (degrees)	Width (degrees)	Intensity, (counts/s) alite (205)/ C-H (101)
943	C-S-H	201	-	-	0.71
	C-H	001	17.96 ¹	0.20 ¹	
	C-H	101	33.99 ¹	0.27 ¹	
	Alite	205	34.36	0.15	
992	C-S-H	201	-	-	0.93
	C-H	001	17.98 ¹	0.19 ¹	
	C-H	101	34.04 ¹	0.25 ¹	
	Alite	205	34.39 ¹	0.11	
1297	C-S-H	201	15.81 ¹	0.13	0.70
	C-H	001	18.02 ¹	0.15	
	C-H	101	34.08 ¹	0.25 ¹	
	Alite	205	34.46 ¹	0.12	
570	C-S-H	201	15.80 ¹	0.11	0.65
	C-H	001	18.16 ¹	0.22 ¹	
	C-H	101	34.18 ¹	0.20	
	Alite	205	34.56 ¹	0.15	
1165	C-S-H	201	-	-	0.73
	C-H	001	-	-	
	C-H	101	34.43 ¹	0.24 ¹	
	Alite	205	34.78 ¹	0.14	
1164	C-S-H	201	-	-	0.60
	C-H	001	-	-	
	C-H	101	34.05 ¹	0.24 ¹	
	Alite	205	34.50 ¹	0.14	
1163	C-S-H	201	-	-	0.62
	C-H	001	-	-	
	C-H	101	34.14 ¹	0.22 ¹	
	Alite	205	34.50 ¹	0.13	

¹ Value outside first standard deviation of reference data.

and ratios between peaks. First, increased peak heights of the 201 C-S-H peak are seen in both of the reference pastes that had longer cure times, i.e., 90 days, relative to the 60-day cure times for the younger pastes (Fig. 18). The increase is believed to correlate with increasing crystalline character of the amorphous C-S-H hydration product as the pastes matured. The second difference noted in the reference pastes was a general reduction in the ratio of the unhydrated cement mineral, alite, to that of the dominant crystalline phase, C-H. This difference is also related to the maturity of the cement paste. Such results are consistent with continued hydration of the paste with time, as expected.

Peak locations and widths of reference specimens were averaged and compared with similar values from the shocked cement pastes (Table 5B). Those values that were outside the scatter of mean values for the reference material have been highlighted. Peak broadening is generally observed for C-H in all tests, but not for the alite. Broadening of the crystalline peak is generally interpreted as either a) reduction in particle size (comminution) or b) residual lattice strain. The contributions from those two factors are not easily separated and no distinction is made here. Similarly, ratios of peak intensities for the (205) alite peak and the (101) C-H increase in all shocked cement samples, relative to the reference paste. Such behavior is consistent with peak broadening of the C-H peak, because, assuming relatively constant peak areas, heights must change as peaks broaden.

Shifts in the locations of peaks were noted for both C-H and alite in the shocked samples from tests C6, C11, and C12. Peak shifts to smaller d-spacing, as a result of compaction of the crystal lattice in response to the shock loading, are certainly possible. It is not apparent whether the observed shifts are related to the type of shock loading, i.e., planar or curved shock front and/or the magnitude of the loading pulse.

Shock loading was also observed to reduce the intensity of the (201) C-S-H "peak" noted in some of the cement samples (Fig. 18). We hypothesize that this effect is a shock-induced "disordering" of the partially crystalline

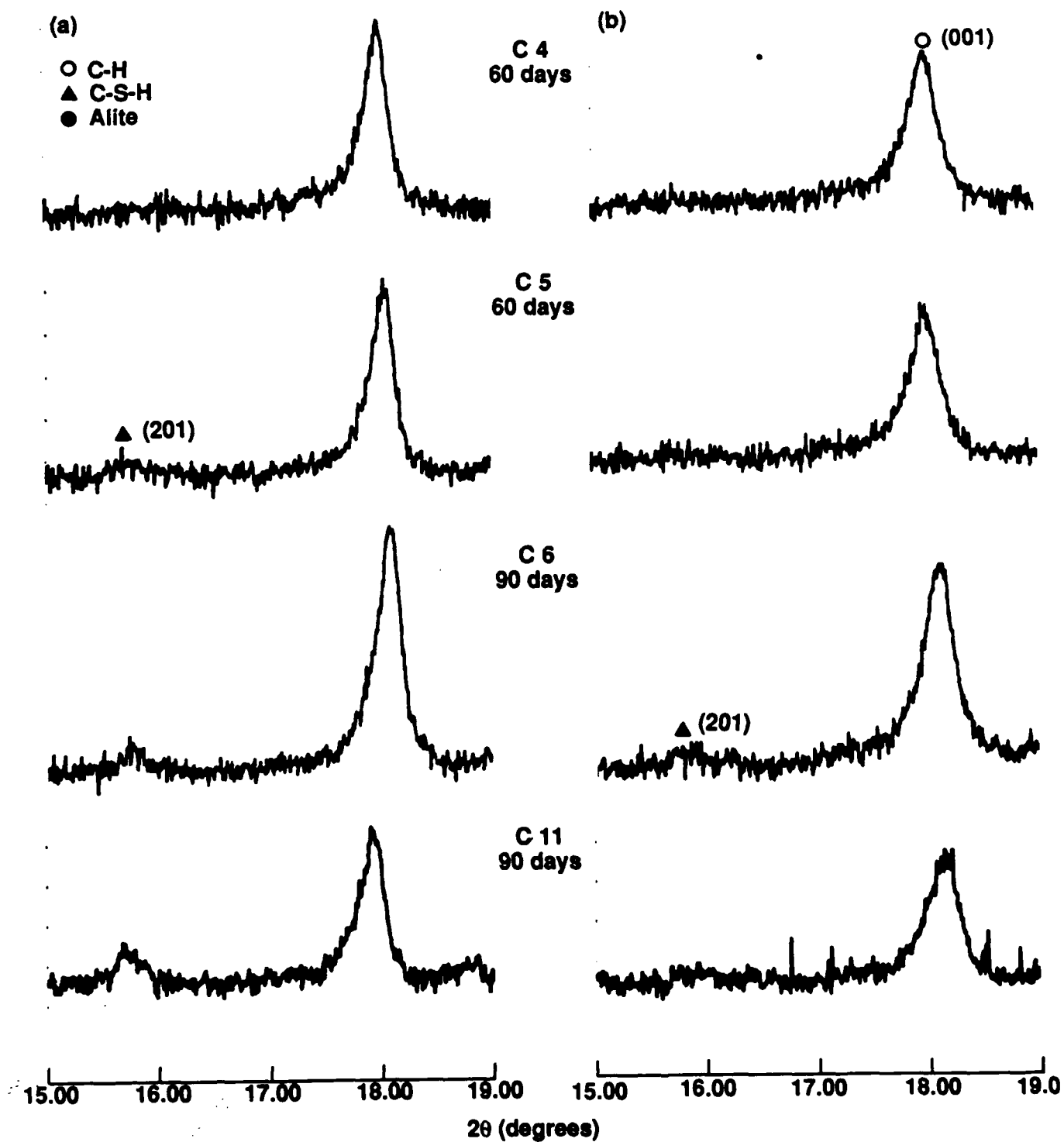


Figure 18. XRD scans of a) unshocked and b) shocked cement paste at various times from initial casting.

C-S-H lattice. However, additional characterizations are needed to confirm this hypothesis.

4. SEM Analysis

Direct SEM observation of the microstructure of recovered shock-loaded samples shows changes in porosity and cement mineral morphology. In our investigations, no attempt was made to identify specific minerals or changes in microchemistry because of the very complex and fine grained nature of the materials. [In general, crystalline minerals with platy cleavage were assumed to be C-H, needle-like minerals were classed as "ettringite-type phases," and all other more massively-structured areas were classified as C-S-H products.] As reviewed below, the principal goal of the SEM analyses was identification not of individual features, but rather of types of features that occurred only in shocked samples through the use of comparative analyses of reference specimens.

Fracture surfaces of cement specimens were observed at magnifications ranging from 1,000 to 100,000 times. Typically, 2 hours of observation time were spent per individual specimen, i.e., a fragment of material from a selected area of the recovered test sample. Areas for observation were selected by randomly moving the test specimen in the scanning electron microscope followed by detailed examination of that part of the sample that was seen under the "cross-hairs." Numerous photographs (about 10) were taken of each specimen, at various magnifications, to allow easier comparison of different samples. The documentary photographs were taken of portions of the sample that typified the local region being observed; unusual, one-of-a-kind features were specifically avoided.

Significant amounts of shock-loaded cement (and mortar) were recovered from six of the recovery tests performed. To preserve differences in material response that might have occurred due to variations in the loading experiments, we examined test specimens in groups related to testing conditions, i.e., cement pastes were tested with either a) point-initiated or b) plane-

wave-initiated contact explosives, or c) plane-wave-initiated contact explosives on mortar. Although variations in the amount of material response were documented (both from sample to sample and also within the same sample), three dominant responses were observed:

- Changes/elimination of certain types of porosity
- Modification, i.e., granulation, of C-S-H
- Microcracking.

a. Point-initiated Explosive Shock in Cement Paste: Tests C5 and C6.

Micrographs of fracture surfaces (Fig. 19) of unshocked reference specimens from castings for recovery tests C5 and C6 are typical and exhibit essentially similar microstructures, i.e.,:

- Angular C-H crystals with an average size of 5-10 μm
- Intergrowths of areas of relatively structureless C-S-H
- A network of fine porosity with an average size of 0.1-0.2 μm , defined primarily by C-S-H and needle-like (ettringite?) hydration products.

Micrographs of the predominant features of shocked cement from C6 [Fig. 20 (a) and (c)] and C5 [Fig. 20 (b) and (d)] show microstructures significantly altered from those observed in unshocked pastes. The amount (and size) of angular minerals (C-H and ettringite) in shocked fracture surfaces is less than that of the reference material. Most of the cement matrix is made up of fine-grained submicron (0.1-0.3 μm) particles that are typically rounded to varying degrees (Fig. 21). As seen in Fig. 21, the amount of 0.1 - 0.2 μm porosity seen in the reference materials is significantly reduced in the shocked pastes.

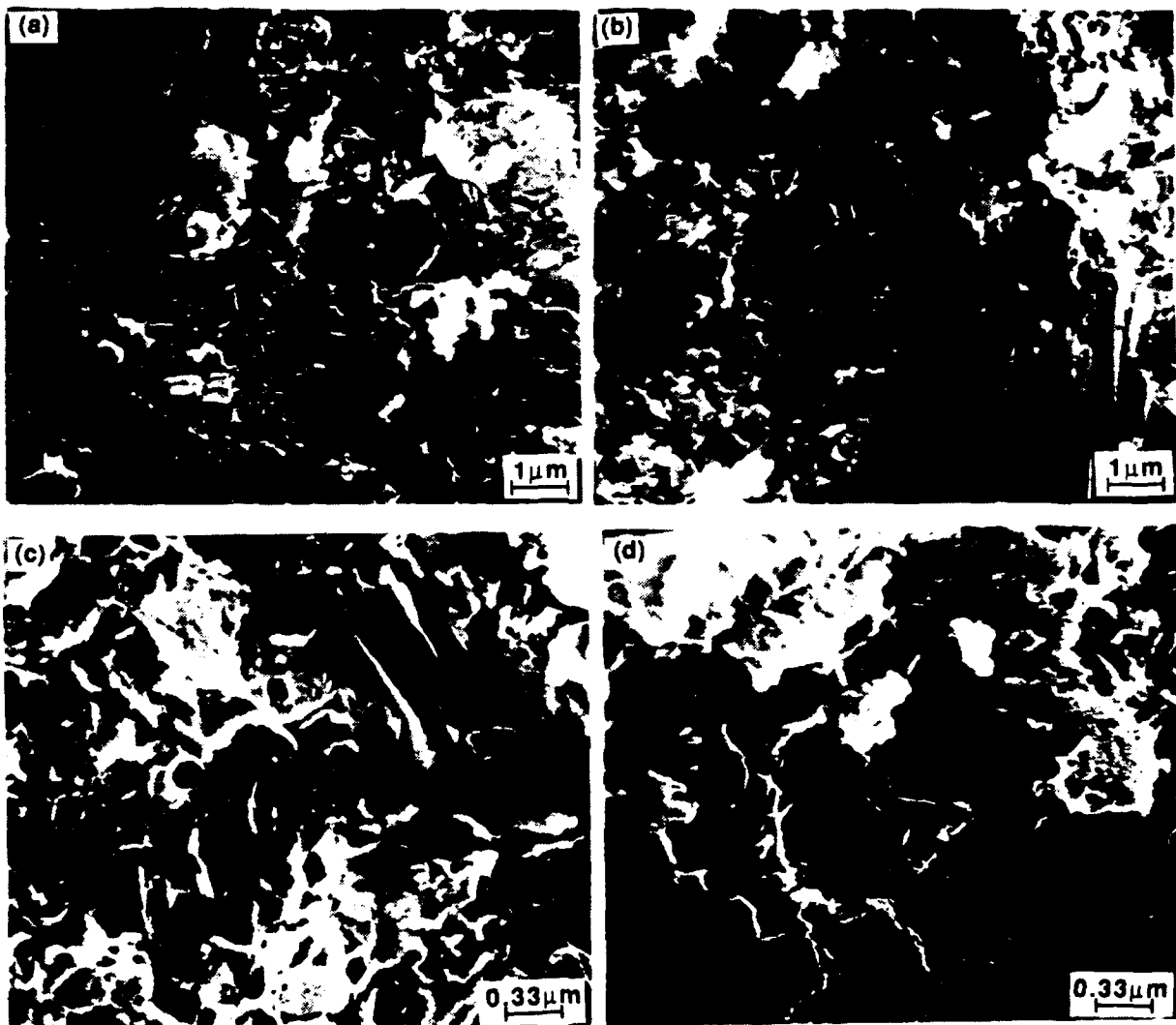


Figure 19. Scanning electron micrographs of unshocked cement fragments showing typical microstructure: (a and c) and (b and d) are the references for shock recovery tests C6 and C5, respectively.

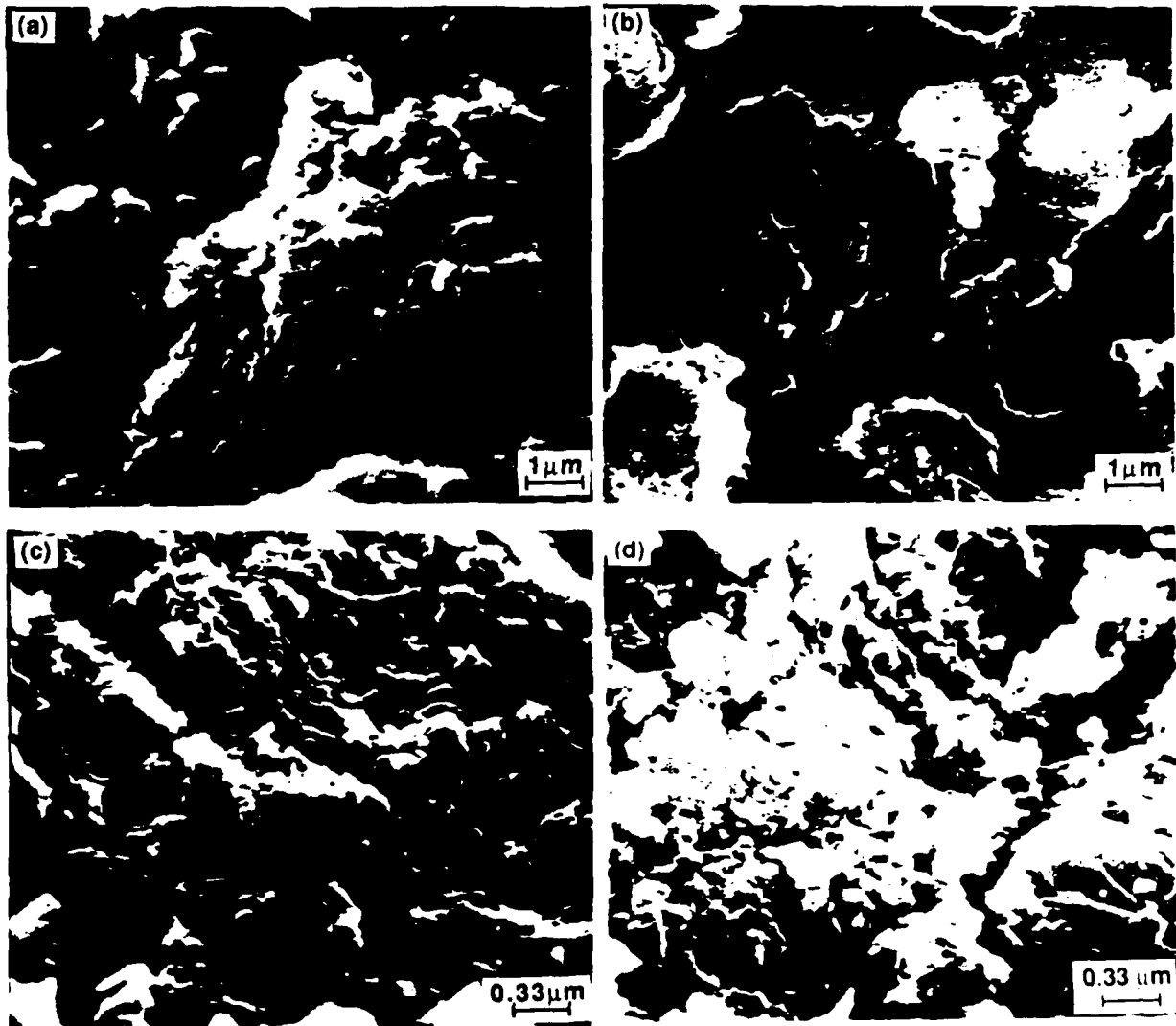


Figure 20. Scanning electron micrographs of fracture surfaces of shocked cement fragments showing compaction and granulation in response to shock recovery tests C6 (a and c) and C5 (b and d).

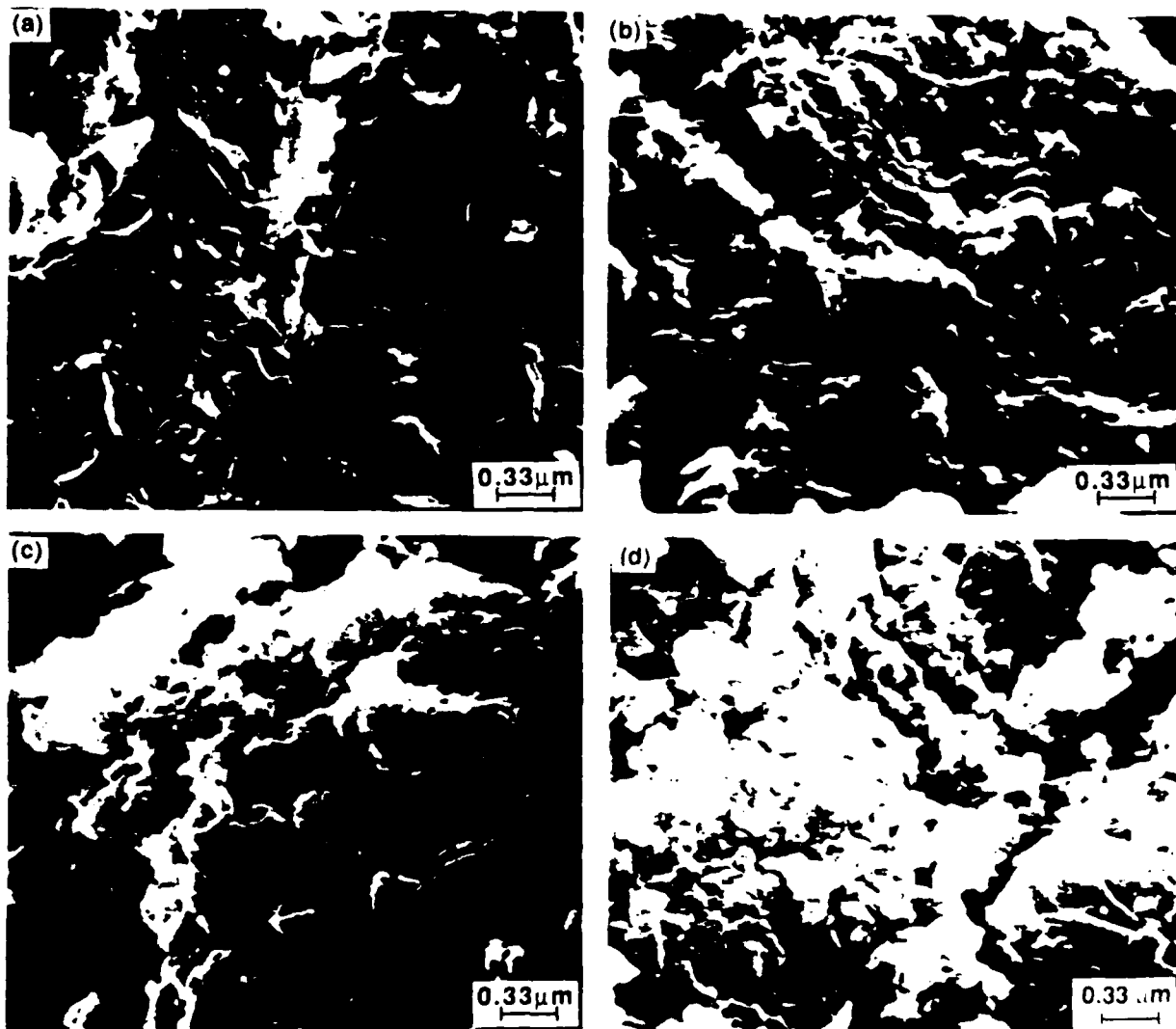


Figure 21. Scanning electron micrographs of cement microstructure showing a) angular porosity in an unshocked reference sample and (b-d) granulation and elimination of angular particles and porosity in shocked specimens.

b. Plane-Wave-Initiated Explosive Shock in Cement Paste: Tests C11 and C12.

These two tests were very successful in that they allowed recovery of the largest amount of intact sample (although portions of the upper half were destroyed in each test). The large samples, with known orientation, made more detailed analyses possible, specifically allowing sampling of the recovered specimens at discrete locations, e.g., top, bottom, and middle. There was significant variation in the amount of alteration of the cement microstructure relative to that of unshocked paste.

The samples for tests C11 and C12 were obtained from the same casting of cement. A reference sample of that casting, removed from an unused shock test fixture, was fractured in a hydraulic press, i.e., low strain-rate loading, and examined by SEM for typical features. Relatively low-magnification observation [Fig. 22 (a)] showed nonhomogeneous microstructure, with widely varying particle sizes, microcracks, and voids that range in size from submicron to 10 μm . Macroscopic voids (up to mm's across) were noted in optical analyses, but were not typical features in the small SEM specimens. Higher magnification [Fig. 22 (b-d)] allowed better observation of individual features in the microstructure. Angular (crystalline C-H) hydration products were prevalent in most fracture surfaces, as were areas of amorphous C-S-H. Much of the discrete porosity seen at high magnification occurs in the C-S-H regions, although the total amount of porosity seen is markedly less than that noted in the earlier reference cement (tests C5 and C6) and in the mortar (following section).

Specimens for SEM were obtained from different locations within the recovered samples, as discussed above. Test C11 specimens were removed from the top edge, top center, and half-way between the two. Of those three sets, the features from the outer edge were most like the reference material, as seen in a comparison of Fig. 22 (reference) and Fig. 23 (top edge of C11). Both show areas of angular hydration products in a fine grained, more porous C-S-H matrix, evidence of microcracking, and roughly equivalent amounts of porosity. In contrast, SEM of the specimens from the middle and center of the

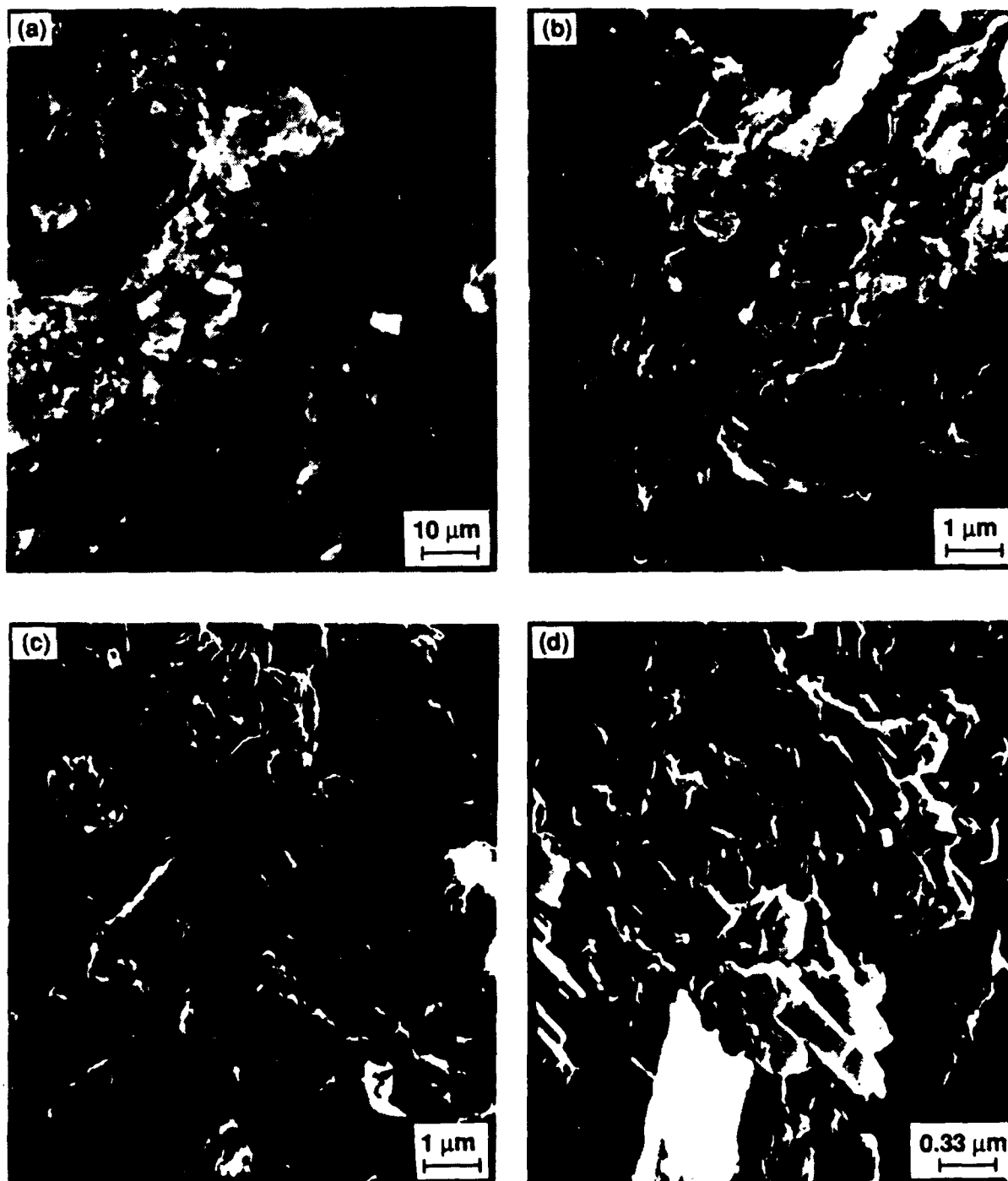


Figure 22. Scanning electron micrographs of the reference cement paste for recovery tests C11 and C12 taken at (a) low and (b-d) high magnification. Note reduced amount of porosity relative to previously characterized reference paste for tests C5 and C6 (Fig. 19).

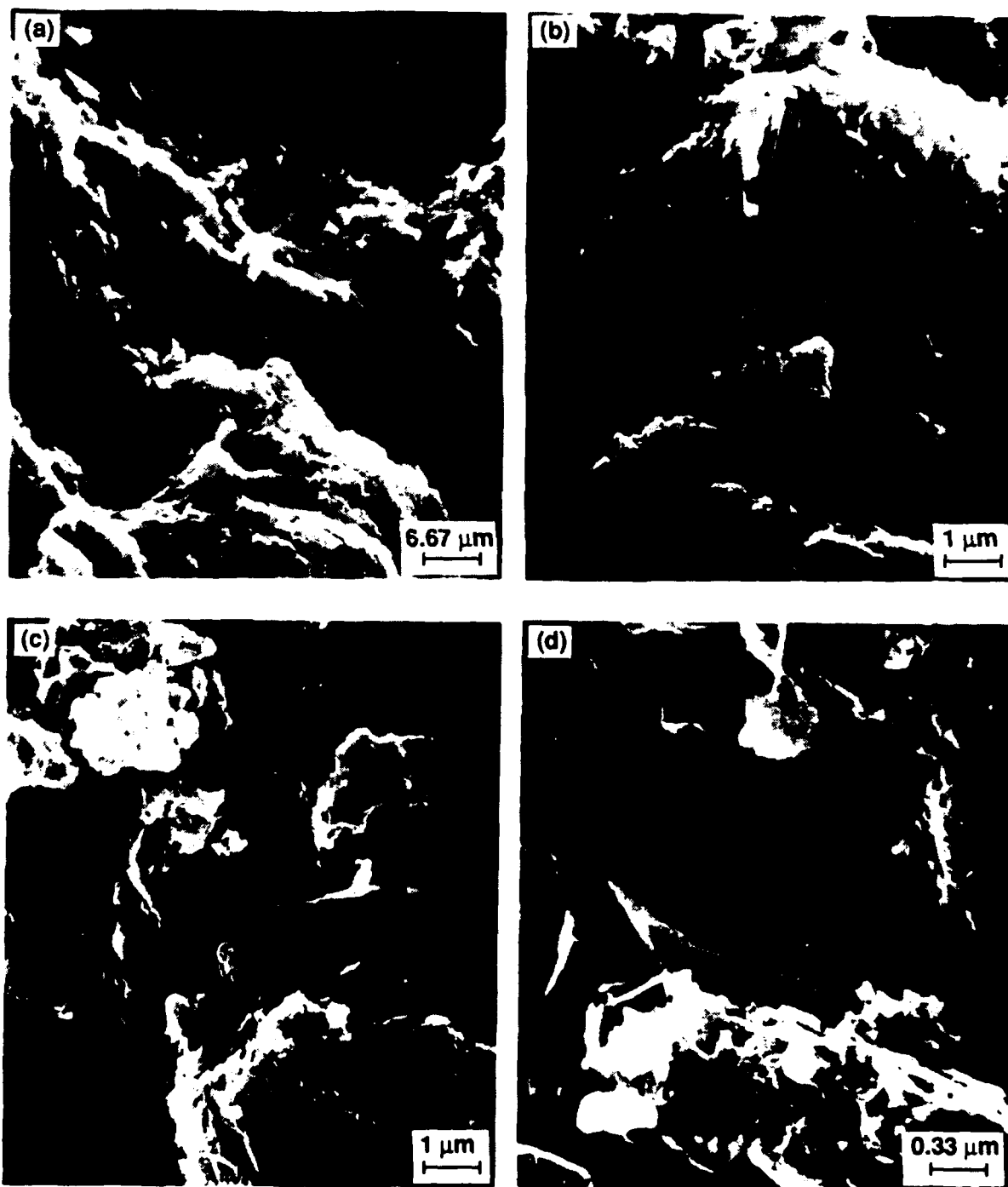


Figure 23. Scanning electron micrographs of fracture surfaces of fragments from the top outer edge of sample C11 showing typical features at (a) low and (b-d) high magnification.

top of sample C11 (Figs. 24 and 25, respectively) do not have significant amounts of any angular material, and thus have a more homogeneous texture. Most of these particles are discrete, submicron, rounded equant grains (C-S-H) that are compacted into dense agglomerates in some areas. Much of the porosity present in these samples is defined by the packing voids between the rounded particles; therefore, it is typically smaller than 0.2 μm . Visual comparison of photographs from the three different areas of the top of C11 indicate that the center of the sample is less dense than the outer edges.

A large, oriented sample was also recovered from shock test C12. The unshocked, reference microstructure to that sample has already been discussed (Fig. 22). Scanning electron microscopy was performed on several fragments removed from the top center of sample C12, with typical features presented in Fig. 26. As in most other recovered shock specimens, the microstructure is more homogeneous than that of the reference, consisting primarily of rounded submicron particles and typically no angular hydration products. High-magnification photographs [Fig. 26 (c) and (d)] show more, and larger, porosity relative to the unshocked paste. Other fragments from the bottom center of sample C12 show fracture surfaces that are also predominantly made of rounded particles. However, they are significantly more densely packed [Fig. 27 (a) and (b)] than those seen in the top of the sample. Although recognizable crystalline, i.e., angular, phases such as C-H are not generally observed in the fractured surfaces of shocked pastes, an obvious crystalline phase was noted in a specimen from the bottom of sample C12 [Fig. 27 (c) and (d)]. The mineral is highly fractured and, unlike those seen in the reference material [Fig. 22 (d)], shows rounding of the corners of individual fragments.

c. Plane-wave-initiated Explosive Shock in Mortar: Tests M5 and M6

There was no recovery of the test specimen in either of these tests. However, the mortar anvil, located just below the test specimen in the impedance fixture (see Fig. 11) was recovered in both instances. Despite the expected attenuation of the shock pulse that would have resulted in lower pressures in the anvil "specimens" compared to those experienced by the

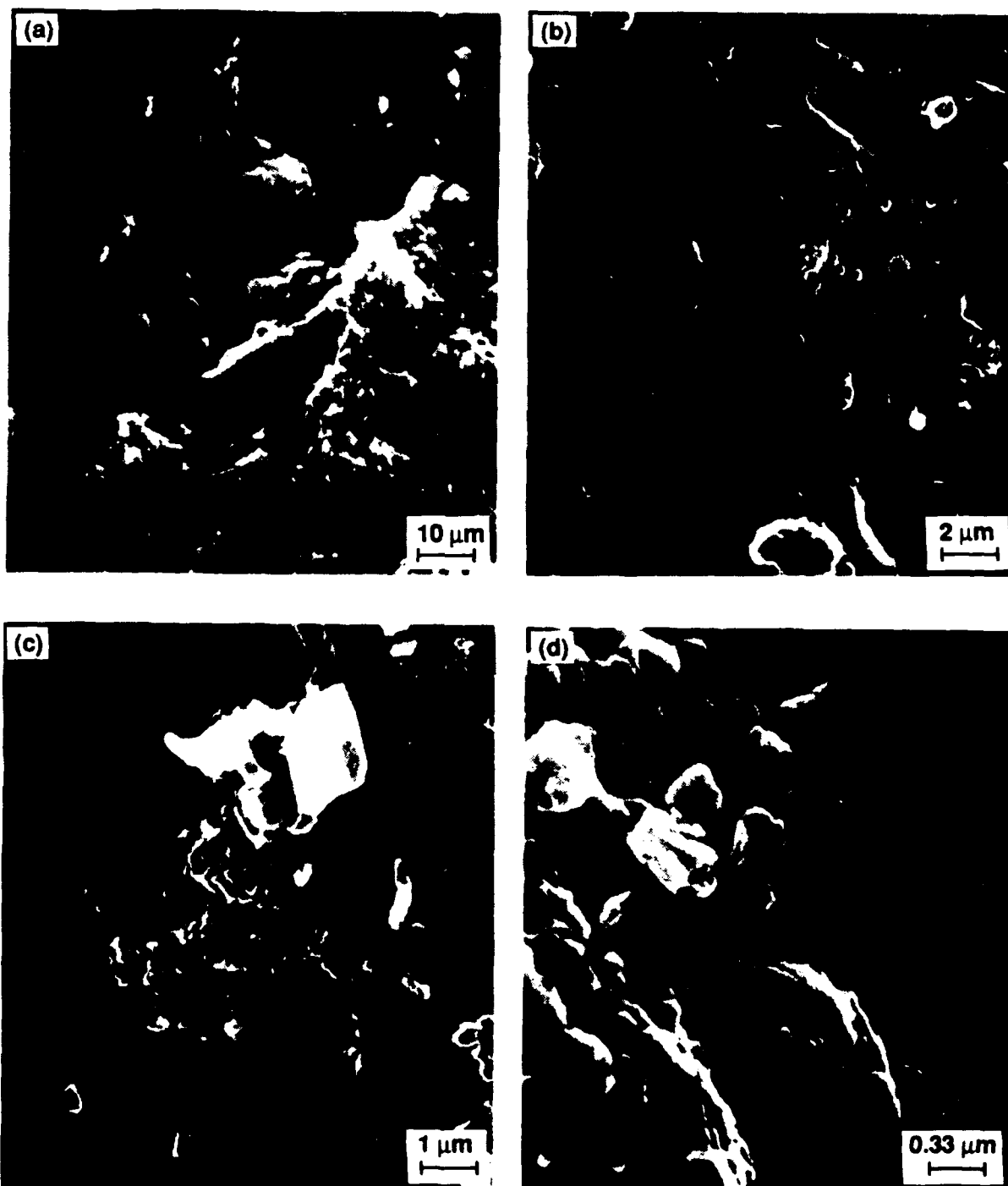


Figure 24. Scanning electron micrographs of fracture surfaces of fragments from midway between the outer edge and center of the top of sample C11 showing typical features at (a) low and (b-d) high magnification. Note the relatively homogeneous texture dominated by rounded particles.

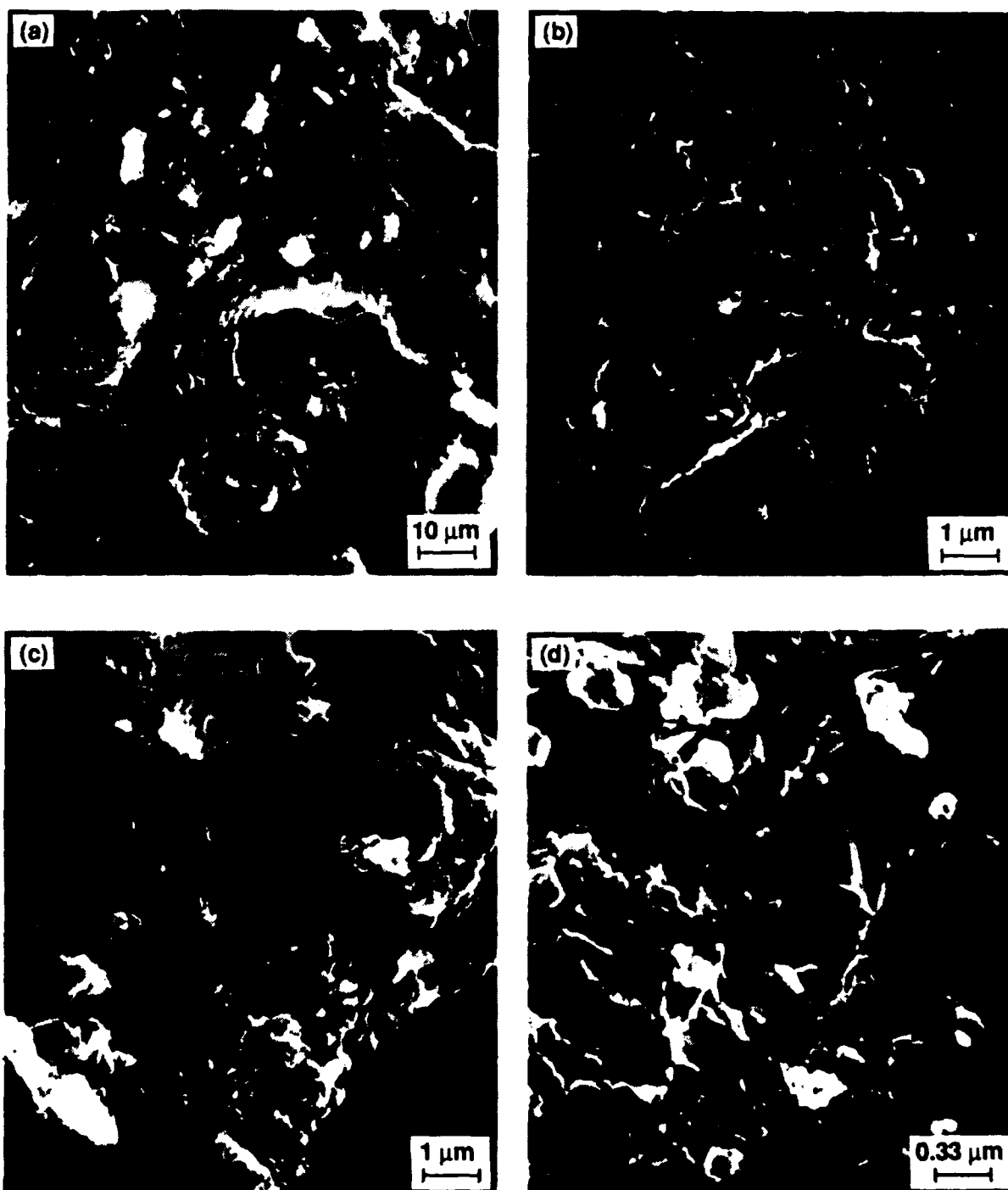


Figure 25. Scanning electron micrographs of fracture surfaces of fragments from the top center of sample C11 showing typical features at (a) low and (b-d) high magnification. Note the increased amount of porosity relative to the unshocked reference paste (Fig. 22).

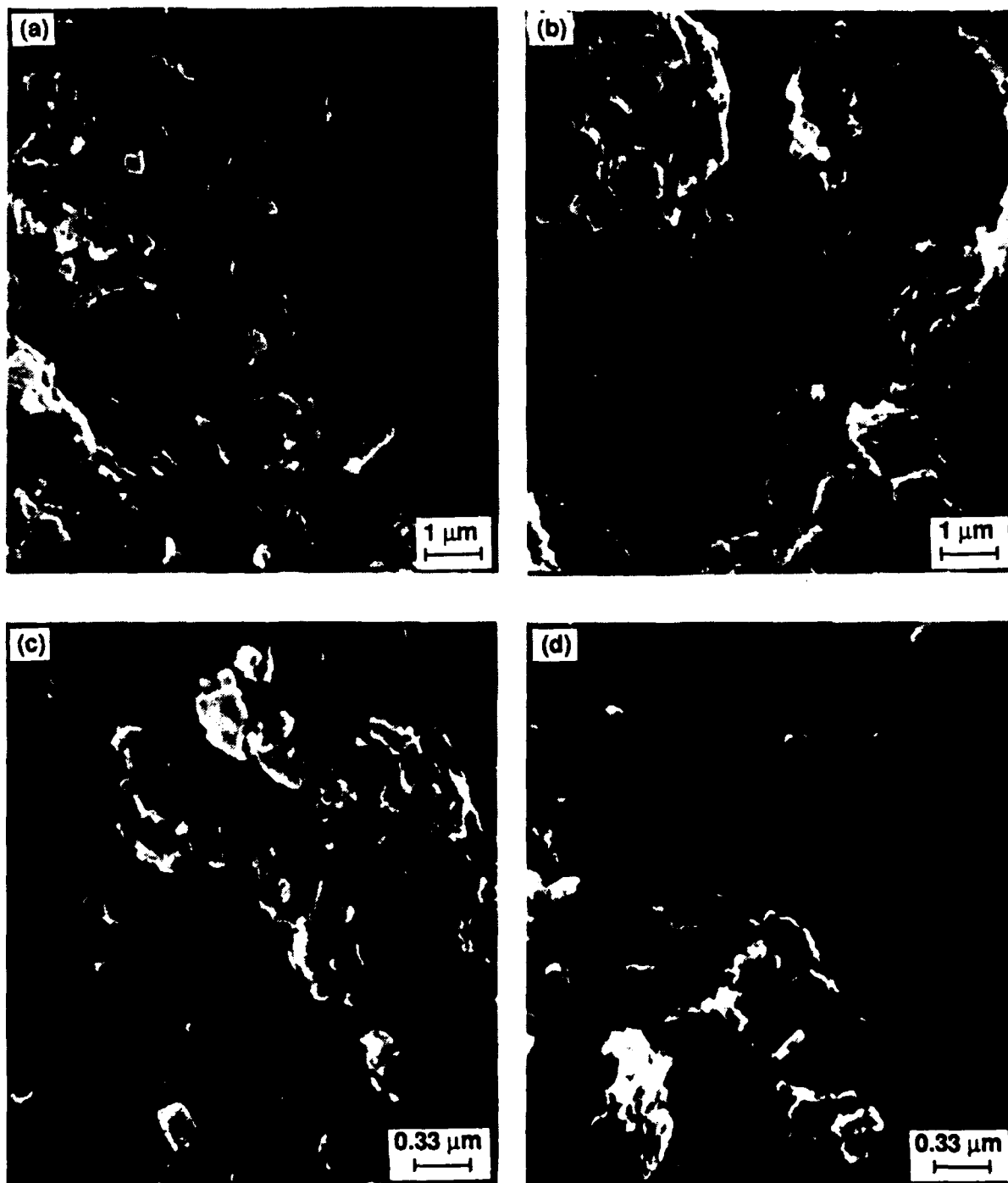


Figure 26. Scanning electron micrographs (a-d) of fracture surfaces of fragments from the top center of sample C12 showing typical features at high magnifications.

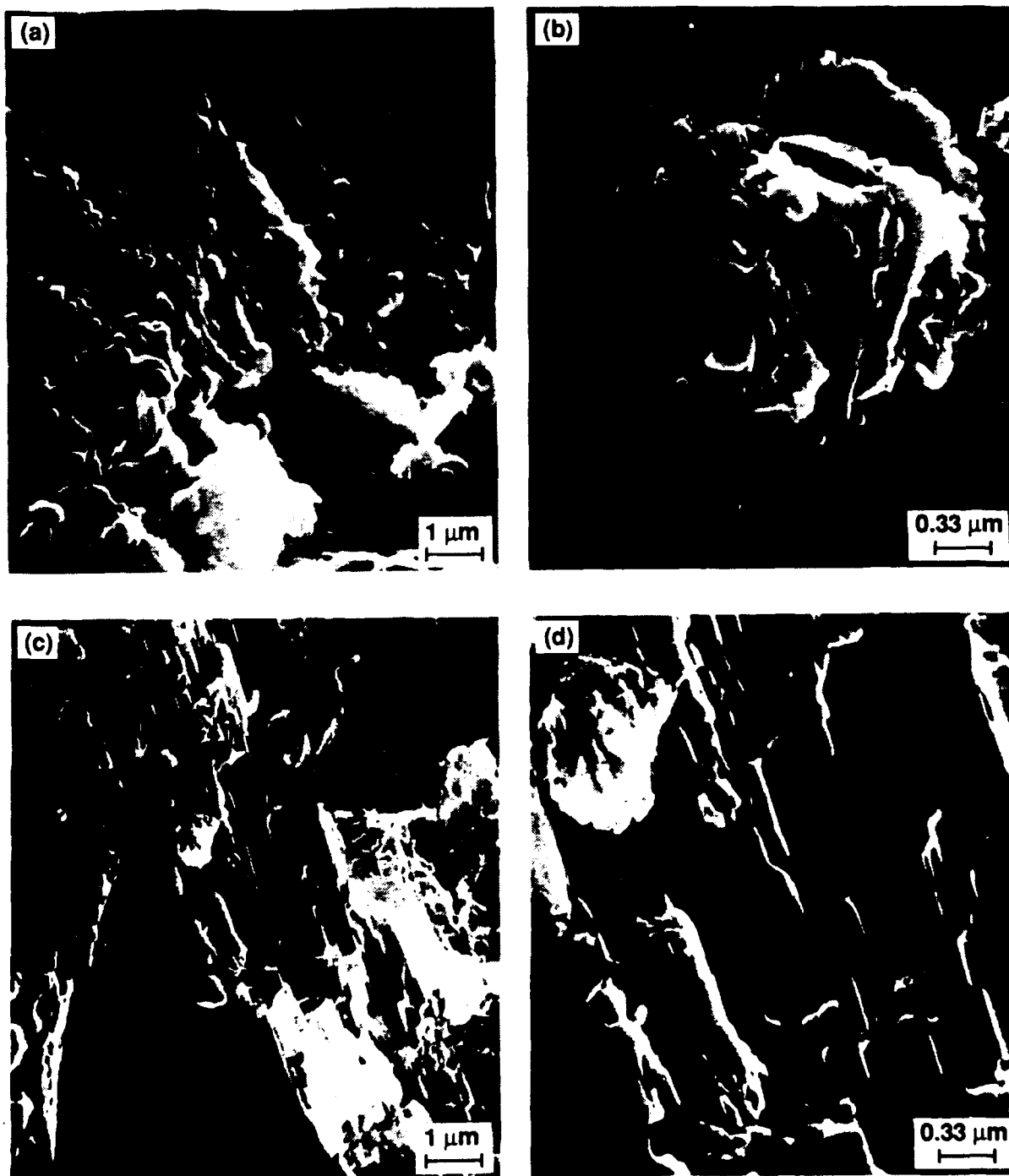


Figure 27. Scanning electron micrographs of fracture surfaces of fragments from the bottom center of sample C12 showing typical features at high magnifications. Note fragmentation and rounding of corners of the C-H mineral (c and d) relative to the C-H in the reference paste (Fig. 22d).

destroyed test specimens that were closer to the explosive lens, the microstructure of the shock-loaded mortar was significantly altered from that seen in reference specimens.

Representative micrographs (Fig. 28) of the unshocked mortar microstructure show large amounts of porosity with an average size of approximately $0.2\ \mu\text{m}$ and some larger voids with sizes that range between $1\text{--}5\ \mu\text{m}$. Much of the fine porosity is defined by angular hydration products (ettringite), as seen in Fig. 28 (d). Quartz grains as big as $100\ \mu\text{m}$ have been observed, and some porosity was noted along the quartz/cement interfaces (Fig. 28 (a)).

In contrast, micrographs of shocked mortar (Fig. 29) show almost no angular cement phases, virtual elimination of the porosity that occurred in intergrowths of needle-like hydration products, and numerous fractures that occur within the cement matrix and quartz grains and along quartz/cement interfaces. Most of the cement matrix also has been transformed into rounded granules, as noted in prior tests in cement paste alone. Examination at high magnification [e.g., Fig. 29 (d)] shows an internal structure in some of the cement grains that suggest comminution, compaction, and fusion of angular material. Other cement particles, e.g., the rounded granules, do not show internal structure at similar magnification. At low magnification, shocked microstructures appear more massive and homogeneous [Fig. 29 (a)] than those of unshocked specimens [Fig. 28 (a)].

5. Mercury Porosimetry

Mercury intrusion porosimetry is a commonly used method to analyze the structure of materials with open, connected porosity.[9] The technique involves the intrusion of mercury into the sample by application of external pressure, and measurements of the volume intruded versus pressure. The volume of mercury intruded at a specific pressure depends on the pore size and the pore volume of the material: the smaller the pores, the higher the pressures required to accomplish intrusion. Thus, mercury intrusion gives information

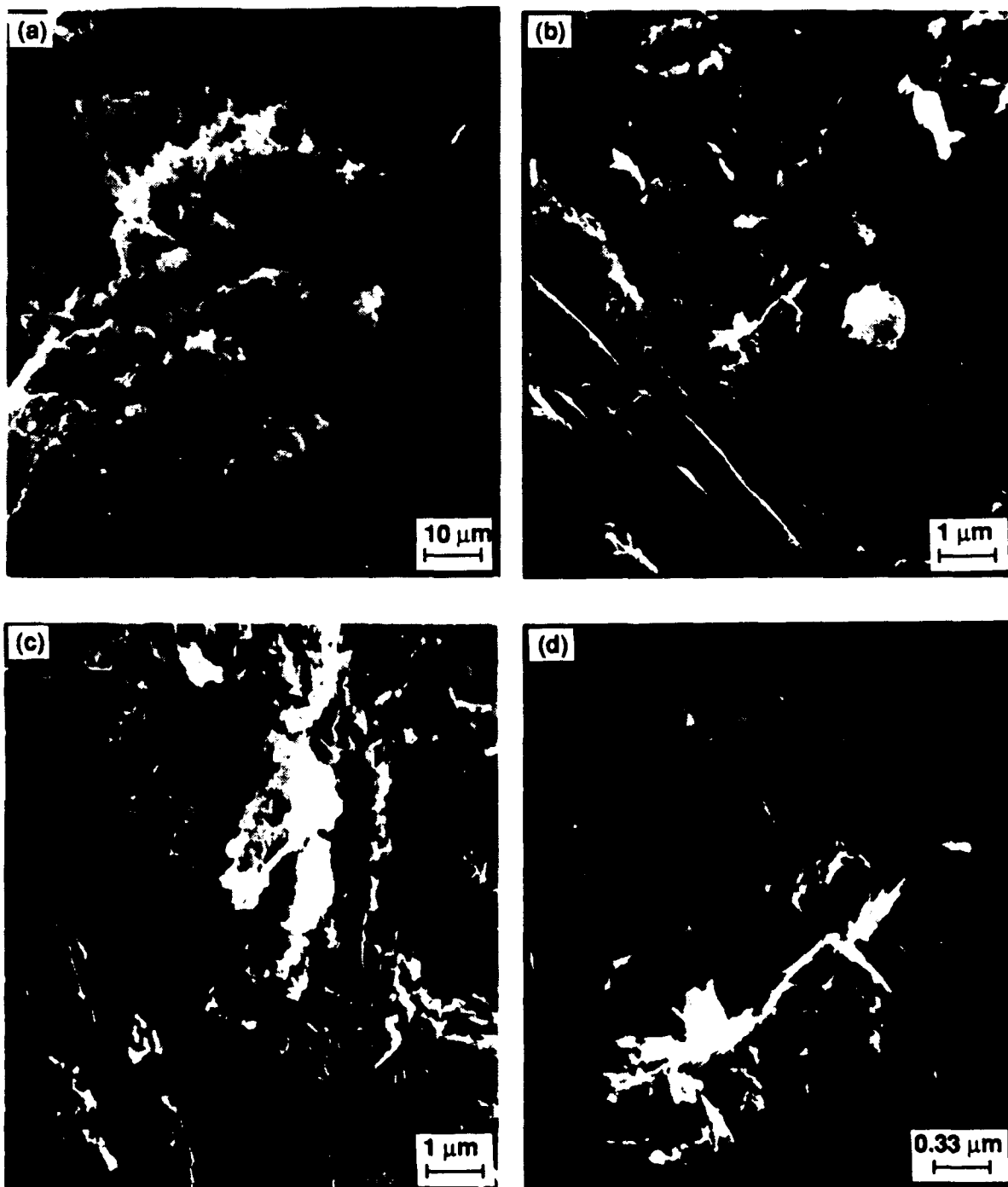


Figure 28. Scanning electron micrographs of fracture surfaces of fragments of unshocked mortar for reference to recovery samples M5 and M6 showing typical features at (a) low and (b-d) high magnifications.

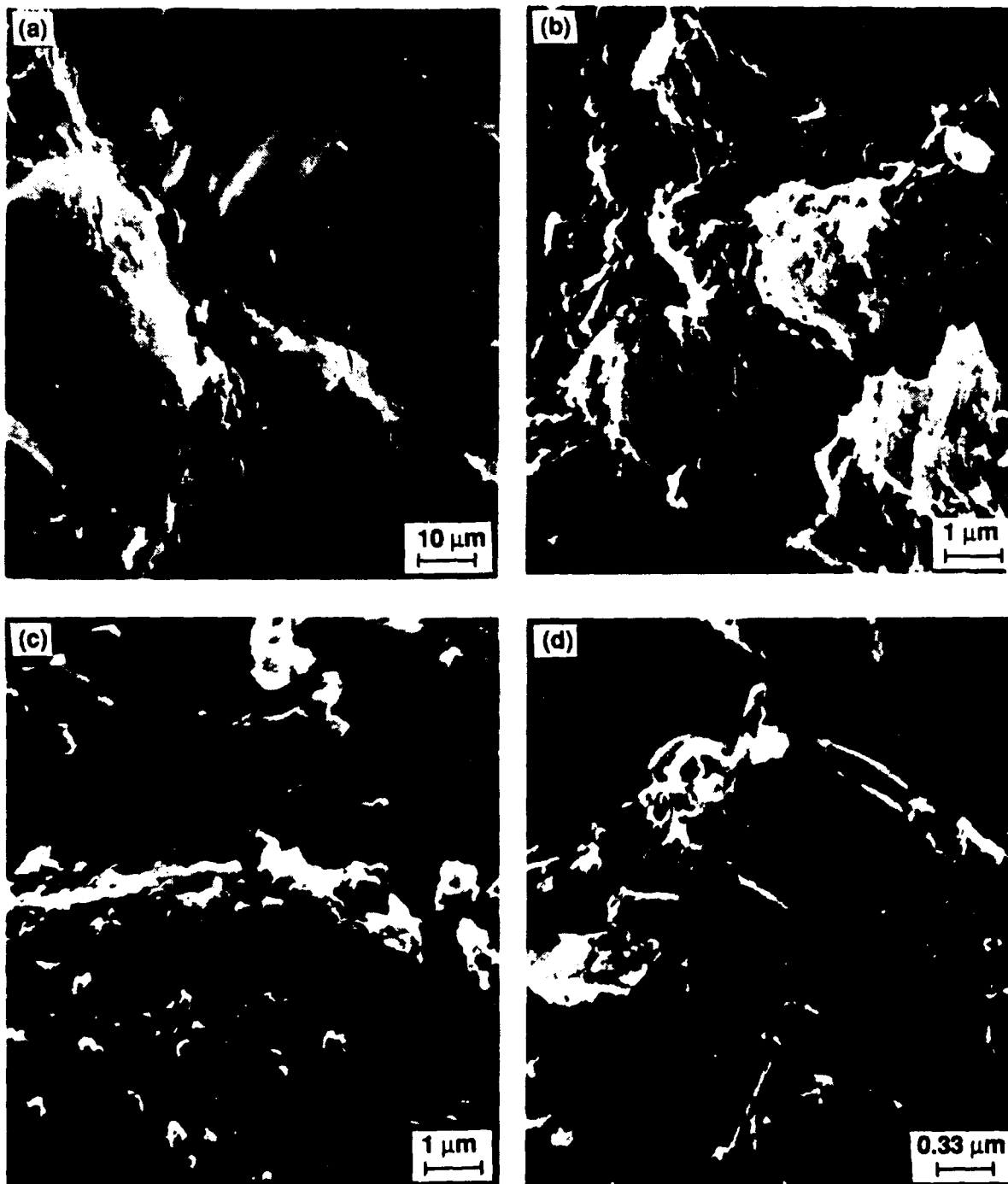


Figure 29. Scanning electron micrographs of fracture surfaces of fragments of recovered mortar anvils from tests M5 and M6 showing typical features at (a) low and (b-d) high magnifications.

about 1) the total porosity, 2) pore size distribution, and 3) bulk and theoretical densities. The pore size calculation is based on the well-known equation for the excess pressure, Δp , across a meniscus

$$\Delta p = \left(\frac{1}{r_1} + \frac{1}{r_2} \right) \gamma \quad (6)$$

where r_1 and r_2 are the radii of the meniscus, and γ is the surface tension. It is assumed that the pores are cylindrical, so that $r_1 = r_2$, and in the case of a non-wetting liquid like mercury, the pore diameter can be expressed as:

$$d = \frac{4 \gamma \cos \theta}{p} \quad (7)$$

Note that if the mercury were intruding into a crack of width t , then $r_1 = t/2 \cos \theta$ and r_2 is infinite, and so

$$t = \frac{2 \gamma \cos \theta}{p} \quad (8)$$

which is half the equivalent cylindrical diameter. Because pores are rarely cylindrical, only approximate pore diameters are measured. However, its use is generally accepted as a practical means of treating that would otherwise be a complex problem.[10]

The pore structure of cement paste consists mainly of gel pores and capillary pores. Gel pores, which average 1.5 - 1.8 nm in diameter, are the nonsolid parts of finely divided hydration products, primarily C-S-H. Capillary pores constitute a continuous interconnected network in fresh cement paste. Their size and volume depend on the water content and the degree of hydration in a particular paste. Although both the unshocked and shocked specimens were allowed to continuously hydrate before pore-size analyses were performed, they have similar histories and therefore, comparable microstructures.

Kinetic hysteresis effects, volume hysteresis effects (described in Fig. 30), and contact angle measurements contribute to errors in mercury porosimetry.[9] The largest source of error comes from assuming a constant value for the contact angle, since the surface chemistry of the pore walls may

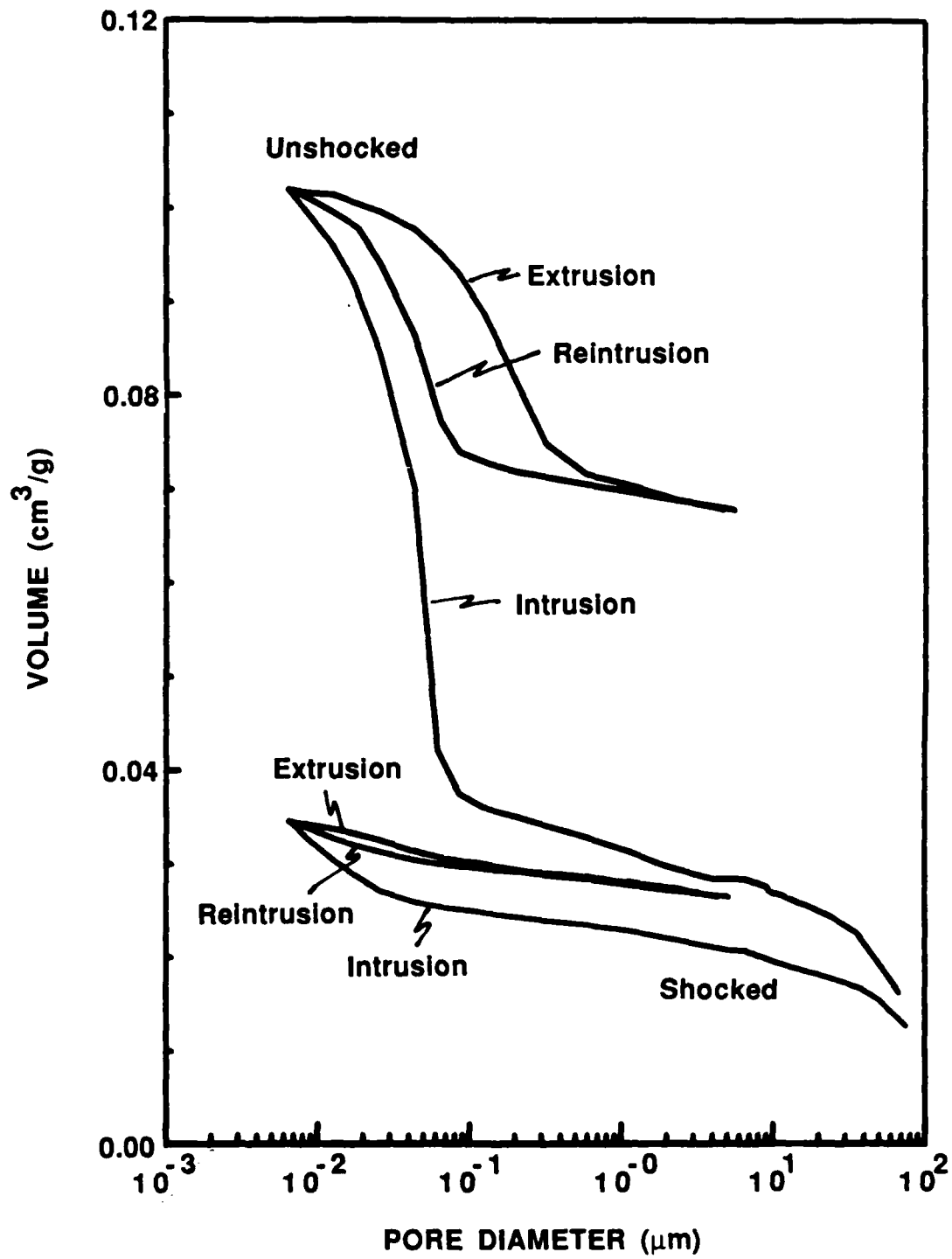


Figure 30. Cumulative porosimetry data for unshocked and shocked cement pastes showing volumetric hysteresis effects.

vary throughout the cement. If the assumed value of the contact angle is off by more than 20 degrees, the actual pore diameter may be off by 50% or more. Based on previous research on portland cement,[10] an average contact angle of 117 degrees was used in this study. Kinetic hysteresis can cause the distribution curve to shift if intrusion readings are taken before equilibrium has been obtained.

Previously,[11] we recorded pore intrusion measurements while continuously increasing external pressures. However, we later found that continuous scans did not allow sufficient time for the mercury to fully intrude the pore structure of the paste, resulting in kinetic hysteresis. Accordingly, we modified the technique by increasing external pressures at discrete intervals and holding each for 5 minutes to allow the mercury to fully intrude the pores before intrusion measurements were recorded.

Volume hysteresis is caused by the retention of mercury by the pores of the sample after the pressure has been reduced to 1 atm. This type of hysteresis may be associated with pores that have constricted necks, such as the classic "ink bottle"-shaped pores. Because Eq. #7 assumes cylindrical pores, the pore diameter calculated is only the diameter of the opening of the pore and not necessarily the largest diameter of the void.

Volume hysteresis was measured directly as follows. After the initial intrusion, mercury was extruded from the sample by gradually lowering the pressure and then re-intruded. Comparison of the initial intrusion and re-intrusion volumes (hysteresis) indicates the amount of constricted porosity within the sample, i.e., those pores that are connected through "bottle-neck" openings. Further, differences in the extrusion and re-intrusion behavior are related to differences in the contact (wetting) angle as the mercury advances or recedes from the pores. Others [12] have reported that the magnitude of the difference between advancing and receding contact angles reflects the surface roughness of the pores and/or the chemical heterogeneity of the pore walls, i.e., the surface energy. Therefore, the difference between the two contact angles is small for smooth, homogeneous pores.

Mercury porosimetry was performed on separate samples of the shocked

and unshocked cement specimens from each w/c ratio (0.25, 0.33, and 0.40). A maximum of 138 MPa (20,000 lb/in²) was used to intrude the smaller pore diameters (corresponding to a size of ~ 70 nm). A ~ 2 g sample was placed in the porosimeter cell of a Micrometrics Model 9300 pore sizer and evacuated to 10⁻² torr. Mercury was then introduced to a pressure of approximately 1 psi -- this pressure and volume define the zero state. Mercury was then intruded and volumes measured up to the maximum pressure.

General observations made from the porosimetry analyses include:

- Pore-size distributions from reference samples from different test series have similar features, but are not reproducible
- Pore-size distributions from reference samples from the same test series are very reproducible, especially percent porosity, percent "bottle-neck" porosity, and mean and median pore sizes
- HSR loads broaden the size distribution of capillary porosity
- Shock loading causes changes in the amount of porosity as well as in the mean and median pore sizes
- Shock loading reduces the amount of bottle-neck porosity, and, in some instances, introduces larger porosity (1-10 μ m) that may represent microcracking.

Pore size distributions for two samples of reference cement (R11/R12) and shocked cement (C11/C12) are shown in Fig. 31. The distributions are characterized by a sharp peak around 0.05 μ m and a broad distribution above 10 μ m: (Note: remember that the pore volume is given by the area under the curve.) The gel porosity, which typically has diameters <0.01 μ m, was not penetrated by the pressures used in these experiments. The porosity in the

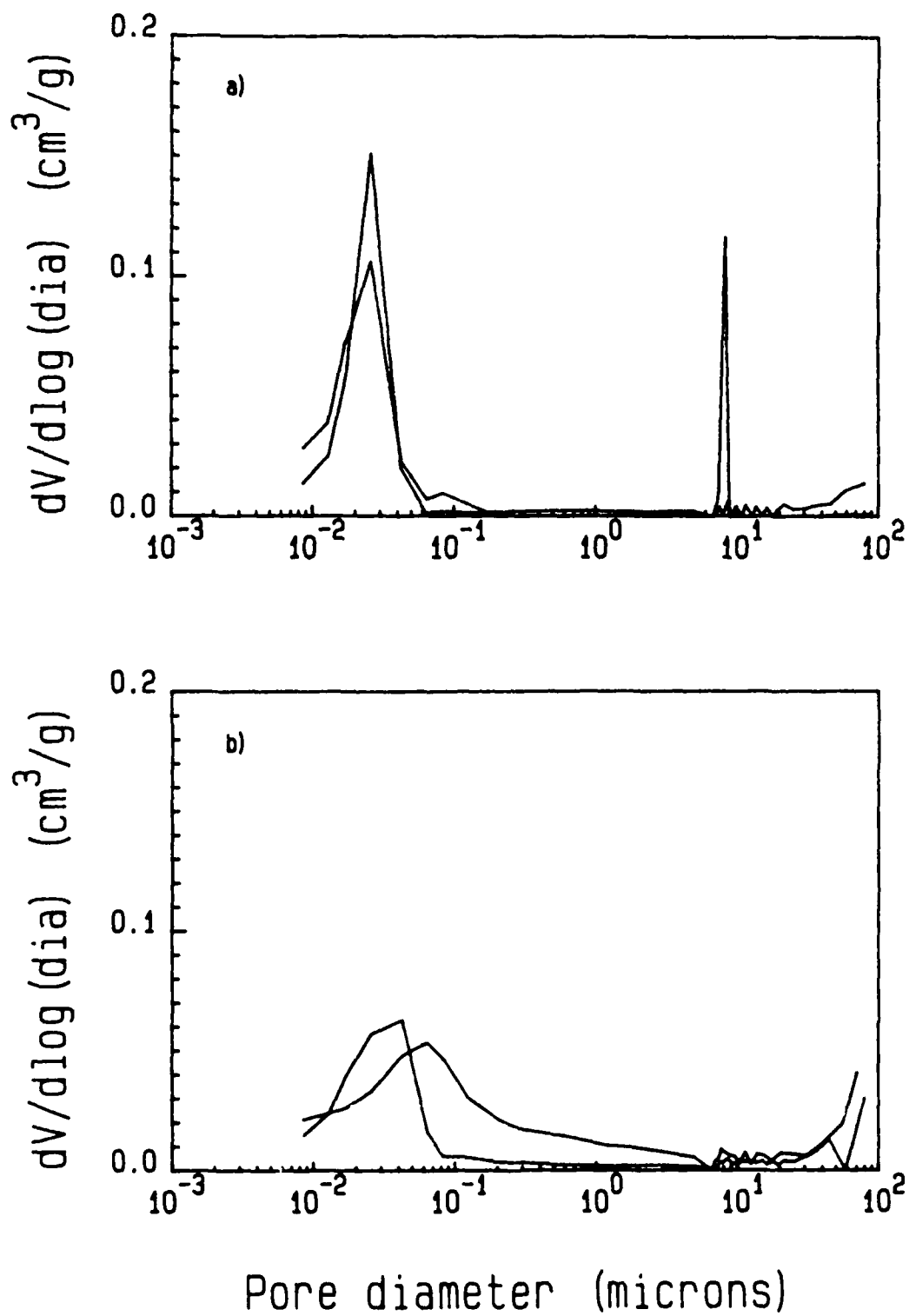


Figure 31. Pore size distribution for two samples of a) reference cement R11/R12 and b) shocked cement (C11 and C12).

range 0.01-1.0 μm is likely to be capillary pores and/or microcracks. The volume above 10 μm represents much larger (visible) cracks and holes in the samples. The agreement between the two curves is excellent.

Data for the reference cements are listed in Table 6. The percent porosity is given for two ranges ($\leq 10 \mu\text{m}$ and $> 10 \mu\text{m}$) in addition to the total. This was done to separate apparent disparities that could occur if just one large crack were present. Nevertheless, the capillary porosities ($< 10 \mu\text{m}$) of the samples show significant scatter. This is likely due to minor differences in the histories of the cements and indicates the importance of having a reference measurement for every sample that was shocked. Note that the variations within the two sets of duplicate samples -- two different R5 samples, and R11 and R12 (which were reference samples from the same casting) are much less than the total range of porosity (8.81 - 14.14%) in Table 6. The theoretical densities, which should be essentially constant, also vary. The volume within the bottlenecks was measured from the extrusion curve at 10 μm and represents the percentage of pore volume with openings below 10 μm that is entered through a bottleneck. The median pore diameter is the 50% point in the cumulative distribution and the mean pore diameter is defined as the position of the peak in the distribution curve. Some scatter is again evident in the values obtained for the reference materials although samples from a single casting (test series) have similar histories, and therefore similar median and mean pore diameters. Clearly much time could be spent studying the aging behavior of cement, but that was not the objective of this work. Examples of the shock response of the sample porosity may be seen through comparisons of the unshocked reference cement paste and mortar samples.

The data for the shocked samples are generally presented in order of increasing strain rate and shear-loading component and are summarized in Table 7.

Relatively low strain-rate (10^3 s^{-1}) dynamic experiments were conducted using the SHPB. The pore-size distribution of two samples from SHPB experi-

Table 6

REFERENCE SAMPLES

Sample	Porosity (%)			Density Bulk/Theor. (g/cm ³)	% Vol. in Bottleneck	Surface Area (m ² /g)	Pore Diameter Median/Mean (μm)
	>10μm	≤10μm	Total				
MTS	1.76	12.76	14.52	1.959/2.29	43.9	8.425	0.0369/0.055
R11	0.589	9.60	10.19	1.96/2.18	---	10.30	0.021/0.025
R12	2.11	9.22	11.33	2.11/2.38	62.7	11.56	0.021/0.027
R5	5.83	13.98	19.81	1.94/2.42	52.5	9.71	0.052/0.065
	3.30	14.14	17.44	1.94/2.35	55.1	9.91	0.052/0.065
R6	No Data						
R7	1.58	8.81	10.39	1.97/2.21	---	9.90	0.021/0.025-0.035
M5 (Mortar)	2.95	18.26	21.21	1.97/2.49	55.3	11.24	0.052/0.061
M6 (Mortar)	3.78	11.54	15.32	1.89	2.33	8.08	0.1034/0.061-0.085

Table 7

SHOCKED SAMPLES

Sample	Porosity (%)		Density Bulk/Theor. (g/cm ³)	% Vol. in Bottleneck	Surface Area (m ² /g)	Pore Diameter Median/Mean (μm)	Location	
	>10μm	≤10μm						
SHP8	1.99	10.95	12.94	1.98/2.28	45.0	9.64	0.034/0.042	---
	1.59	9.89	11.48	1.98/2.24	52.1	10.34	0.034/0.040	---
C11	2.75	12.73	15.38	1.96/2.32	39.1	7.93	0.738/0.070	Right half
	1.71	9.18	10.89	2.12/2.38	---	8.01	0.034/0.030-0.040	Left half
	1.84	8.47	10.31	2.04/2.27	42.7	8.72	0.033/0.030	Bottom
	2.30	11.05	13.35	1.92/2.21	45.0	9.61	0.034/0.045	Top
C12	---	---	17.90	3.24/3.94	37.2	5.96	0.051/0.040	Top
	1.93	11.37	13.30	1.93/2.22	40.2	10.01	0.034/0.040	Top
	1.63	12.49	13.12	1.96/2.26	39.4	9.97	0.033/0.040	Bottom
C5	1.57	10.04	11.61	1.96/2.22	41.8	9.80	0.034/0.035	Bottom
	4.94	2.83	7.77	2.24/2.43	40.4	2.95	32.95/No Mean	---
C6	3.34	3.81	7.15	2.23/2.40	46.2	3.63	3.63/No Mean	---
	3.24	8.7	11.94	2.16/2.45	46.2	8.97	0.034/	---
C7	2.28	4.49	6.77	2.08/2.23	---	4.62	0.033/0.025	---
M5/M6 (mortar)	3.22	12.41	15.63	2.15/2.54	32.9	6.85	0.164/0.041	Top of
	8.01	7.31	15.32	2.29/2.71		5.50	0.255/0.041	anvil

ments are shown in Fig. 32 together with that of a reference specimen which also had been fractured but at a very low strain rate (MTS machine). Good agreement is seen between the two SHPB samples. Both have a broader distribution than the reference but as can be seen from Tables 6 and 7 the median and mean pore diameters have only decreased slightly, relative to the reference. The total porosity also decreases a small amount and the amount of bottleneck pores is similar.

Samples C11 and C12 were subjected to a plane-strain shock wave from an explosive lens, i.e., nominally no shear component. Figure 33 shows pore size distributions for samples from test C11 recovered from different locations in the test, plotted together with the reference sample pore-size distribution. In every sample the shock has broadened the distribution in the capillary porosity region. This effect is especially pronounced in the samples taken from the sides where significant porosity is observed in the 0.1 - 10.0 μm range. This latter porosity may be due to microcracking. In addition to the broadening, a shift in median and mean pore diameters is evident from Tables 6 and 7. It is not possible to determine any change in the pore volumes because the capillary porosities measured for the shocked samples contain within their scatter the value for the reference. Figure 34 shows pore-size distributions of samples taken from the top and bottom of C12 along with a reference specimen pore-distribution. Again the major effect is one of broadening the distribution and shifting the peak to slightly larger pore diameters. It should be noted that the agreement between the C12 curves is good and also that they somewhat resemble the curves for the top and bottom samples from C11. However, there is a small increase in the amount of capillary porosity in C12 and the percentage in the bottlenecks is decreased. Note that an extrusion run was not performed on C11 so this information could not be determined for that shock test.

The most disruptive tests, according to the degree of change seen in the porosimetry analyses were C5 and C7. In these runs a convex shock wave was sent through the cement so that it experienced a "uniaxial" strain pulse with the possibility of a significant shear component (of undetermined magnitude). Figures 35 and 36 show the pore size distributions for C5 and C7

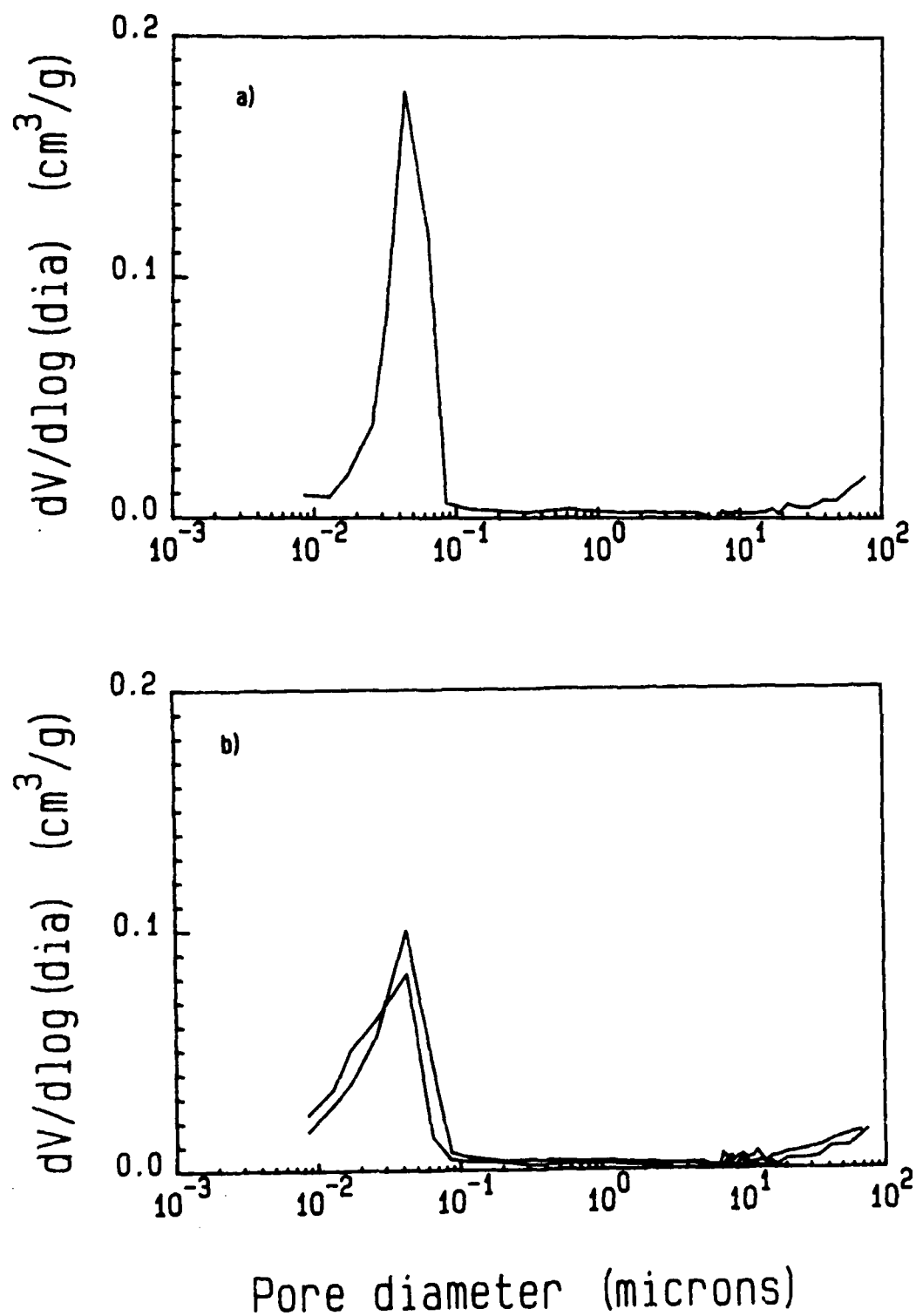


Figure 32. Pore size distribution of a) reference (fractured at low strain rate) and b) SHPB-tested samples.

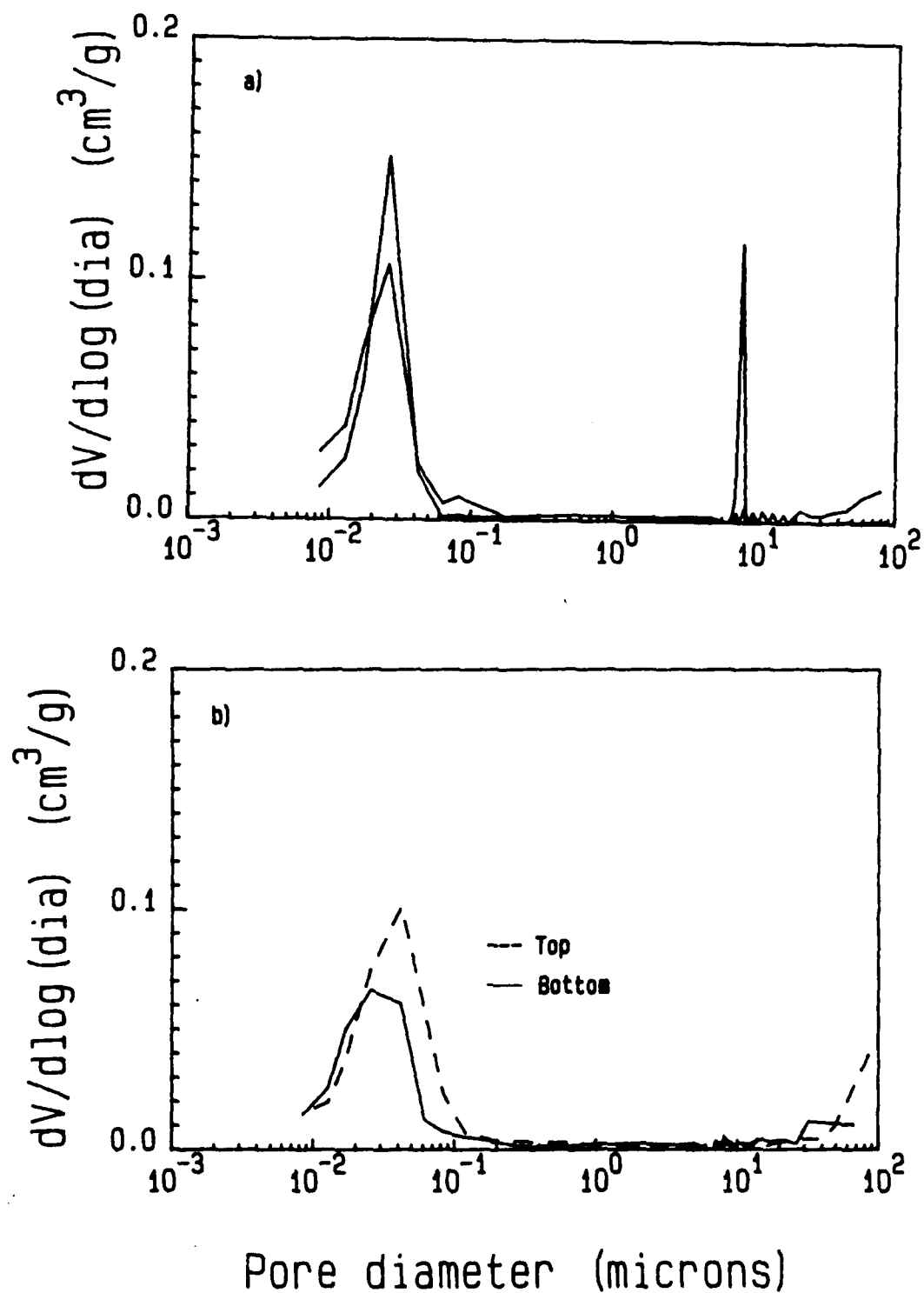


Figure 33. Pore size distribution for a) reference (R11/R12) and b) shocked cement from test sample C11.

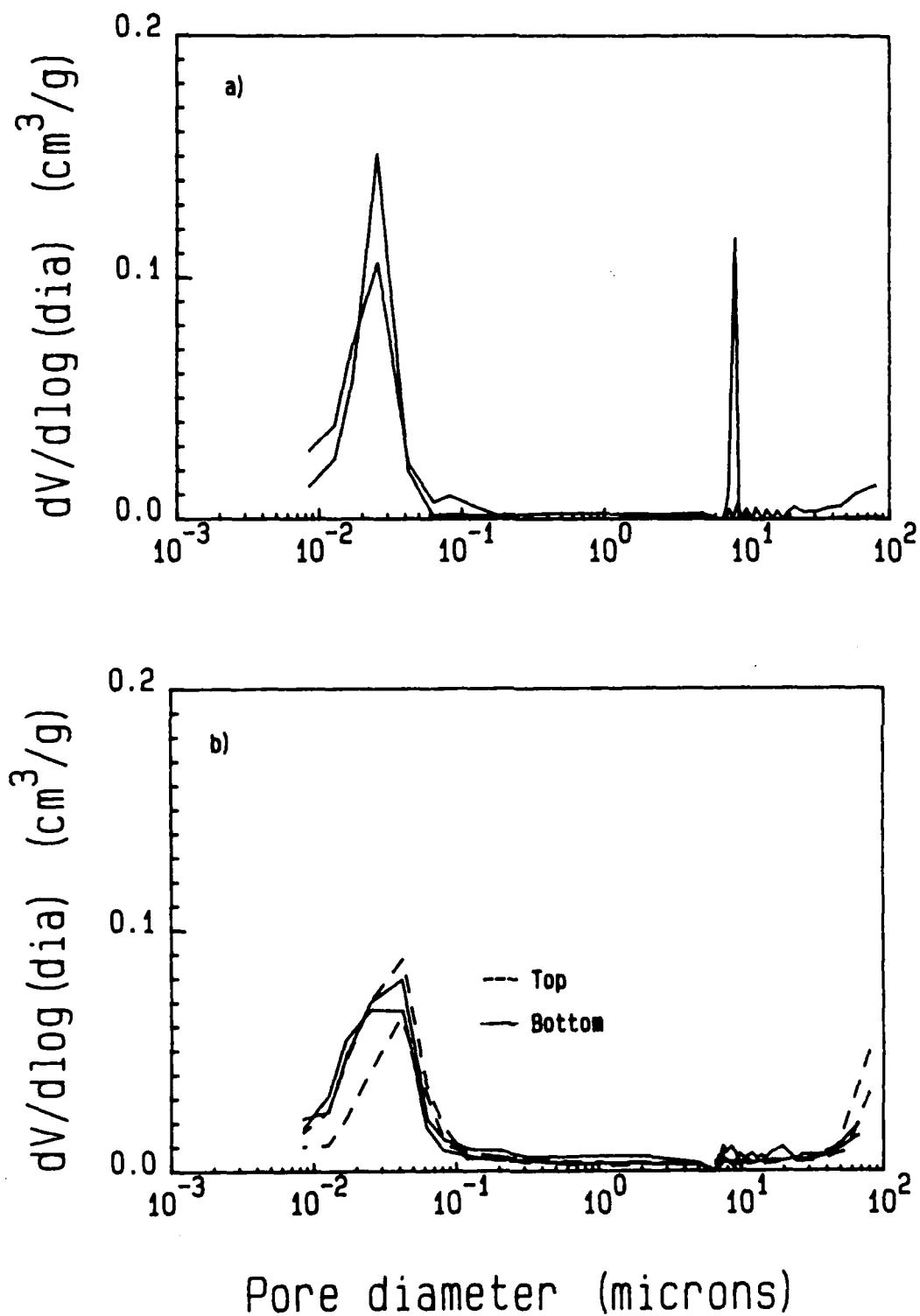
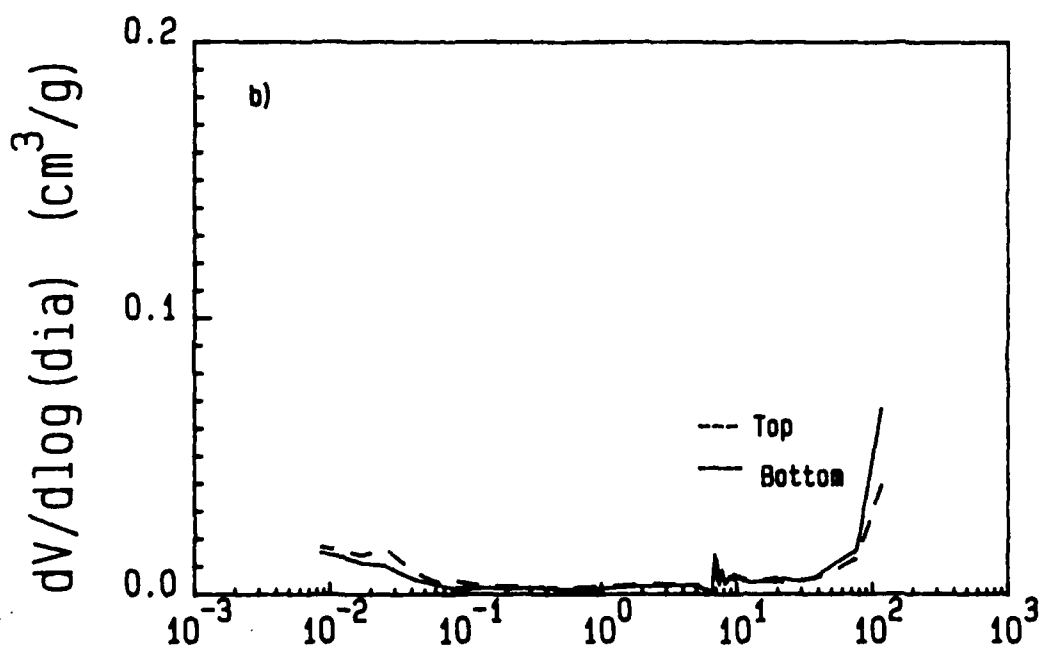
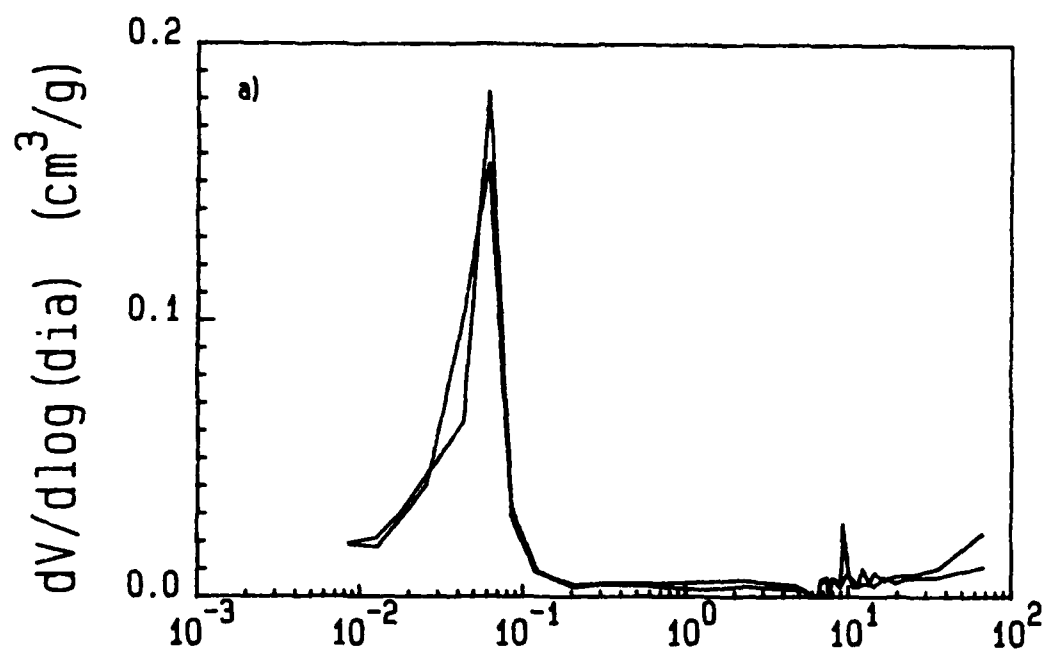


Figure 34. Pore size distribution for a) reference (R11/R12) and b) shocked cement from test sample C12.



Pore diameter (microns)

Figure 35. Pore size distribution for a) reference (R5) and b) shocked cement from test sample C5.

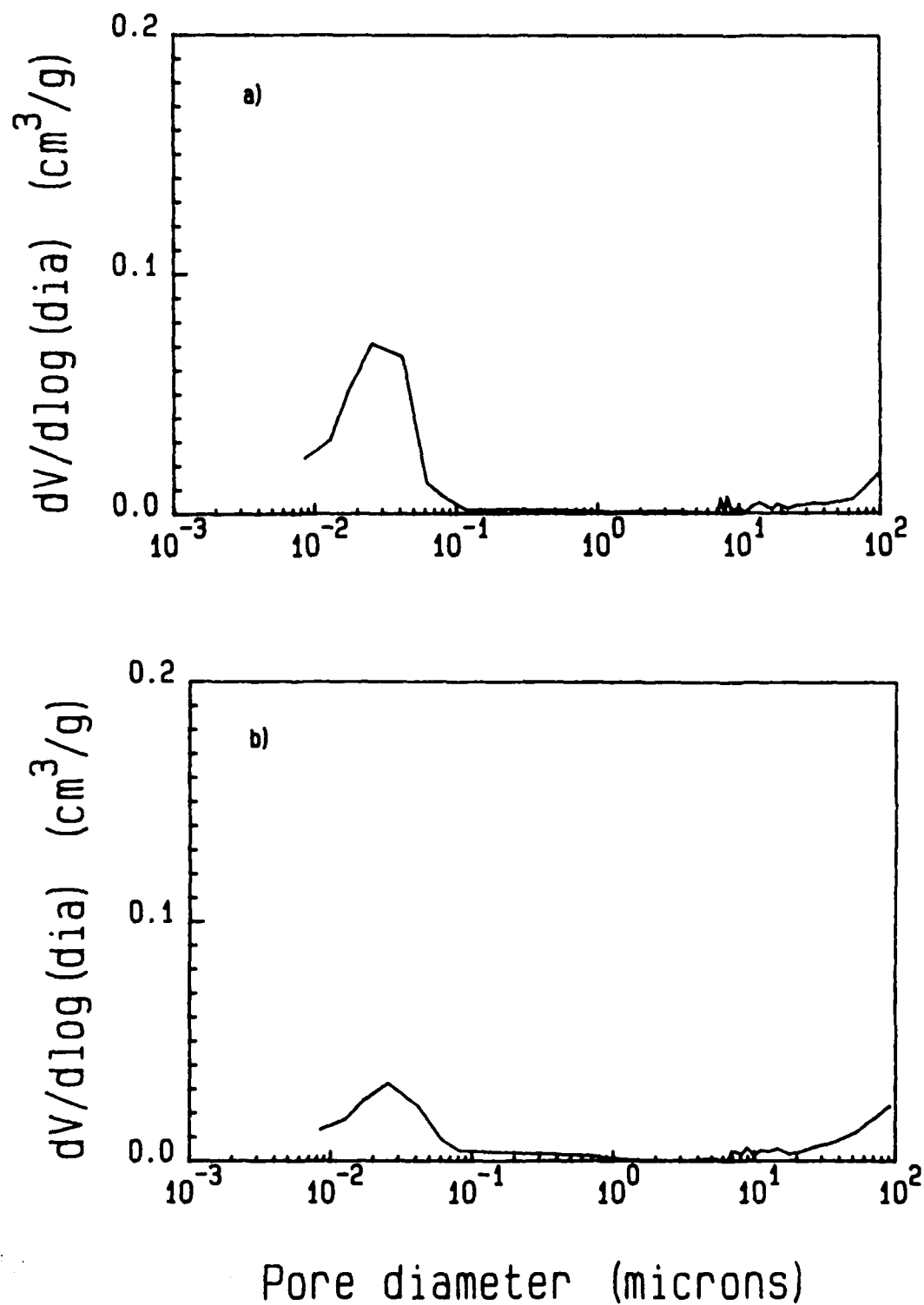


Figure 36. Pore size distribution for a) reference (R7) and b) shocked cement from test sample C7.

together with the appropriate references. It is readily apparent that the capillary porosity has been almost totally destroyed by some mechanism, more so in C5 than in C7. This shows up in Table 7 as a dramatic drop in capillary porosity. In C5 the capillary porosity has decreased from ~14% to ~3%. This represents an extreme of the broadening observed in the other shocked samples. In the two C-5 samples studied, there is no peak in the distribution curve and no appearance of porosity (microcracks) in the 0.1 to 10.0- μ m range after the shock.

Figure 37 and Table 7 show the pore size distributions and summary data, respectively, for the reference and shocked (M5) mortar samples. The shocked mortar sample had been loaded with a planar shock wave, i.e., one initiated from an explosive lens. The reference mortar samples have a broader peak in the capillary range and a far greater volume in the 0.1 to 10- μ m range than the cement samples. The total porosity is also slightly higher than the average measured for the cement samples but because of the scatter in these data, and the differences in maturity of cement and mortar samples at the time of testing, this is not necessarily significant. Similarly the median and mean diameters appear slightly higher than the cement values. The shock test dramatically broadens the pore size distribution in the mortar and reduces the capillary porosity although the volume in the range 0.1-10 μ m actually increases. This effect is more severe than that recorded for the similar tests on cement (C11 and C12).

E. DISCUSSION

The characterizations of the recovered shock-loaded cement and mortar samples have shown changes in microstructure that we have attributed to the loading event through comparisons with reference samples. In general, XRD has shown peak broadening of hydrated phases, reduction in peak intensity (crystallinity ?) of C-S-H and, in some tests (C6, C11, and C12), shifts of peak locations to smaller d-spacings. According to the SEM analyses of fracture surfaces, consistent shock effects were granulation of the predominant C-S-H phase and elimination of angular hydration products from the microstructure. There also were variations in the magnitude of the shock

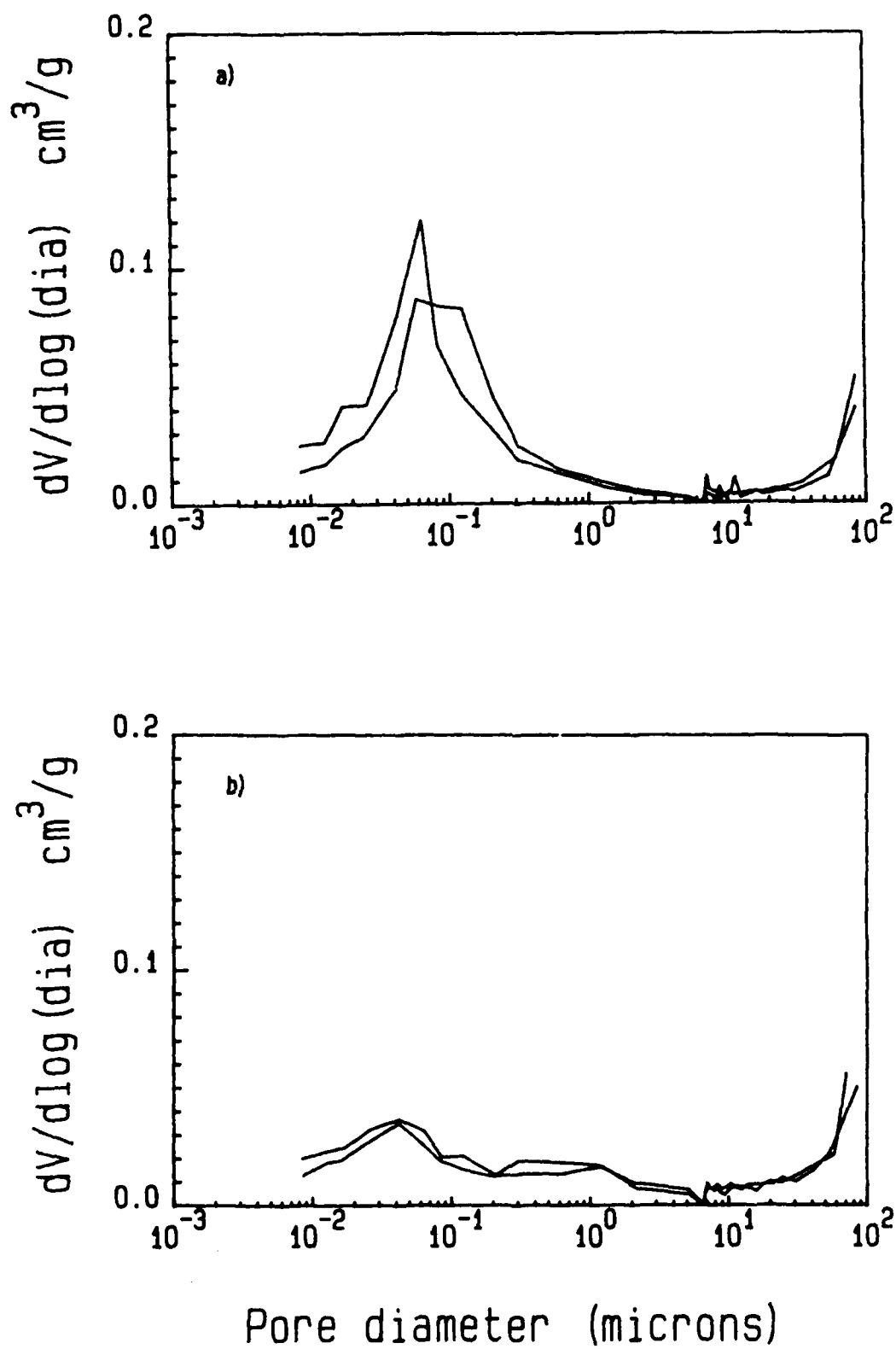


Figure 37. Pore size distribution for a) mortar reference (M5) and b) shocked mortar sample from test M5.

effect with different locations within the same sample, including significant differences in the size and amount of fine (typically submicron) porosity. Mercury porosimetry also showed changing in the porosity, i.e., broadening of the pore-size distributions, in response to shock and even to high-amplitude elastic loading. Mean and median pore sizes shift in response to the shock loading, usually to larger pore sizes. This behavior possibly results from an increased number of microcracks in the dynamically tested samples perhaps from fracture (or recrystallization) of bottle-neck pore openings whose number was found to decrease in shocked cement samples. In shock-tested samples with an uncalibrated, nonuniform (convex) loading pulse, capillary porosity was virtually eliminated from the sample, an observation confirmed qualitatively using SEM.

The above observations are consistent and are reinforced by the different types of characterization performed. Fracture and possible recrystallization of C-H seen in SEM support peak broadening observed by XRD. Similarly, granulation of C-S-H accounts for reduction of peak intensities of semicrystalline peaks also noted in XRD patterns. Porosimetry showed that shock loading reduced the amount of capillary porosity in samples recovered from C5 and mortar tests M5 and M6, but increased the amount in tests C11 and C12. High-magnification scanning electron micrographs show identical trends when compared with reference microstructures. Mercury porosimetry of shock-loaded mortar showed a decrease in the amount of submicron, e.g., capillary porosity, but also an increase in the pore sizes above 1-10 μm . Scanning electron microscopy showed significant reduction in the amount of capillary porosity and an increase in microcracking (seen typically near cement aggregate interfaces).

Although careful analysis of the microstructural data allows differences to be isolated, it does not allow identification of the specific causes of the observed behavior. None of the studies conducted in this program were designed to provide data on how the microstructural changes occur, and therefore our hypotheses do not address issues of "how" and "why," but only "what and when."

Correlation of the observed microstructural changes with the shock-loading conditions is difficult for several reasons: a) recovery tests were not instrumented with pressure gages, b) results from instrumented tests, used to calibrate the recovery ones, were affected by experimental problems, and c) variables other than shock conditions, e.g., differences in the initial, unshocked microstructure, were also likely to affect shock response.

Gas-gun impact tests and several gage-instrumented explosive loading tests gave pressure data that could be grouped into two general sets of two types: a) those conducted in either cement paste or mortar, and b) those with either a nominally planar shock pulse (from gas-guns and explosive lenses) or a slightly convex "planar" pulse resulting from point-initiated explosive charges. Pressure data showed that under duplicate loading conditions, i.e., similar gas-gun impacts or explosive drivers, shock pressures were typically 20-30 kbar lower in mortar than in cement paste, regardless of the depth within the sample. Also, the attenuation rate of the shock pulse in both cement and mortar was about 1.5 kbar/mm, over a pressure range of 30-70 kbar. Finally, peak pressures measured in instrumented point-initiated explosive tests showed that expected pressures in the uninstrumented recovery test samples would be approximately 60-40 kbar (top to bottom) for tests C4 - C7. Estimated pressures for the samples recovered from the more energetic plane-wave explosive tests in cement (C11 and C12) were between 100-75 kbar. Pressures were also estimated for the plane-wave-initiated mortar test sample (which was destroyed) to be about 75-50 kbar, and those for the mortar anvil (which was recovered) to be about 45-25 kbar, given the expected attenuation through the destroyed sample. Despite the uncertainties in test conditions, the microstructural changes that were observed were a) significantly and reproducibly different from the reference cement materials, and b) can be said to be typical of cements shocked-loaded well above the HEL (around 5 kbar) within the elastic-plastic material response regime -- generally to pressures in the range of 40-70 kbar. More detailed correlations cannot be made because of uncertainties in loading histories and differences in both material type (cement and mortar) and characteristics (porosity and maturity).

V. CONCLUSIONS

In this three-year program we sought to investigate the HSR behavior of hydrated cement paste and mortar by determining the ways in which the microstructure responded to dynamic loads. Types III and IV cement pastes were used for testing because they represent the extremes in mineralogy of common cement types. In order to study effects of porosity in cement material response, pastes were prepared with varying w/c to produce a suite of samples with differences in the amount of fine (capillary) porosity. In an effort to minimize effects from the differences in maturity of fresh cement pastes, samples were cured for at least 28 days prior to testing; some samples, particularly those used for shock loading experiments in later program stages, were typically 60-90 days old when tested.

Initial studies were conducted at low strain rates (up to 10^0 s^{-1}), using a hydraulic mechanical testing machine, and at intermediate strain rates (up to 10^3 s^{-1}), using a SHPB, to load samples in plane-stress. Tests measuring the dynamic yield strength confirmed that the material response remained in the brittle, elastic regime. The yield stress of all cement types was found to be directly dependent on strain rate (as expected). However, the Type III specimens with low w/c ratios, i.e., 0.25 and 0.33, showed an unexpected strain-rate sensitivity at loading rates around 10^2 , marked by a discontinuity in the yield strength/strain rate relationship, the cause of which was not isolated. Such behavior may correlate with SEM observations where fracture surfaces in SHPB test specimens showed little preference for fracture path, whereas those seen in low strain-rate test specimens showed more preferential fracture through C-S-H, the weakest phase. Dynamic yield strength was shown to be dependent on the amount of capillary porosity (w/c ratio) and the maturity of the cement paste. High porosity samples had lower strengths, as did those with a lower degree of hydration.

Tests at very high strain rates ($10^4 - 10^5 \text{ s}^{-1}$) required development of impedance-matched momentum traps that allowed samples to undergo uniaxial

strain impulses without experiencing damaging reflections of the initial loading pulse. These would complicate the loading history or, at worst, destroy the sample and prevent its recovery for microstructural characterization. After a series of development experiments, 0.25 w/c Type III cement pastes and mortar samples were shock loaded with explosive charges (at an indoor facility at NSWC). Peak pressures were estimated to be in the range of 25-100 kbar (typically around 40-75 kbar), which is above the ~ 5-kbar HEL that we determined from gas-gun testing of pastes and mortar. The highest pressure tests were conducted using a plane-wave explosive lens to initiate an explosive charge in contact with the specimen, thus providing what we believed was the most uniform, planar impulse. Other recovery tests with somewhat lower peak pressures were conducted using explosive charges initiated with a single blasting cap. These resulted in a shock wave with a convex shape, whose radius of curvature, while likely approximating a plane wave, could still have had a significant shear component. Loading other than in uniaxial compression complicates both the initial and subsequent reflected, loading histories.

Comparative analyses of the microstructures of unshocked and shocked cement paste and mortar samples, using principally XRD, SEM, and mercury porosimetry, showed significant shock-induced changes, including:

- Particle-size reduction and/or residual lattice strain in hydrated minerals which were not observed in unhydrated alite
- Lattice distortion in both C-H and alite in higher pressure tests
- Disordering of semicrystalline C-S-H
- Alteration of pore-size distribution by modification/elimination of capillary porosity and introduction of microcracks
- Granulation of C-S-H

- Disappearance of angular (crystalline) particles from fracture surfaces.

It is important to point out that microstructural response was affected not only by the initial shock pulse, but also by later-stage complex reflections within the sample that undoubtedly occurred despite the extensive momentum-trap fixture. Such reflections account for the destruction of either parts of or of the entire test specimen, and their effects cannot be separated from that of the primary pulse. Additionally, correlations between the degree of microstructural response and the magnitude of the shock impulse could not be made for reasons that in part reflect uncertainties of the sample loading histories and influences from other variables such as sample porosity and other heterogeneities. Significantly more testing, designed to isolate suspected variables, is needed to fully understand the microstructural responses.

VI. SUGGESTIONS FOR FUTURE RESEARCH

During the course of this study, we have documented microstructural changes associated with high strain-rate loading of cement paste, and provide some additional preliminary mortar data. It is clear from these efforts that microstructural changes take place with increasing severity of loading conditions. The change from plane stress tests, e.g., the SHPB, to plane strain tests using explosives, flyer plates, or gas guns, has been shown to produce significant changes in the microstructure of cement paste. These changes are documentable and repeatable, but the details are difficult to describe accurately. This largely results from the complexity of the microstructure of cement and the fact that it is made up largely of amorphous phases which do not show up on X-ray diffractograms. Hence, while these phases might change significantly as a result of the loading event, the changes are difficult to document quantitatively.

The principal problems encountered in this research were with the loading experiments. It was desired that a range of loading rates, and, in the case of loading above the HEL, a range of shock pressures, would be available for study. Changes could then be documented over that range and the direction of change discerned. What was actually achieved was a series of tests that in the final analysis were essentially undocumentable as to pressure range, and were therefore essentially, within error, conducted at the same peak pressure. The principal difference between the tests was that, in two cases where recovery was possible, the loading state achieved was not plane strain, whereas in the remainder, we have some confidence that plane strain was achieved. As stated in the conclusions, the major microstructural differences encountered are found between these two groups of samples. Where plane strain was not achieved, we believe the principal cause to be the introduction of a shearing component. There are also major microstructural differences between the plane-stress- and plane-strain-loaded samples, which likely result from the degree of plastic deformation encountered in those samples loaded above the HEL.

In order to build on the progress we have made, the key issue is achieving documentable, repeatable shock loading tests, from which samples are recovered, which is a most difficult task. In many of the tests done, where reasonably good test data were obtained, specimen recovery was absent. Likewise, where specimens were recovered, documentation of the loading conditions was not always good. This shrank the amount of tests where both good loading data and recovery were achieved to a number too small for statistical analysis. The work done to date indicates the potential for additional understanding of the microstructural basis for the dynamic behavior of cement and cement-based materials that can be gained from this type of research, but considerably more work must be done to put the results on a firm, quantitative footing.

The other important factor in understanding the dynamic behavior of cement, which was not addressed at all in this effort, is the need to model computationally the processes going on during the dynamic event as well as the conditions leading to the strain history of the loaded specimen. Although measurements can give insight into the stress or strain history experienced by the sample, only by computationally modeling the event, using a realistic first principles modeling, can that history be quantitatively constructed. Modeling was not a part of this effort and reasonably so, given the time and cost constraints along with the paucity of information on what was actually happening to the microstructure. It should be a part of the next effort. We have documented some of the changes occurring, especially pore collapse, the modification of porosity (change in size, introduction of different types of porosity), and the reconstruction of the microstructure. These changes can be implemented in a first principles model and coupled with larger hydrodynamic codes like EPIC to enable calculations of the stress history of the sample.

Modeling must not, in our opinion, be done in the absence of the experimental work, which we believe should be the focus for any continued effort in this area. The next effort should focus on improving the shock recovery tests and the documentation of the shock history seen by the sample. The second requires coupling in the modeling function, as no

instrumentation can be expected to survive more than the first pass of the initial shock wave in the sample. By further improving the loading fixtures and the positioning of strain gages, more of the reflected energy can be scavanged before it is propagated back into the sample, and a better picture of the attenuation and modification of the strain wave can be obtained. These improvements, coupled with modeling and close examination of the microstructural changes occurring in the material, should lead to a better understanding of the manner in which cementitious materials fail at high strain rates.

REFERENCES

1. Mindess, S., in Structure and Performance of Cements, Ch. 7, P. Barnes (ed.), Applied Sci. Publ., London, p. 319 (1983).
2. Jawed, I., "Hydration of portland cement," in Cements Research Progress - 1984, J.F. Young, ed., pp. 77-105, American Ceramic Society, Columbus, OH (1985) (in press).
3. ASTM, 1978 Annual Book of Standards, Part 13, Philadelphia, PA (1978).
4. Cem. and Concr. Res.. 15, pp. 320-330 (1985).
5. R.L. Berger, Science, 175, 626 (1972).
6. R.L. Berger, F.V. Lawrence, Jr. and J.F. Young, Cem. Concr. Res., 3, 497 (1973).
7. B. Marchese, Cem. Concr. Res., 7, 9 (1977).
8. DeCarli, P.S., and M.A. Meyers, "Design of uniaxial strain shock recovery experiments," in: Shock Waves and High Strain-Rate Phenomena in Metals, M.A. Meyers and L.E. Muir, eds., Plenum Press, pp. 341-373 (1981).
9. Rootare, H., "A review of mercury porosimetry," in Advanced Experimental Techniques in Powder Metallurgy, pp. 225-252, Plenum Press, New York (1970).
10. Winslow, D.N., and Diamond, S., "A mercury porosimetry study of the evolution of porosity in portland cement," J. Mater. 5 (3), pp. 564-585 (1970).
11. Jawed, I., G. Childs, S. Winzer, S. Johnson, R.T. Dick, and D. Barker, "High Strain-Rate Behavior of Hydrated Cement Paste," 1987 Annual Report For AFOSR Contract F49620-86-C-0021, MML TR 88-1c, January 1988.
12. Johnson, R.E., Jr., and R.H. Dettree, in Surface and Colloid Science, Vol. 2, E. Matijevic, ed., Wiley-Interscience, New York, (1969).